

POLITECNICO DI TORINO

Master's Degree

in

Biomedical Engineering



Process optimization and experimental measurements of organic electrochemical transistors for in liquid biosensing

Supervisor:

Dr. Cocuzza Matteo

Co-supervisors:

Dr. Marasso Simone

Dr. Frascella Francesca

Candidate:

Salucci Leila

Academic year 2018/2019

Abstract

This thesis is focused on the fabrication of organic electrochemical transistors (OECTs) constituted by a silicon oxide substrate, gold source and drain electrodes and a poly-(3,4-ethylene-dioxythiophene):poly-(styrenesulfonate) (PEDOT:PSS) channel. Within the production process two improvements of the device properties were investigated: the addition of (3-glycidyloxypropyl)trimethoxysilane (GOPS) in the polymeric solution to enhance the adhesion on the substrate, and a post-deposition treatment of the original solution with sulfuric acid in order to improve the conductivity. These enhancements were combined with two different techniques for the PEDOT:PSS deposition: the spin coating and the ink-jet printing methods. After the fabrication, OECTs have been characterised in order to check if they worked properly, to evaluate their performances and finally to compare the devices, developed following the different fabrication approaches. The experimental measurements involved different electrolytic solutions and simple molecules, like streptavidin-HRP and VEGF, after the gate functionalization. Further smaller OECT platforms were fabricated, in order to equip this technology with a pre-fabricated microfluidic set-up and to perform real-time measurements.

Acknowledgements

I would like to thank my supervisors Dr. Matteo Cocuzza, Dr Simone Marasso and Dr. Francesca Frascella for the opportunity to work at this thesis project, for their constant and great help and expertise.

Special thanks to the entire Chilab staff, from the people who helped me since the beginning to the ones who made the laboratory a positive and challenging working environment, always willing to help me with patience and constantly showing their passion for the research: Alessio V., Matteo P., Valentina B., Federica B., Alberto B., Eve V., Giorgio S., Matteo S. .

A last thank also to the Nanosciences Laboratory, in particular to Gianluca P. and Alessandro C..

Contents

Abstract	iii
Acknowledgements	iv
Contents	v
Introduction	viii
i. Liquid sensing with organic transistors	ix
ii. Description of this work	xi
1. OECTs for biosensing applications	12
1.1. The organic conductive polymer	14
1.2. The working principle	17
1.3. The device physics	19
1.4. Transduction principles	23
1.4.1. Polarization of the interfaces	23
1.4.2. Increased ion flow at polymer-electrolyte interface	27
1.4.3. Electron transfer	27
1.5. State-of-the-art in biosensing	30
1.5.1. Fabrication techniques	30
1.5.2. Sensing interfaces	33

1.5.2.1. Functionalization of channel surface	34
1.5.2.2. Functionalization of gate surface	35
1.5.3. Biological classification	37
2. Materials and methods	39
2.1. Device overview	39
2.2. Device fabrication	41
2.2.1. Metal electrodes	41
2.2.2. PEDOT:PSS deposition	44
2.2.2.1. Solutions preparation	46
2.2.2.2. Spin coating	48
2.2.2.3. Ink-jet printing	52
2.2.3. PDMS chamber	55
2.2.4. Gate electrode	56
2.2.5. The real-time platform	57
2.3. Device functionalization	57
2.3.1. Streptavidin-peroxidase (Stp-HRP)	58
2.3.2. Vascular endothelial growth factor (VEGF)	60
2.4. Device measurement set-up	61
2.4.1. Set-up for characterization	62
2.4.2. Set-up for the detection	64
3. Ink-jet printing optimization	67
3.1. Jetlab 4 ink-jet system	68
3.2. The problem of clogging	69
3.3. The main settings	71
3.3.1. The back-pressure	71
3.3.2. The driving waveforms	73
3.4. The additional settings	83
3.5. Surface preparation	85
4. Results and discussion	90
4.1. Fabrication process	90
4.2. Electrical conductivity enhancement	94

4.3. Adhesion enhancement	99
4.4. Stability after 15 days	103
4.5. First detection measurements	106
4.6. Real-time measurements	110
5. Conclusions and future works	113
Appendix - Easy guide to Jetlab 4 ink-jet printer	115
General description	115
Reference system	118
Initialization and simple printing	119
Printing from digital models	121
Alignment process	125
References	130

Introduction

This thesis work is inserted within two projects, concerning different applications of biosensors and both co-founded by Regione Piemonte inside of the European Funds for Regional Development (POR FESR 2014-2020): *DEFLeCT* and *Food Drug Free*.

DEFLeCT (Digital tEchnology For Lung Cancer Treatment) is part of the “Health and Wellness Technological Platform” and is intended to produce an advanced platform for the early detection of non-small cells lung cancer (NSCLC). It involves a project team, constituted by both academic and corporate partners, like Aizoon Consulting s.r.l., Politecnico di Torino, Università di Torino, Azienda Ospedaliera S. Luigi, Abich s.r.l., Chimete s.r.l., Essebi s.r.l., Fluody s.r.l., Gem Chimica s.r.l., Human Brain Wave s.r.l., Honestamp s.r.l., Lamp s.r.l., Osai S.p.A., Consorzio Proplast, Renishaw S.p.A., S.In.Co.S. Applications s.r.l., STV Italia s.r.l., Trustech s.r.l..

In the framework of “Bioeconomy Technological Platform”, the project *Food Drug Free* has the goal of developing a miniaturized and portable platform for the detection of drugs in food products. It gathers the work and the experience of both technological partners and manufacturing companies: Informatica System

S.r.l., Politecnico di Torino, Bruno Kessler Foundation, Università degli Studi di Scienze Gastronomiche, DGS S.p.a., Cemas Elettra S.r.l., Sky Technology S.r.l., Chemsafe S.r.l., Eltek S.p.a., Istituto Zooprofilattico Sperimentale del Piemonte, Liguria e Valle d'Aosta, Beppino Occelli I Formaggi S.r.l., Golosità Dal 1885 S.r.l., La Monfortina S.r.l..

The Department of Applied Science and Technology (DISAT) of Politecnico di Torino actively collaborates in both projects and deals with the design, the development and the testing of microelectronic devices, specially selected for the detection of biological molecules, like tumour markers (*DEFLeCT*) and antibiotics (*Food Drug Free*). These innovative systems may significantly reduce the response times for this kind of analysis and aim to pave the way towards point-of-care testing and in-situ detection.

i. Liquid sensing with organic transistors

The selected devices for the detection of biological analytes are microelectronic sensors, based on transistors. The latter present two metal contacts, called source and drain electrodes, linked by a doped semiconductor material, which constitutes the channel, and where a current flows under the application of a drain-source voltage (V_{ds}). An insulator, typically silicon oxide, is placed between the semiconductor and the third electrode, the gate. On the latter, the gate-source voltage (V_{gs}) is imposed, which generates an electric field in the oxide and controls the current in the channel, the drain-source current (I_{ds}). From this specific working principle, the devices have been named field effect transistors (FETs).

In several applications requiring the analysis of solutions or the detection of ions, molecules or other analytes, an electrolytic solution constitutes the insulating element between the gate and the channel, allowing the in-liquid sensing. The gate electrode is immersed in the electrolyte, which is contained in a chamber. A very promising perspective have been observed in devices, which involve a doped semiconductor of organic nature, constituting the channel. The

development of these remarkable sensors, called organic field effect transistors (OFETs) was allowed by decades of research in new materials and fabrication processes.

Within the two projects, two different materials, constituting the channel of FETs, were patterned between gold electrodes: the graphene and the polymer poly(3-hexylthiophene-2,5-diyl) (P3HT), which constitute graphene field effect transistors (GFETs) and electrolyte gated field effect transistors (EGOFETs), respectively.

The third biosensor involved in these works is the organic electrochemical transistor (OECT), another three terminal device in which instead of the electric field effect, ions from the electrolyte can penetrate the organic polymeric channel of poly-(3,4-ethylene-dioxythiophene):poly(styrenesulfonate) (PEDOT:PSS), due to the application of a gate-source voltage. OECTs have been recently used as detection platforms for multiple analytes, as ion or enzymatic sensors and in the field of electrophysiology. The possibility to fabricate such biosensors on flexible substrates and the compatibility with the human skin make OECTs also

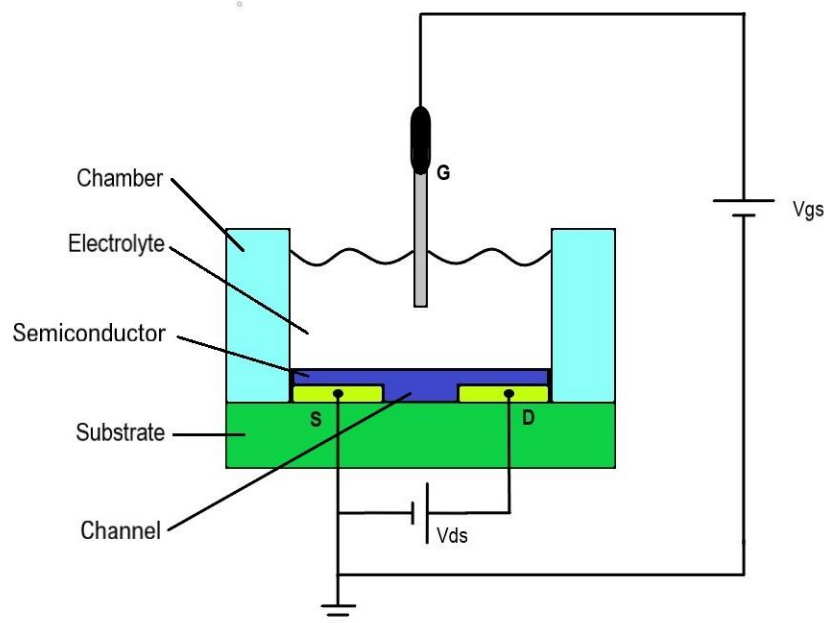


Fig. 1 – Scheme of a transistor biosensor for the analysis of solutions and/or analytes. The semiconductor may be realized, for example, by graphene, P3HT or PEDOT:PSS in order to fabricate GFETs, EGOFETs or OECTs, respectively. The picture shows a typical configuration for the measurements, where the source terminal is grounded and the voltages V_{ds} and V_{gs} are referred to the source.

promising wearable devices. At the same time, thanks to the biocompatibility of the polymeric material involved in its fabrication, these sensing platforms can host a wide variety of cell types, facilitating adhesion and promoting ionic interactions with the polymeric surface.

ii. Description of this work

This thesis is focused on the fabrication of OECT devices constituted by a silicon oxide substrate, gold source and drain electrodes and a PEDOT:PSS channel. Within the production process two improvements of the device properties and two techniques for the deposition of the polymeric channel were investigated: the employment of an additive inside the polymeric solution, a post-deposition treatment of the original solution and, concerning the deposition techniques, a photolithographic and a printing process. After the fabrication, OECTs were characterised in order to check if they worked properly, to evaluate their performances and finally to compare the devices, developed following the different fabrication approaches.

The work continued with the first measurements of different electrolytes up to the detection of simple molecules, after the OECT functionalization. The final real-time measurements have been performed by using a dedicated microfluidic set-up, which allows the exploitation of the same design also for the other sensing devices (EGOFET and GFET).

1. OECTs for biosensing applications

Among transistor-based sensors, OECT is notable for its peculiar and attractive properties that make it adaptable in many research fields and for several applications.

The very low working voltages (<1 V) of these devices allow a low power consumption, maintaining good amplification and transconductance. The usage of organic polymers confers cytocompatibility and some device components allow different bio-functional modifications, as it will be explained afterwards.

The attractive properties of OECTs are reported here and briefly described:

- **High transconductance:** in the transistor-based devices a modulation in the gate-source voltage (ΔV_{gs}) leads to a high modulation in the drain-source current (ΔI_{ds}). The main parameter that can quantify the efficiency of this modulation is the transconductance, defined as $g_m = \partial I_{ds} / \partial V_{gs}$. This value can be computed from experimental data of the characterised device, as the derivative of the transfer curve ($g_m = \Delta I_{ds} / \Delta V_{gs}$). High transconductance means that small changes in V_{gs} lead to a higher variation in I_{ds} and thus a

better sensitivity of the biosensor [1]. In OECTs high transconductances are achieved due to the ability to absorb ions by the whole channel volume [2].

- **Low working voltages:** OECTs can be operated with low gate-source and drain-source voltages [3]. Typical values are between -1 V and 1 V for the gate voltage, and from -1 V to 0 V for the drain voltage. The corresponding currents usually do not exceed 100 mA, thus the power consumption is very low [1].
- **Cytocompatibility:** the use of biocompatible organic components, such as PEDOT (a conductive polymer described in the following paragraphs), allows the interfacing of sensors with biological compounds, like cells, tissues and other biological samples. Several studies in tissue engineering were focused on the use of PEDOT-based hydrogels [4,5] or scaffolds [6,7], confirming its excellent biocompatibility.
- **Bio-functional modification:** OECTs can be modified bonding either an antibody or an antigen on one of their sensitive surfaces. This operation allows the OECT to immobilize specific biomolecules and to detect very low concentrations (up to femtomolar for some species), due to the good amplification nature of these devices [1].
- **Suitable response time:** OECTs are considered slow electronic devices with their response times typically on the order of 1-100 ms and sometimes larger than 1 s. For electrochemical biosensing, this does not represent a limit, because very high working frequencies are usually not required. The commercial and already available tests on the market (such as ELISA kits, colorimetric-, fluorescent- or surface plasmon resonance-base biosensors), which represent the main competitors of microelectronic biosensors, show detection times from about 30 minutes up to few hours [8].
- **Ease of fabrication:** the simplest OECT device is also easy to produce, in fact it needs the fabrication of the three electrodes on a substrate (typically glass or silicon oxide) and the installation of the electrolytic chamber. All these elements are realized with easy fabrication steps, due to the easy processability of the involved materials [9].

- **Wearable biosensing:** these devices may be supported on a flexible substrate or they can be constituted by textile materials, thus paving the way for wearable OECT biosensing [10–13]. This concept of OECT still ensures ample margins for research and improvements.

The above-mentioned peculiar advantages of OECT technology enhanced the wide development of these devices in bio-sensing applications. OECTs can successfully be utilized as biosensors, for their excellent capability in electrochemical transduction. A biosensor is a detection device, designed for the recognition of entities of biological origin, using a transducing element to convert the formation of biological complex into an electronic signal. It can also be constituted by fully synthetic recognition entities, but it is aimed at the recognition of biomolecules. The two elements that compose the biosensors are the probe and the transducer. The first one represents the biochemical recognition component, while the second constitutes the transducing element of the device [9].

This chapter is focused on the description of the main material constituting the transistor channel, the OECT working principle and its basic physics, the transducing modalities by which the biological component is converted into an electrical signal, and finally some classification of OECT devices developed for biomedical applications, where they are grouped by the sensing interfaces and by the biological detection typologies.

1.1 The organic conductive polymer

In the past years various organic conducting polymers were used in the fabrication of the semiconductor channel of OECTs: polypyrrole (PPY), polyaniline (PANI), polyfluorene, polythiophene (PT), etc [9]. After the first use of a PT derivate, the poly(3-methylthiophene), in 1985 [14], the researchers continued to move towards the design of other conjugated polymers, to further improve the device characteristics. Among all of them, the most common polymer for OECT devices is a derivate of PT: poly-(3,4-ethylene-

dioxythiophene):poly(styrenesulfonate) (PEDOT:PSS) [2,15]. In fact, it shows a higher stability towards chemical and electrochemical modification and towards air oxidation [9], than the historical conducting polymers, PPY and PANI.

PEDOT:PSS is composed by:

- **PEDOT**: an intrinsically conducting polymer (ICP) obtained from the oxidative polymerization of 3,4-ethylene-dioxythiophene (EDOT) [9] (Fig. 1.1). After this process, PEDOT is already a conducting polymer, thanks to its conjugated structure composed by alternating single and double bonds. In fact, the π -type bonds between adjacent carbon atoms are weak bonds, and thus the corresponding charge is easily delocalized across the polymeric chain.

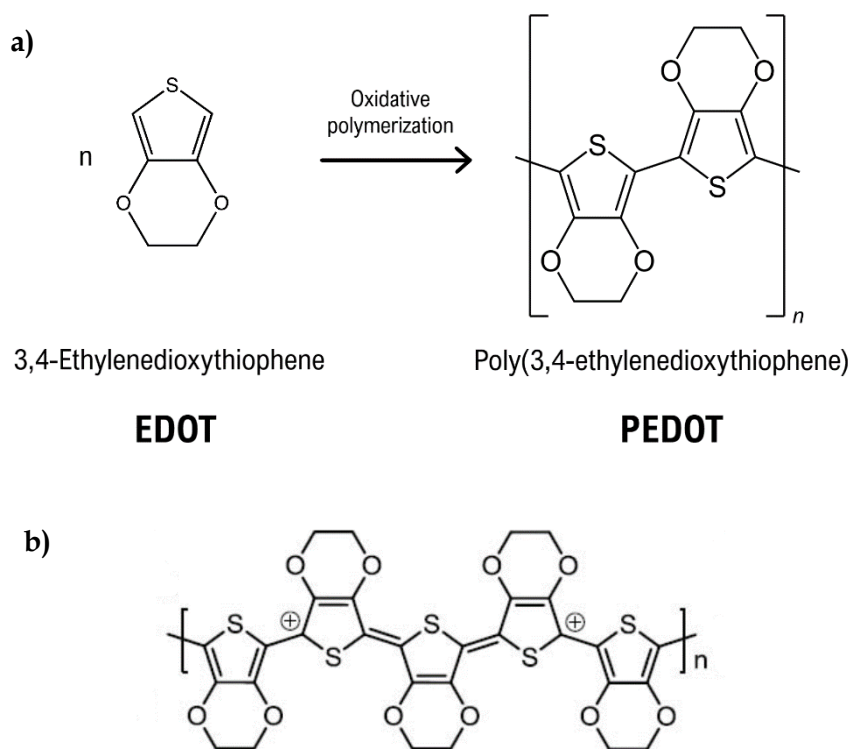


Fig. 1.1 – The polymerization of EDOT (a) and the oxidized state of PEDOT (b).

The conductive property of PEDOT is enhanced by oxidation: the polymer cedes electrons and the holes can be found on the main chain. Thus, through oxidation PEDOT is p-doped and its positive charges can be transported if a voltage is applied. During oxidation, the chains arrange themselves enclosing the charges, generating particular structures, called polarons,

which facilitate the hole transport. The more the polymer is oxidized, the more polarons are created and thus the higher is the conductivity. For this reason, PEDOT presents a higher conductivity (in the range of 1-100 S/cm, depending upon the film morphology and the choice of counter ion [15]) with respect to the undoped material. Furthermore it is very stable in its oxidized state [9], but it's insoluble in water, thus its deposition proves difficult to apply.

- **PSS:** a polyanion obtained by the sulfonation of polystyrene. It shows negative charges, on the sulfonate groups (SO_3^-). The PSS anions compensate for the shortage of negative charges in PEDOT, stabilizing its oxidation state [2]. The addition of PSS ensures the solubility of PEDOT:PSS and improves its conductivity [9,15]. In fact, the PEDOT chains can align with the PSS ones, assuming a spatial arrangement that allows a better flow of positive charges current. PEDOT:PSS maintains a good stability, gaining transparency and good film forming.

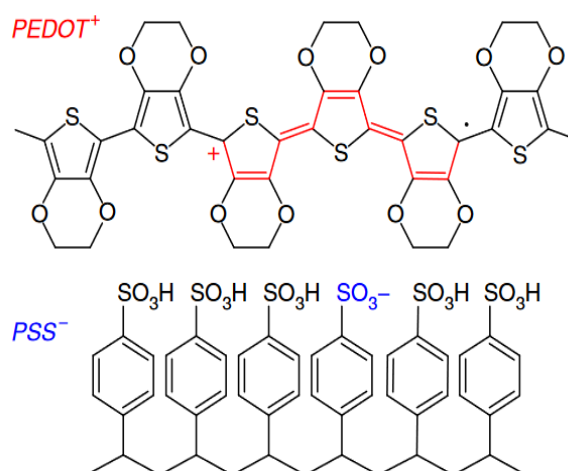


Fig. 1.2 - The chemical structure of PEDOT⁺ and PSS⁻. A positive polaron (+) on the PEDOT chain is compensated by a negative charge (-) on the sulphonate ion on the PSS chain [16].

The main properties of PEDOT:PSS, as high conductivity, electrochemical stability, reversible ion penetration, bio-compatibility, easy commercial availability and applicability for flexible substrates [17], make it thus the most used ICP for OEETs.

The different film-deposition techniques for PEDOT:PSS in the OECT fabrication will be described later.

1.2 The working principle

As seen above, PEDOT in its oxidation state, due to its polymerization process and its great oxidation stability, obtained with the conjugation of PSS, allows the flow of positive charge carriers between drain and source electrodes. In this state, PEDOT:PSS becomes a positively-doped (p-doped) semiconductor polymer.

Under an application of a drain-source voltage, at zero gate voltage (Fig. 1.3), the PEDOT:PSS is in its *on* state: the ICP is conducting. The current of positive charges flows through the channel, due to the external potential between drain and source.

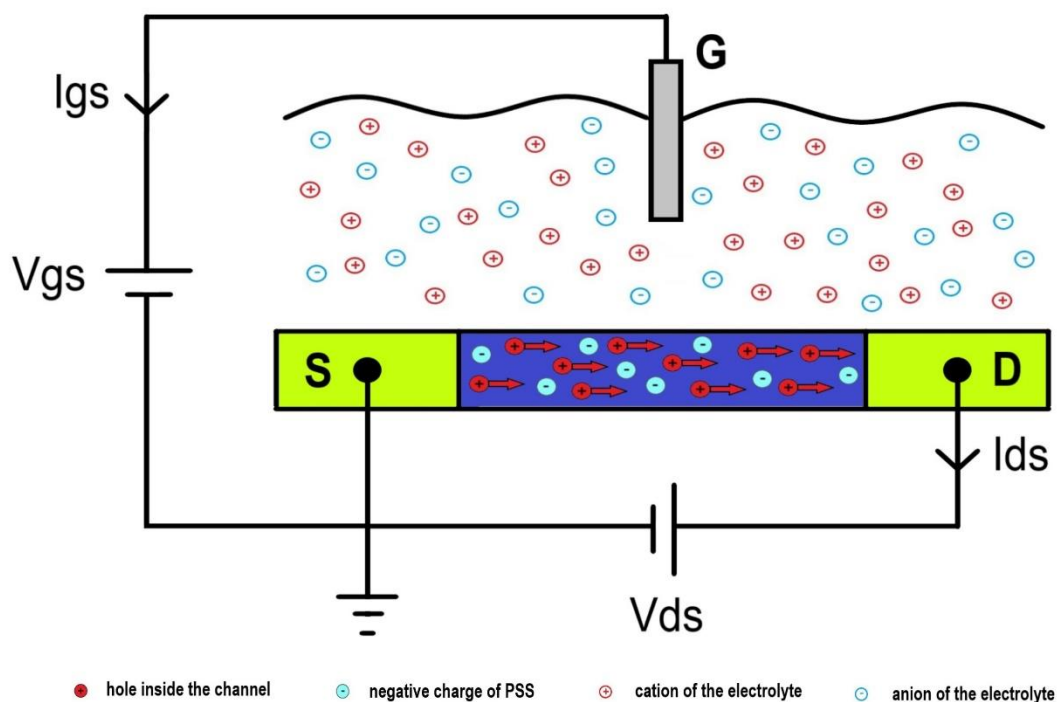


Fig. 1.3 – The working principle of OECT at $V_g = 0V$: the positive charge carriers inside the PEDOT:PSS channel are responsible of the source-drain current flow, so the device is in the *on* state.

In response to an application of a positive gate bias (Fig. 1.2), the cations present in the electrolyte move towards the channel, rejected by the positive polarization of the gate electrode. These positive ions inject into the channel, compensating

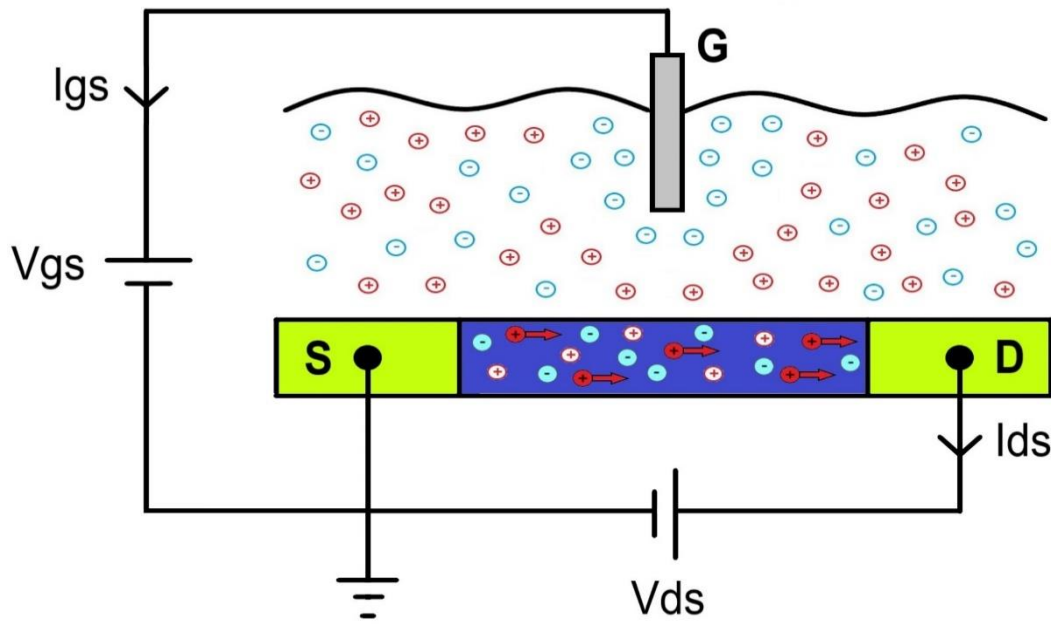


Fig. 1.4 – The working principle of OEET at increasing positive gate voltages: positive ions in the electrolyte repulsed by the positive V_g penetrate the channel, reducing the doping state of the polymer and the carrier mobility, thus I_{ds} decreases.

the negative charges of PSS. Thus, the density of positive charge carriers inside the PEDOT:PSS film is reduced by the ionic interactions. The conductivity of the polymer decreases. Since the cations are responsible of the de-doping of PEDOT:PSS, this working principle is called depletion mode. Increasing the gate potential, the channel decreases even more, leading the device to the *off* state. Therefore, the current I_{ds} is proportional to the quantity of mobile carriers in the channel and is related to the channel doping state, in the case that the gate potential is switched off. In fact, the cations return to the electrolyte and the oxidation of the PEDOT is restored.

This phenomenon is described by the following electrochemical reaction:



where M^+ is the cation from the electrolyte and e^- is the electron from the source electrode[18]. The cation, entering into the channel, causes the decoupling of the two constituent polymers. From its oxidation and high conducting form, PEDOT⁺ mutates in its neutral and less conducting state of PEDOT⁰, absorbing

an electron from the source. Since the very long PSS chains cannot leave the film, the SO_3^- of PSS binds the cation M^+ inside the channel, generating $\text{M}^+:\text{PSS}^-$. The reversibility of this reaction allows the recovery of the initial state of the polymer.

The PEDOT oxidation level can modulate the conductivity of the channel, demonstrating a high sensibility in controlling the channel current through the gate voltage application. This important quality allows the OECT to be considered as high-performance transducer, especially in biosensing applications [3].

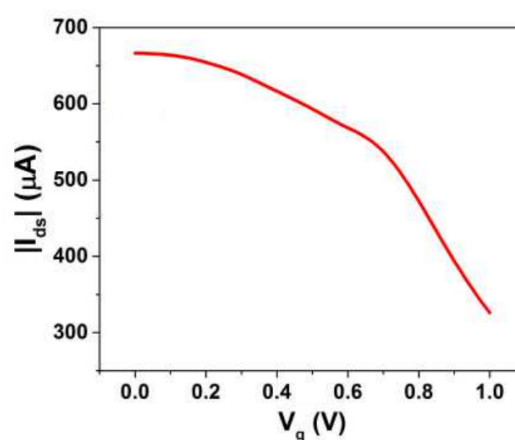


Fig. 1.5 – A typical transfer characteristic curve of an OECT, in which $|I_{ds}|$ decreases upon the application of increasing values of V_g [3].

1.3 The device physics

Bernards and Malliaras [19] developed the device model for the behaviour of the OECT. The device can be considered as a combination of two circuits: the electronic and the ionic circuit.

The first one represents the charges flow in the source-channel-drain system. According to the Ohm's law, the current flux is:

$$J = \sigma E \quad (1.2)$$

and

$$\sigma = q\mu p(x) \quad (1.3)$$

where q is elementary charge, μ is the hole mobility, $p(x)$ is the hole density. The current flux $J(x)$ across an infinitesimal portion of the semiconductor channel upon an applied electric field dV/dx is:

$$J(x) = q\mu p(x) \frac{dV(x)}{dx} \quad (1.4)$$

The effective dopant density $p(x)$ in a volume v of the semiconductor can be written as:

$$p = p_0 \left(1 - \frac{Q}{qp_0v} \right) \quad (1.5)$$

where p_0 is the initial hole density in the organic channel before the application of a gate voltage and Q is the total charge of the cations injected in the organic film from the electrolyte.

The other circuit, the ionic one, describes the ions flowing in the gate-electrolyte-channel system. Like ideal polarizable electrodes in electrochemistry, the ionic circuit is described by a resistor (R_s) and a capacitor (C_d) in series [20].

The resistor represents the ions that flow in the electrolyte, as the ionic strength of the electrolyte, while the capacitor considers the ions volume in the channel, as the quantity of ions that can be stored. The transient behaviour of this circuit is akin to a charging capacitor:

$$Q(t) = Q_{SS} \left(1 - e^{-\frac{t}{\tau_i}} \right) \quad (1.6)$$

where Q_{SS} is the total charge that passes through the circuit (the charge at steady state), expressed by the following formula, as a function of C_d and of the voltage applied across the electrolyte ΔV :

$$Q_{SS} = C_d \Delta V \quad (1.7)$$

And where τ_i is the ionic transit time, expressed as:

$$\tau_i = C_d R_s \quad (1.8)$$

C_d can be expressed also considering the capacitance per unit area (c_d), as:

$$C_d = c_d A \quad (1.9)$$

The following pictures show the geometric structure of the model (the box represents the polymeric channel and its relative infinitesimal element, dx) and the combination of the two circuits.

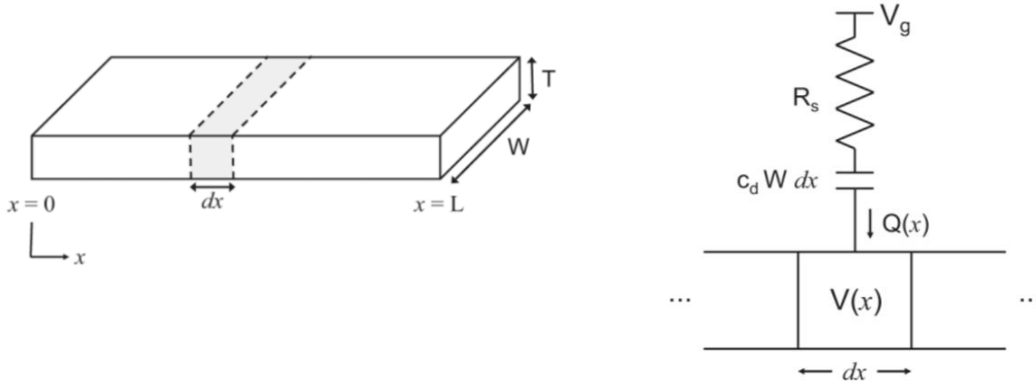


Fig. 1.6 – The representation of the channel (on the left) shows its geometric characteristics: the length L (between the source and drain electrodes), the width W and the thickness T . On the right, the electric scheme of the two circuits, that can model the device physics [19].

The model elaborated by Bernards et al. takes into account two different behaviours of the device: the steady-state and the transient. Since in this work the device have undergone measurements only after the end of transient regime, solely the steady-state equations will be considered.

The total charge passing through the circuit (Q_{ss}) is expressed by equation (1.7) and by substituting the geometrical characteristics of the device, the charge in the steady state behaviour can be rewritten as:

$$Q(x) = c_d W dx (V_g - V(x)) \quad (1.10)$$

From (1), (2), the following equation can be obtained:

$$J(x) = q\mu p_0 \left(1 - \frac{Q}{qp_0 v}\right) \frac{dV(x)}{dx} \quad (1.11)$$

where v is the volume of the channel:

$$v = WTdx \quad (1.12)$$

Replacing (1.10) and (1.12) in (1.11), it is possible to obtain the governing equation for OECT characteristics at steady state:

$$J(x) = q\mu p_0 \left(1 - \frac{V_g - V(x)}{V_p} \right) \frac{dV(x)}{dx} \quad (1.13)$$

where V_p is the pinch-off voltage defined as:

$$V_p = \frac{qp_0T}{c_d} \quad (1.14)$$

The drain-source current, obtained by integrating equation (1.13), depends on the choice of the applied drain-source voltage $V(x)$ and determines different operating behaviours of the transistor, as it can be seen in Fig. 1.7. For positive

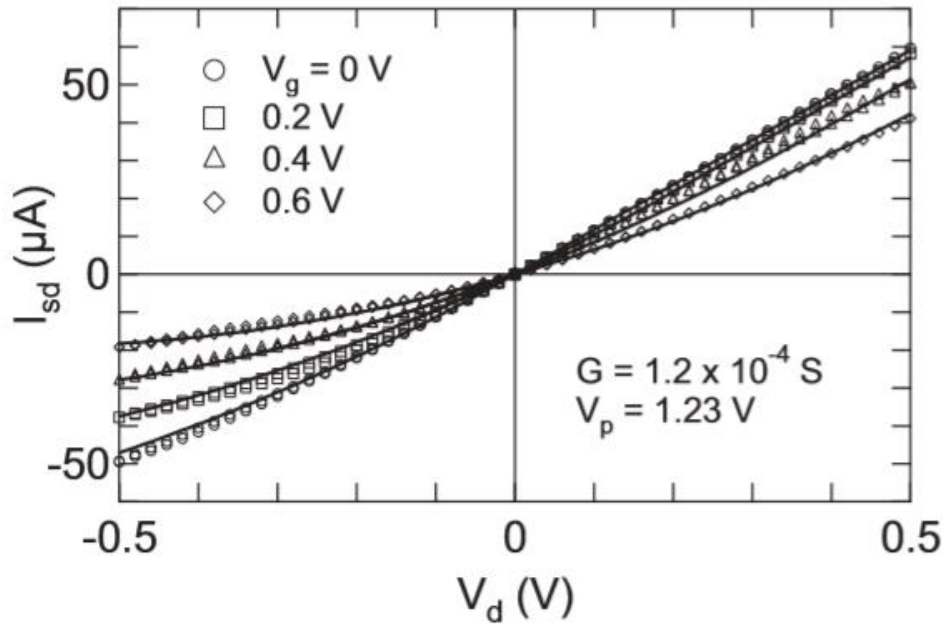


Fig. 1.7 - Typical output characteristic curves (I_{sd} - V_d), obtained imposing different values of V_g (0 V, 0.2 V, 0.4 V and 0.6 V). The solid lines show the trend of the theoretical model equations, instead the scatter lines represent the experimental measurements [19].

drain-source voltage values (as in the first quadrant), the current increases at a higher rate, until overoxidation of the PEDOT:PSS active area occurs. This phenomenon leads to an irreversible state, in which the transistor is no longer working properly. With the application of a negative V_d (third quadrant), the current gradually starts to saturate and eventually remains constant for higher

(in absolute value) source–drain voltages and this configuration allows the reversibility of the ion penetration [15]. Inside of the negative range of V_d and before the saturation ($V_d > V_g - V_p$), the equation of the current between the drain and the source terminal is:

$$I = G \left[1 - \frac{V_g - \frac{1}{2}V_d}{V_p} \right] V_d \quad (1.15)$$

where G groups all these constants:

$$G = q\mu p_0 WT/L \quad (1.16)$$

V_p indicates the onset of saturation in no-bias condition ($V_g=0$ V) and for devices with aqueous electrolytes it ranges between 0.5 V and 2 V [19].

1.4 Transduction principles

According to their specific transduction principle, OEETs can be grouped into the following categories [9]:

- polarization of the interfaces;
- increased ion flow at the polymer-electrolyte interface;
- electron transfer.

1.4.1 Polarization of the Interfaces

As seen in the previous section, the drain-source current (I_{ds}) is a function of the gate-source voltage V_{gs} upon the application of negative drain-source voltages ($V_{ds} < 0$). V_{gs} reported in equation (1.15) represents the effective voltage applied between gate and source, thus takes into account different contributions. Equation (1.15) can be re-written, considering the effective gate voltage, V_{gs}^{eff} [3,21], as:

$$I = G \left[1 - \frac{V_g^{eff} - \frac{1}{2}V_d}{V_p} \right] V_d \quad (1.18)$$

where the effective gate voltage is composed by the following two contributions:

$$V_{gs}^{eff} = V_{gs} + V_{offset} \quad (1.19)$$

V_{gs} is externally set and V_{offset} is related to the potential drop at the two interfaces: gate-electrolyte and electrolyte-channel. An alteration of the potential drop at any one interface causes a change to V_{offset} , that consequently modulates V_{gs}^{eff} . Thus, the device will show a change in the measured channel current.

Since OEETs are sensitive to the potential drop at gate-electrolyte and electrolyte-channel interfaces, different phenomena can cause a variation of V_{offset} and then a change in I_{ds} , such as any variation in concentration (ionic strength) or in the nature of the ions inside the electrolyte, that leads to a changing of V_{gs}^{eff} due to a modification in the gate-electrolyte interfacial capacitance.

The relation between the ion concentration in the electrolyte and the consequent change of V_{gs}^{eff} can be explained also with the following equation [22]:

$$V_{offset} = -E_{Nernst} = E^0 + \frac{kT}{ne} \ln Q \quad (1.20)$$

where E^0 is a constant, k is the Boltzmann's constant, T the temperature, n the number of transferred electrons, e the electron charge and Q is the reaction quotient, which depends on the concentration of each species:

$$Q = \frac{[PEDOT^0]^n [M^{n+} : nPSS^-]}{[PEDOT^+ : PSS^-]^n [M^{n+}]} \quad (1.21)$$

The above-mentioned working principle regards ion-sensors (an example in Fig. 1.8), such as for K^+ , Ca^{2+} , Al^{3+} concentration.

Another configuration that can modulate V_{gs}^{eff} , changing the interfacial capacitance, is the case of bio-recognition methods. The immobilization of bio-recognition molecules, such as antibodies, aptamers, antigens allows the capture of the target substances, like antigens, nucleic acids, cells, small proteins etc.

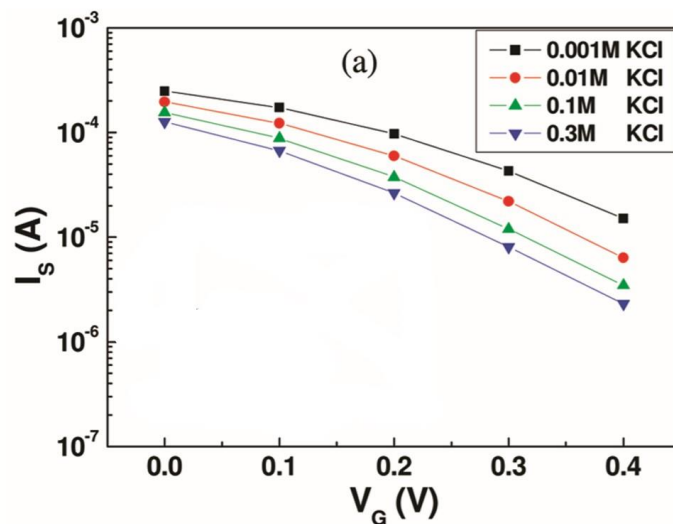


Fig. 1.8 – OEET transfer characteristics at $V_{DS} = -0.1$ V for different KCl concentrations [22].

This immobilization may occur on a functionalized channel, thus allowing a modification of the capacitance between channel and electrolyte (see Fig. 1.9) and, in consequence, a change in V_{offset} [23].

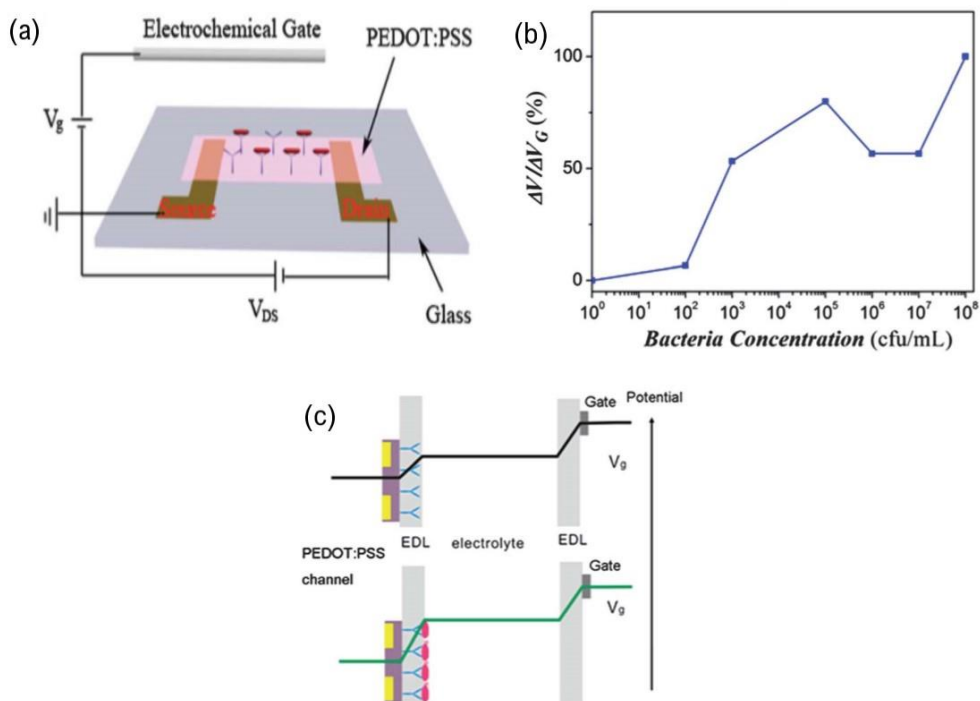


Fig. 1.9 – The immobilization of *E.coli* on the specific antibodies on the channel surface (a) causes a wide change in V_g s at increasing bacteria concentrations (b,c) [23].

Another phenomenon that may contribute to the variation of V_{offset} is the binding of the target with the functionalized gate electrode (Fig. 1.10), which causes a modification in the gate-electrolyte capacitance, since it increases the so-called double layer thickness. This latter exists at the interface between an electrode and its surrounding electrolyte, where ions from the solution move closer to the surface of the electrode. Charges in the electrode are separated from the charges of these ions, by a distance on the order of tens of nanometers, composed of polarized solvent molecules. Charges separated by an insulator form a capacitor, whose capacitance is inversely proportional to the distance between the charges. Increasing the thickness of the double layer, due to the immobilization of target molecules, causes the variation in this capacitance, and consequently in the V_{offset} [24].

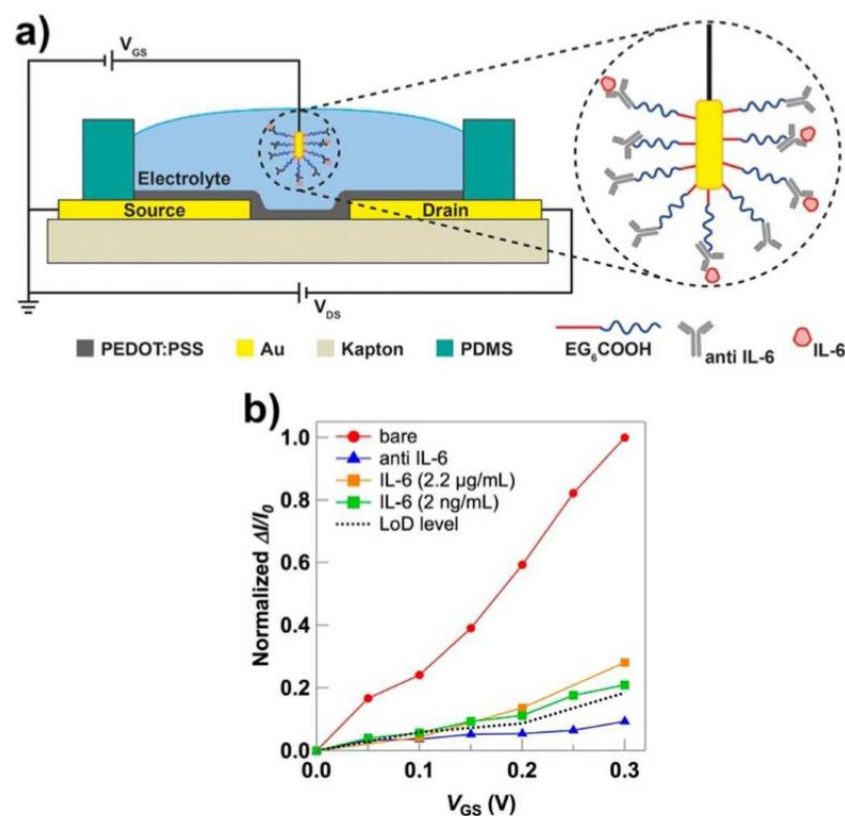


Fig. 1.10– The bonding between the anti-IL-6 and its antigen on the gate surface modifies the V_{gs}^{eff} , whose variation is detectable measuring the corresponding $I_{ds}-V_{gs}$ curves [24].

1.4.2 Increased Ion Flow at Polymer-Electrolyte Interface

A selective membrane, placed on the polymer film, allows the injection of specific cations into the channel [15]. Therefore, it results in an increasing concentration of those ions permeating through the membrane and penetrating the polymer. This latter is de-doped and then it can be measured a decreasing drain-source current. Two interesting works have led to the implication of K^+ selective membrane [25] and to the detection of Na^+ and K^+ ions through a membrane containing gramicidine [26].

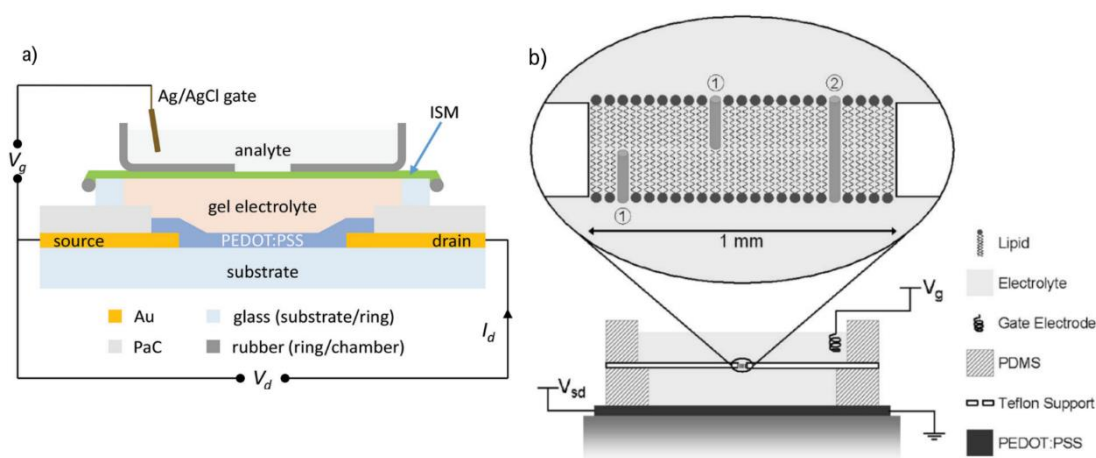


Fig. 1.11 – Examples of devices with selective membranes: (a) an K^+ ion selective membrane (ISM) [25] and (b) a Na^+ and K^+ ISM [26].

1.4.3 Electron Transfer

In this case devices in which electroactive molecules or enzymes generate a redox reaction on the gate electrode surface are considered.

The electroactive chemicals, such as norepinephrine, dopamine, serotonin, can be directly oxidized or reduced on the electrode. This kind of biosensors are called enzyme-free OEETs and represent low-cost and easy-fabricating OEETs, but show a weak selectivity compared to the extreme selectivity of most enzymes. Gallic acid is a typical example of electroactive molecule, that can directly react with a modified gate surface, causing a variation of the gate/electrolyte capacitance [27].

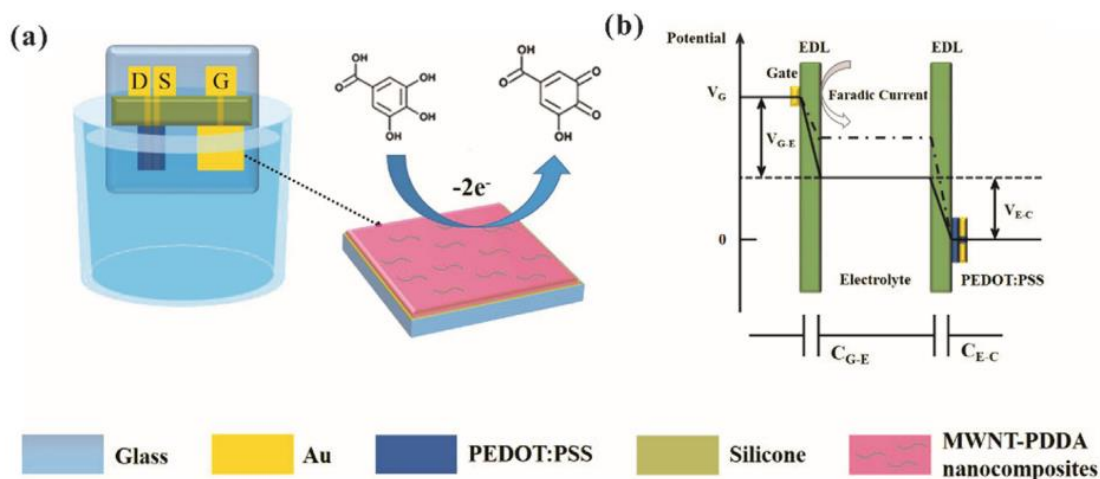


Fig. 1.12 – An OEET-based gallic acid sensor, in which the gallic acid reacts with the gate electrode functionalized surface. The oxidation of the gallic acid causes a variation in the potential drop between the gate and the channel [27].

In the case of redox enzymes, they cause a selective oxidoreduction of the analyte, that can be a:

- direct electroreduction of one of the enzyme products on the gate;
- indirect (mediated) electron transfer between the gate and the redox centre of the enzyme;
- direct electrical connection, when possible, between the gate and the redox active centre of the enzyme.

The first type of reaction often exploits the re-oxidation of H_2O_2 , a co-product of some oxidase enzymes, as the glucose oxidase (GOx). This oxidation corresponds to the transfer of electrons from the molecule to the gate, which in turn causes a shift of V_{gs}^{eff} , decreasing V_{offset} and then reducing the drain-source current [28] (an example in Fig. 1.13).

The last two kinds of reaction have not been frequently used in research works. It's reported one example for each category. It can be seen that a mediator, ferrocene [29], was used for the transfer of electrons from the active enzymatic site to the gate (Fig. 1.14) and further how GOx can be directly placed in contact with the PEDOT:PSS film, instead of with the gate electrode [30] (Fig. 1.15).

Crucial in these systems is the construction of the high-performance gate electrode for a high-sensitive sensing.

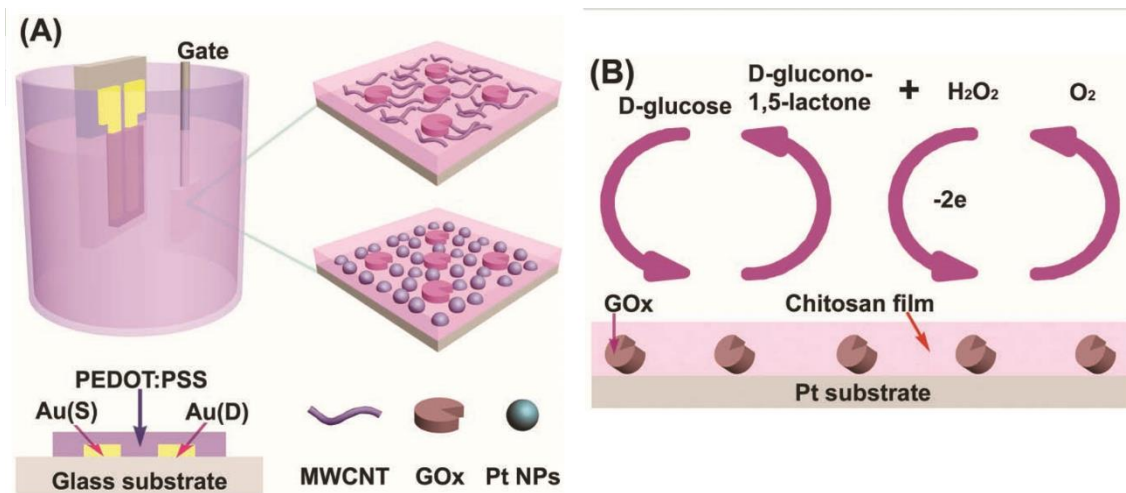


Fig. 1.13 – An example of glucose biosensor, in which the gate electrode contains GOx inside of a chitosan film. The reaction between glucose and GOx causes the transfer of two electrons to the gate surface [28].

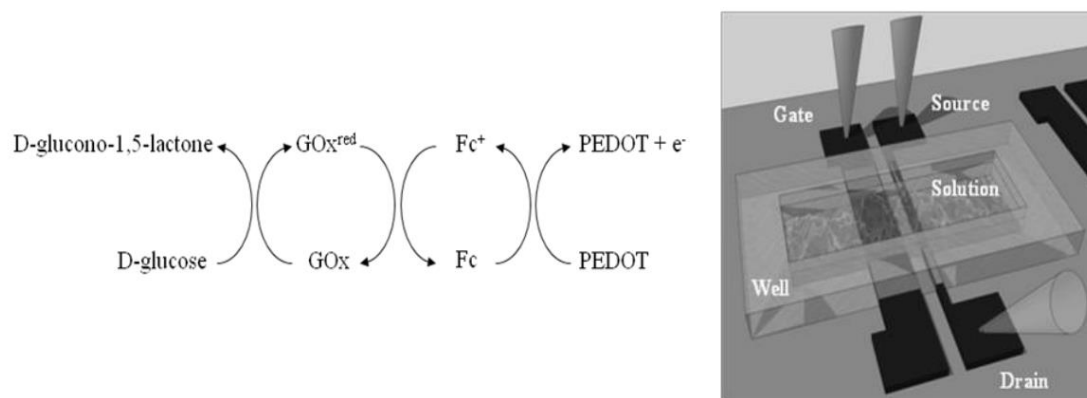


Fig. 1.14 – The mediation of ferrocene was exploited to transfer electrons on the channel surface [29].

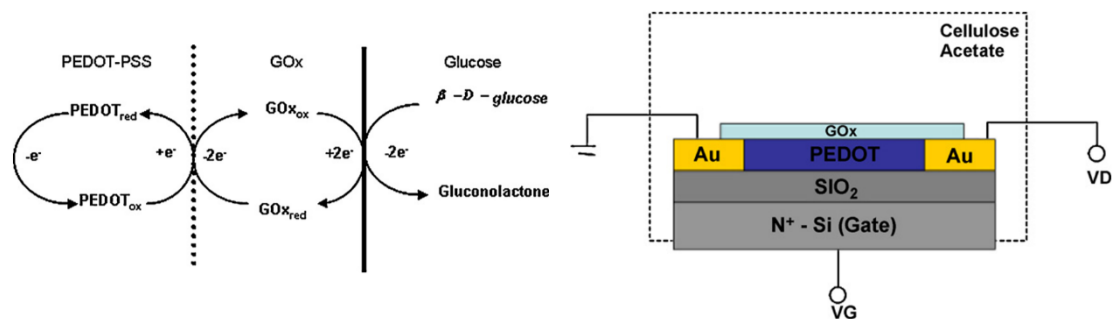


Fig. 1.15 – The GOx located on the PEDOT:PSS channel transfers directly electrons to the polymeric material [30].

1.5 State-of-the-art in biosensing

In the following sections, the main fabrication processes, the design strategies and two classifications for OECT biosensors (according to the sensitive interfaces or to the biological application of the devices reported in literature) are analysed.

1.5.1 Fabrication techniques

The creation of the source-drain electrodes, the deposition of the polymeric channel, the preparation of the gate electrode and, eventually, the bio-functional modification are the main steps involved in OECT fabrication.

The most relevant difference in the fabrication techniques concerns the method through which the semiconducting film is formed and patterned.

Here, the methodologies for the PEDOT:PSS deposition are reported and briefly described.

- **Spin coating** is the most used fabrication technique for OECT production. It consists in distributing fluid solutions on a fixed substrate using a spinning plate. To create a specific pattern of material on the substrate, several photolithographic steps are required. Typically, two approaches may be followed: a top-down (or subtractive) and a bottom-up (or additive) approach. In the first one, the solution is deposited on the substrate and subsequently patterned, generally by using a protective photoresist on the solution film, which is then removed by etching. In the second one, the solution is spin-coated on a prepatterned layout, made by a sacrificial layer of photoresist, that is then removed by lift-off, leaving the solution film only on the required zones. After that, devices are annealed for at least an hour, at temperatures higher than 120°C [9]. Through this fabrication technique, a good uniformity, control and reproducibility of the coating thickness over the whole substrate may be reached. The equipment is commercially available and low cost, the time-consuming delays are absent and the operation is very fast (only a few seconds per coating). On the other side, the spin coating presents some disadvantages, such as the waste of material and

the necessity of a small and rigid substrate. In fact, less than 10% of the applied solution remains after centrifugation. Furthermore, large substrates are not able to be spun at a high rate, allowing the film to thin and dry in a short time. The rigidity of the substrate is strictly necessary to ensure uniformity of the covering [31].

- **Ink-jet printing** is an attractive digital technique, that allows the utilization of relatively small quantities of inks, not requiring a physical printing master. It can be adapted to different size of production scale from small-scale substrates to large-area production. The substrates for printing may be also flexible and wide. This technology can be applied in microelectronics, but needs inks with special properties, such as low viscosity and high surface tension. This printing technique allows direct patterning, low material waste, low cost, and close composition control, that made it an increasingly technique accepted for many industrial and scientific applications. It represents the only true non-impact printing process, in which a fluid ink is sprayed through very fine nozzles, and the resulting ink droplets directly form an image onto rigid or flexible substrates with a certain lateral resolution. Nevertheless, there are not examples of inkjet-printed OEET for the detection of metabolic analytes, at this moment [9].
- **Screen-printing** has been practiced for a long time in electronics industry and now is still used for printing metallic interconnects on printed circuit boards. The screen printer owns a very simple setup, composed by screen, squeegee, press bed, and substrate. In flatbed assembling, the ink poured on the screen is squeegeed to move across the screen resulting in its transfer through the stencil openings to the substrate beneath it. Flatbed screens can be substituted by rotary screen for continuous processing in which the web of the screen is folded while the squeegee and ink are placed inside the tube. It allows the usage of high viscosity inks (0.5-5 Pa·s) and the printing on flexible substrates [32]. For polymers, like PEDOT:PSS, an annealing of few minutes is needed after the printing [9].

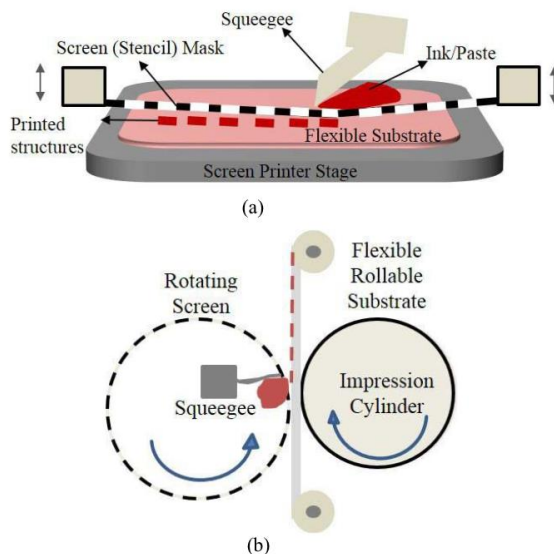


Fig. 1.16 – Scheme of the working principle of screen-printing: flatbed method (a) and rotary screen (b) [32].

- **In-situ polymerization** consists in the synthesis of a polymeric structure, starting from the deposition of a precursor solution on the substrate; then, the addition of the initiator triggers the beginning of the reaction, completing the polymeric chains assembly. This technique requests low viscosity pre-polymers (less than 1 Pa·s), a short period of polymerization, and no formation of side products during the polymerization process and is widespread in production of polymer nanocomposites from nanoparticles. For PEDOT:PSS, an aqueous solution of EDOT (the monomer) and PSS is mixed and the resulting mixture is activated in a solution of sodium persulfate and ferric sulfate [33].

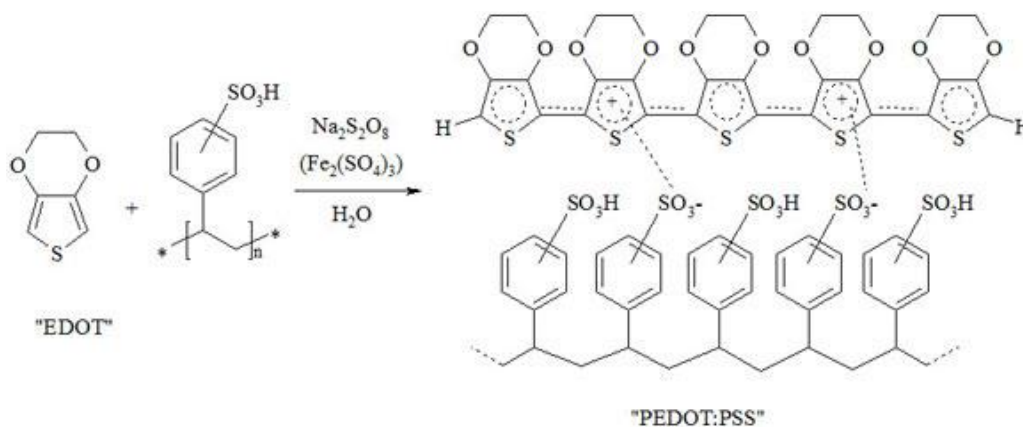


Fig. 1.17 – Polymerization of EDOT with PSS [33].

The choice of the deposition technique must take into account the final desired pattern of the polymeric channel. Several studies have confirmed the direct relationship between the transconductance and the volume of the channel [34]:

$$g_m \propto \frac{WT}{L}$$

The transconductance g_m is defined as the first derivative of the transfer characteristic curve (I_{ds} - V_{gs}) and represents a fundamental parameter in biosensing. Due to this correlation, the channel of the OECT must be fabricated considering the relationship among these three parameters (width, length and thickness).

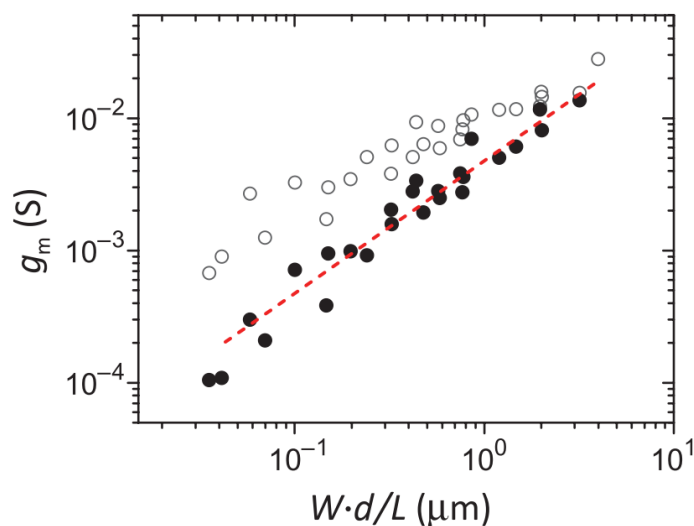


Fig. 1.18 – Variation of transconductance is a function of the volume of the OECT channel. The white dots represent the peak g_m at $V_{ds} = -0.5V$ and V_{gs} corresponding to the maximum transconductance. The black ones are the transconductance at saturation at $V_{gs} = 0.4V$ and V_{ds} that corresponds to saturation [34].

1.5.2 Sensing interfaces

The most recent OECTs development research has focused especially on the two sensing interfaces for signal monitoring, exploiting the phenomena of polarization of such interfaces: one is the electrolyte-channel interface and the other is the gate-electrolyte [3]. This is due to a better possibility to realize a wide spectrum of different devices, modulating their fabrication and design

parameters, often using a basic sensing platform. A PEDOT:PSS-based OEET is a versatile device that can be used for several bio-applications.

As seen above, one of the fundamental proprieties of the OEETs, that makes them very useful for biosensing applications, is the ability of modulating the drain-source current (I_{ds}) depending on interfaces polarization.

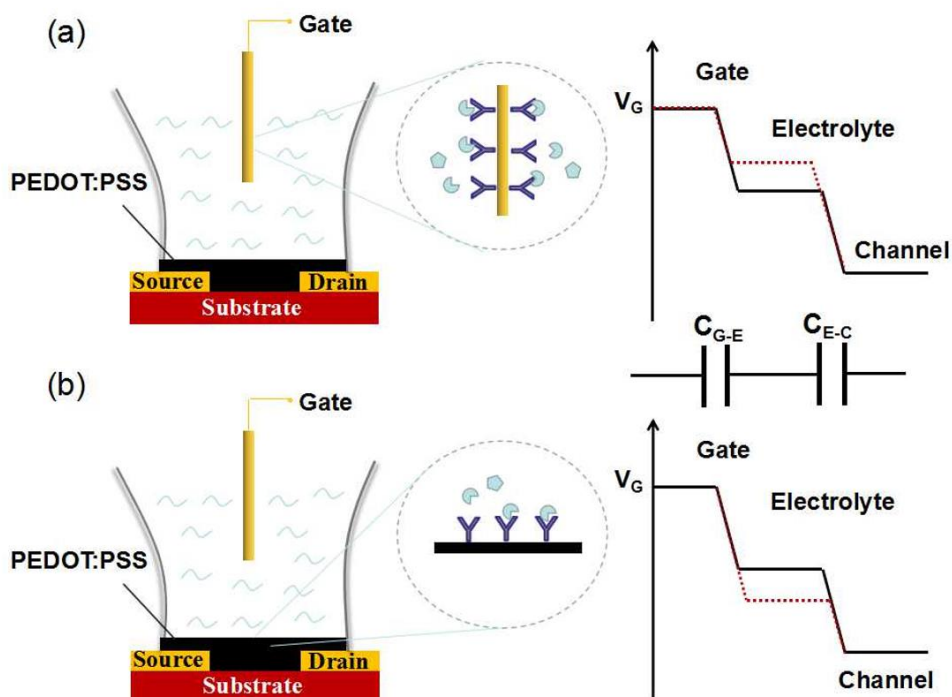


Fig. 1.19 – The two sensing interfaces of OEET: the gate and the channel surfaces. The immobilized target molecules cause a change in the capacitances between the different interfaces, modifying the drop in the gate voltage [3].

1.5.2.1 Functionalization of Channel Surface

Immobilization of various specific biorecognition elements on the PEDOT:PSS channel of OEETs allows a relevant improvement in the selectivity and sensitivity of the biosensor. Biomolecules, such as enzymes, antibodies and nucleic acids have been successfully integrated with the conductive polymer for specific bioelectronic applications.

The following table gives an overview of the developed platforms, employing grafting identification molecules on PEDOT:PSS films.

Gate	Target	Channel Functionalization	Performance	Ref.
N ⁺ -Si	Glucose	GOx	Linear range 1.1-16.5 mM	[30]
Ag/AgCl	<i>E. coli</i> O157:H	Anti- <i>E. coli</i> O157:H7 antibodies	Detection limit 10 ⁻³ cfu/mL	[23]
Ag/AgCl	Human influenza virus	Trisaccharides	Detection limit 0.025 HAU	[35]
Ag/AgCl	PSA-ACT complex	Au NPs + PSA pAb	Detection limit 1 pg/mL	[36]
Ag/AgCl	K ⁺	K ⁺ ion-selective membrane	Linear range 10 ⁻⁴ -10 ⁻¹ M	[25]

Tab. 1.1 – OECT developed platforms involving the channel functionalization.

1.5.2.2 Functionalization of Gate Surface

Several problems are related to the above-mentioned biosensing technique. In fact, the functionalization of the PEDOT:PSS channel may cause unwanted effects:

- the inhomogeneity of the biomolecule distribution may be limited by the low bio-functionality of PEDOT:PSS;
- the conductivity of PEDOT:PSS may be disrupted after biomolecule immobilization;
- biomolecules may denature after high-temperature hard baking.

Thus, the modification of the gate electrode surface is the subject of a large amount of research works. Furthermore, this second kind of grafting shows the following advantages:

- it does not affect the performance of the channel;
- a variety of modification methods can be performed without considering the deleterious effects to the PEDOT:PSS
- a wide choice of metal or semiconductor materials (Au, Pt, Ag, Ag/AgCl, ITO, TiO₂ nanotube) can be used as gate electrodes.

In addition, the gate electrode and the channel (as well as the remaining parts of the device) can be individually and conveniently fabricated.

The table below shows notable applications, involving metal and semiconductor gate surfaces.

Gate	Target	Gate Electrode Functionalization	Performance	Ref.
Au	Amino acid	Molecularly imprinted polymer	Linear range 300-10 μ M Detection limit 2 nM	[37]
Au	Interleukin-6	IL-6 antibodies	Detection limit 2 ng/mL	[24]
Au	Gallic acid	PDDA + carbon nanomaterials	Linear range 1-10 μ M Detection limit 10 nM	[27]
Au	Glucose Lactate	GOx/LOx + Pt NPs	Detection limit 0.1 μ M glucose 1 μ M lactate	[38]
Pt	Epinephrine	Nafion + SWNTs	Detection limit 0.1 nM	[39]
Pt	Dopamine	Nafion + graphene	Linear range 5 nM-1 μ M Detection limit 5 nM	[40]
Pt	Glucose	CHIT/GOx/Pt-NPs	Detection limit 5 nM	[28]
PEDOT:PSS	Glucose Lactate Cholesterol	GOx LOx ChOx	Linear range 0.02-1 mM glucose 0.1-2 mM lactate 0.01-0.7 mM cholesterol Detection limit 10 μ M glucose 50 μ M lactate 10 μ M cholesterol	[41]
PEDOT:PSS	Ascorbic acid	-	Detection limit 80 μ M	[42]
PEDOT:PSS	Lactate	Lox + CHIT + Fc	Linear range 30-300 μ M Detection limit 10 μ M	[43]
PEDOT:PSS	Glucose	GOx	Linear range 10^{-7} - 10^{-2} M Detection limit 10^{-3} μ M	[44]
Ag/AgCl	Bacteria	-	Detection limit 10^{-3} cuf/mL	[23]
Ag/AgCl	K ⁺ Ca ²⁺ Al ³⁺	-	Linear range 10^{-3} - 10^{-1} M	[22]
ITO	DNA	CdS QDs + ssDNA probe (420 nm light illumination)	Linear range 10^{-15} - 10^{-9} M Detection limit 10^{-15} M	[45]
Glass carbon electrode	Sialic acid	Poly(3-aminophenylboronic acid)	Linear range 8 μ M-2mM Detection limit 8 μ M	[46]
TiO ₂ nanotube arrays	Glucose	Nafion/GOx/Pt-NPs	Linear range 100 nM-5mM Detection limit 100 nM	[47]
TiO ₂ nanotube arrays	Chemical oxygen demand	UV-LED as excited light source	Detection limit 0,01 mg/L	[48]
PEDOT:PSS	Dopamine	All-PEDOT:PSS OEET	Detection limit 6 μ M	[49]
Pt NPs	Glucose	Platinum nanoparticles gate electrode (integrated with a microfluidic channel)	Detection limit 10^{-7} M	[50]

Pt	Hydrazine	Concentric-electrode OECT	Linear range 0.1 M-10 ⁻⁵ M Detection limit 10 ⁻⁶ M	[51]
----	-----------	---------------------------	--	------

Tab. 1.2 – OECT platforms developed by functionalization of the gate electrode.

1.5.3 Biological classification

From a biological point of view, all the above mentioned OECT-based platforms can be further divided in different groups, related to the involved biomolecules in sensing [1]:

- **Ion sensing:** since the OECTs allow a transfer of free ions in the whole bulk of the electrolyte, they can be suitable for ion detection in aqueous solution but also in other ionic and electronic media, e.g. gel and ionic liquid.
- **Enzymatic biosensors:** this is the most widely used application of OECT in biosensing. In this typology the enzymes are immobilized on the gate electrode and catalyse the substrates into enzymatic product, gaining or losing electrons on the electrode. These electrical signals are transferred to the gate electrode, leading to channel current changes. The charge neutrality in the whole circuit, considering both the ionic and the electronic circuit, is maintained by a cation which penetrates into the polymeric channel and replaces the role of the cationic component (PEDOT⁺) compensating the anionic constituent (PSS⁻), leading to a change of V_{gs}^{eff} . Due to this mechanism, the drain-source current across the channel is logarithmically proportional to the concentration of enzymatic substrates.
- **Immunosensors:** in this kind of biosensors the biorecognition elements are antibodies of the immune system, that detect the concentration of their own specific antigen in the electrolyte solution. Two types of immunosensors are widely accepted, as in immunoassay: the competitive and the sandwich types. The immobilized biorecognition molecule can be either an antibody or an antigen, in competition immunosensors. For the sandwich type, a primary antibody is bound on the platform of a sensor, the specific antigen marker is in the sample solution and the secondary antibody reacts with the antigen

bound. The detectable and low noise signals are generated through enzymes, redox substrates or nanomaterials.

- **Aptamer sensors:** Since aptamers own a high specificity, even superior to antibodies, aptamer-based OECTs allow the fabrication of label-free DNA sensors, in which single stranded DNA is immobilized on the gate as probes, detecting the complementary DNA targets inside of the electrolyte solution. These devices can be potentially applied also in microRNA analysis.
- **Artificial receptors-coupled sensors:** Artificial receptors possess comparatively higher chemical stability than natural receptors under physiological conditions, thus they represent an alternative and an overcoming of the natural molecules, like antibodies and enzymes. A combination between OECTs and molecular imprinted polymers (MIPs) is also possible, in order to prepare wearable devices with a molecularly or ions selective membrane.
- **Cell monitoring:** OECT can detect the gradients of cells located on the channel or gate surface of the device, due to its sensitivity to the surface charge changes induced by the adhesion of cells. Cell-based OECT may promote the cell relevant testing, such as screening drugs and testing toxic substances, while the cell potential recording can predict the adhesion of cell and, eventually, the epithelium formation. In very recent studies, OECT can detect glycans on the cell surface, owning a modified gate which can capture cancer cells, even at very low concentrations.

2.

Materials and methods

In this chapter all steps of OECTs fabrication will be explained in sequence, from the processing of the silicon wafer to the final stages of the functionalization for biosensing experimental measurements. Finally, the last paragraph will describe the set-up used for the measurements.

2.1 Device overview

The final goal of all the fabrication processes is to realize a platform, composed by two parts: the micro-electronic basement and the chamber for the electrolyte, that will be equipped with the holder for the functionalized gate electrode.

Two different structures were produced in order to satisfy different goals of this thesis work:

- a six-OECTs platform (Fig. 2.1), constituted by the electronic substrate, the chambers for the electrolyte and an Ag/AgCl wire or a cover; this one is used

- for different purposes: device characterization, comparison of different treatments and fabrication techniques, and first experimental measurements;
- a five-OECTs platform (Fig. 2.2), composed by the substrate, the electrolytic chamber, the cover and a pre-fabricated external rigid case; this one is used for real-time detection measurements.

They will be called static platform (SP) and real-time platform (RTP), respectively.

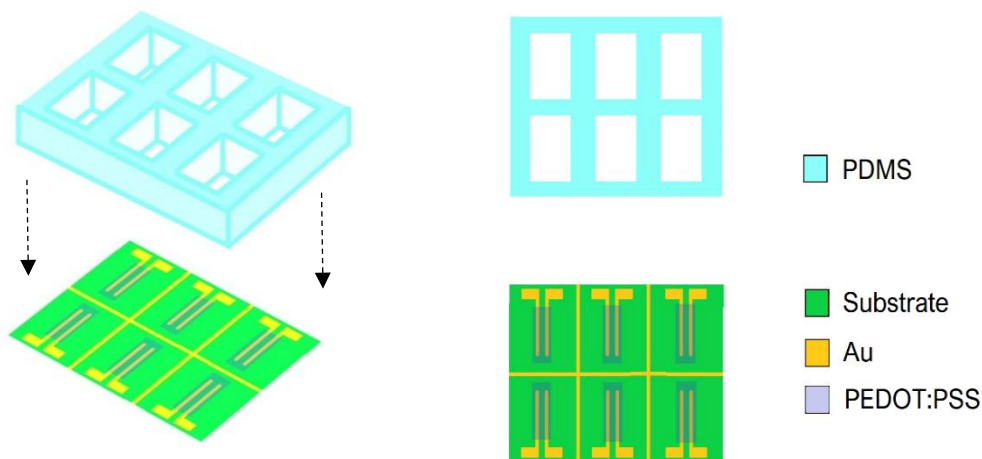


Fig. 2.1 – Representation of the six-OECTs static platform: schematic three-dimensional view (left) and vision from above (right).

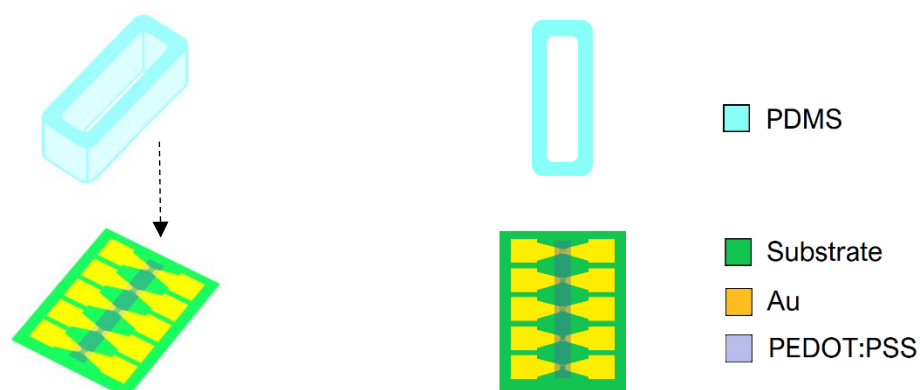


Fig. 2.2 – The five-OECTs real-time platform: a 3D schematic figure (left) and a view from above (right).

The fabrication and characterization steps were conducted both in class 100 and 1000 cleanrooms and in the additive manufacturing room at Chilab (Materials

and Processes for Micro & Nano Technologies Laboratory), located in Chivasso (TO). The functionalization and the corresponding measurements were conducted in the chemical and biochemical labs at Nanosciences laboratory, within the DISAT (Politecnico di Torino).

2.2 Device fabrication

At the beginning of this section the fabrication of the SP will be discussed in detail. Instead, the preparation of the RTP will be explained in the last part of this section, reporting the fabrication main steps.

The production of the OECTs started from the oxidation of a silicon wafer (5 inch diameter = 125 mm), to obtain a surface layer of silicon oxide (SiO_2), which represents the substrate for the next processing steps.

2.2.1 Metal electrodes

This substrate was then treated with the following techniques for the fabrication of gold electrodes, whose steps are briefly summarized in Fig. 2.3.

10 nm of titanium (which forms the adhesion layer) and successively 100 nm of gold were deposited on the substrate of silicon oxide employing an e-beam evaporator (ULVAC EBX-14D).

Then, a positive photoresist (AZ 1518 from Microchemicals) was spin-coated with SPIN 150i spin coater at 500 rpm for 5 s and subsequently at 4000 rpm for 30 s, covering the entire surface of the wafer (the spin coating working principle will be explained in Section 2.2.2.4). Then it was placed on the hot plate for 1 min at 110 °C (soft-bake).

The UV-mask, whose model is shown in Fig. 2.4, contains the pattern for the definition of the gold electrodes and was placed on the substrate covered by the photoresist, using the Neutronix Quintel NXQ-4006 Mask Aligner (Fig. 2.5). It was exposed to UV light, with a power density of 11 mW/cm², for 5 s. Through this step, the areas of the photoresist exposed to the UV-rays become soluble in

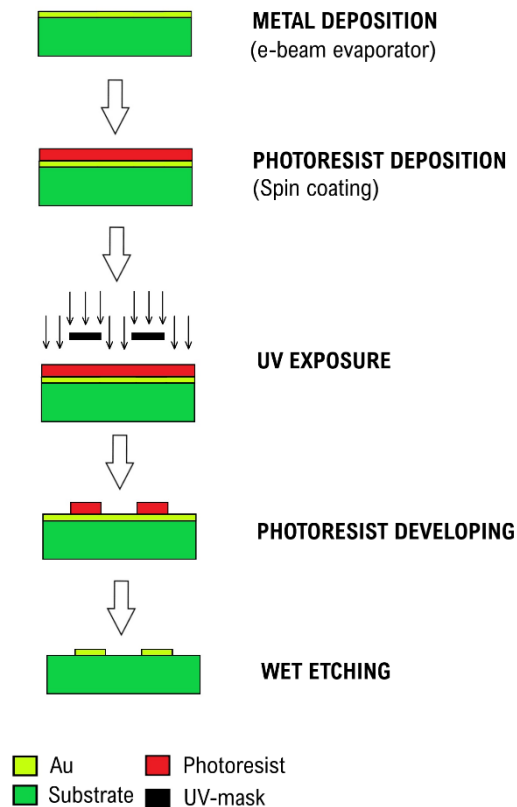


Fig. 2.3– Realization of the gold electrodes on the silicon oxide substrate.

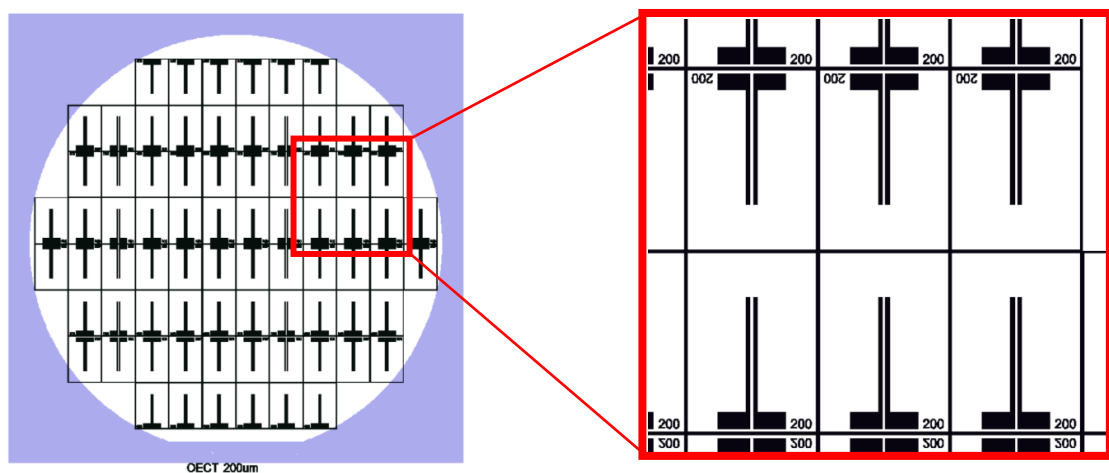


Fig. 2.4 – UV-mask containing the pattern for the gold electrodes for the six-OECTs platform. It allows the preparation of more than 60 OECTs from one 5-inch wafer. This model was obtained thanks to CleWin5 software.

the developer solution. The UV-mask protects the zones where the gold must be preserved.

The photoresist was developed in AZ 400K developer solution (from Microchemicals), composed by H₂O:AZ400K 3:1, for about 35 s. The samples were rinsed in DI water and then placed on the hot plate for 1 min at 115 °C (post-bake).

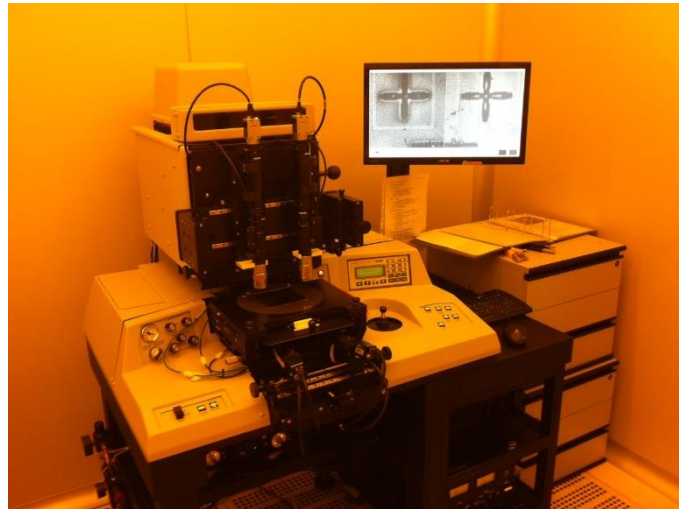


Fig. 2.5 – The NXQ-4006 Mask Aligner

The excess metallic material was removed through a process of wet etching: for gold etching the samples were immersed for few seconds in an aqueous solution of KI/I₂, while a solution containing HF was used for titanium etching [52].

At the end, the wafer was cut, obtaining the maximum number of six-devices platforms (Fig. 2.6). From this point, the fabrication steps were applied on every single device platform.

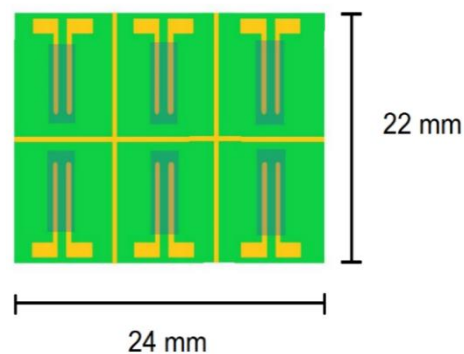


Fig. 2.6 – Dimensions of the SP containing six OECS.

2.2.2 PEDOT:PSS deposition

In this work different solutions containing PEDOT:PSS were deposited, and also different techniques and treatments were followed for the patterning of the semiconductor channel.

With regard to the PEDOT:PSS solution, different commercial solutions are available on the market, with specific compositions and production processes for a wide spectrum of applications. Additives, adhesion layers and/or specific treatments may improve the properties of the polymeric film. In this study, it was investigated the effect of a treatment with sulfuric acid (after the deposition of the PEDOT:PSS film) and, separately, the effect of the addition of (3-glycidyloxypropyl)trimethoxysilane (GOPS) to the polymeric solution, on the device performances.

The following paragraphs will describe both the preparation of the polymeric solutions (Section 2.2.2.1) and the two deposition techniques involving the different prepared solutions (Sections 2.2.2.2 and 2.2.2.3) to obtain the same pattern, shown in Fig. 2.7a.

The channel (Fig. 2.7b) was patterned with an high width/length ratio ($W/L=30$), in order to obtain a good transconductance.

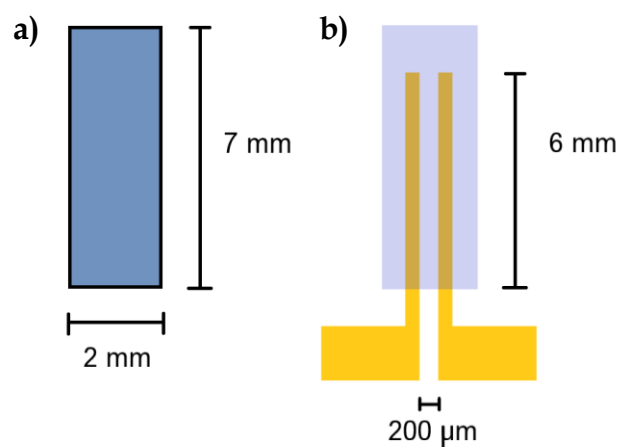


Fig. 2.7 – Pattern of the PEDOT:PSS pattern for each device (a) and the corresponding channel dimensions (b).

Concerning the PEDOT:PSS deposition, in this thesis work spin coating and ink-jet printing were employed in parallel for the fabrication of different samples.

In order to perform a better comparison between these fabrication techniques, the same two solutions (pure Clevios and Clevios with GOPS addition) and the same post-treatments were applied, changing only the deposition technique for the realization of the polymeric channel.

The comprehensive scheme of the developed devices is reported in Table 2.1.

SOLUTION PREPARATION	CLEVIOS		CLEVIOS + GOPS	
PEDOT:PSS DEPOSITION	SPIN COATING	INK-JET PRINTING	SPIN COATING	INK-JET PRINTING
POST-TREATMENT	H ₂ SO ₄	H ₂ SO ₄	none	none

Tab. 2.3 – Summary of the different treatments and techniques. The various steps (solution preparation, PEDOT:PSS deposition and post-treatment) correspond to the consecutive phases of the deposition process, from top to bottom.

Therefore, four different devices were fabricated, combining the deposition techniques and the treatments for the enhancement of some properties of the PEDOT:PSS channel (the GOPS addition and the sulfuric acid post-treatment):

- OECTs with polymeric channel of Clevios, deposited by spin coating and submitted to the sulfuric acid treatment after the deposition;
- OECTs with polymeric channel of Clevios, deposited and patterned by ink-jet printing and submitted to the sulfuric acid treatment after the printing;
- OECTs with polymeric channel of Clevios and an addition of GOPS, deposited by spin coating and patterned by photolithography, without other treatments;
- OECTs with polymeric channel of Clevios+GOPS, deposited and patterned by ink-jet printing, without other treatments.

In order to prove the necessity of the H_2SO_4 treatment and the GOPS addition, other two samples without both of these improvements were fabricated:

- an OECT with polymeric channel of Clevios, realized by spin coating
- an OECT with Clevios, made by ink-jet printing.

2.2.2.1 Solutions preparation

Clevios™ PH1000 (from Heraeus) was used as the main component of the polymeric film. This latter is an aqueous PEDOT:PSS (1:2.5) dispersion, with 1.3% of solids content and a viscosity between 15 and 60 mPa·s, as reported in the datasheet [53]. The specific composition and production process make Clevios PH1000 a better dispersion for electronic devices than other commercial PEDOT:PSS solutions [17]. For the first solution, it was used pure Clevios PH1000 (that will be called *Clevios*, in the following) and for the second one 1% *v/v* of GOPS was added¹ (this solution will be named *Clevios+GOPS*).

As explained above, for a better comparison between the deposition techniques, the same two solutions were prepared and used both for spin coating and ink-jet printing. The two solutions were treated before their use, due to some restrictions requested by the ink-jet printing system. The ink that can be used in this kind of printer might own specific characteristics [54]:

- viscosity: 0.5 ÷ 40 mPa·s
- surface tension: 20 ÷ 70 mN/m.

Fluids with properties outside these ranges may be dispensed using this ink-jet apparatus, but with increased difficulty and/or decreased performance. In fact, the most problematic aspect of this printing system is the occlusion of the nozzle, due to undesired lumps or particulate material that may block the ink flow, the driving pressure waves and thus the drop formation. For this reason, the polymeric solutions must be treated, before their use, in order to remove small particles or filaments or, if necessary, reduce the viscosity of the fluid.

¹ This solution is composed of 76% *v/v* Clevios PH1000, 19% *v/v* ethylene glycol, 4% *v/v* dodecylbenzene sulfonic acid, 1% *v/v* GOPS [51]

In this case, the viscosity of Clevios PH1000 exceeds the required range of this quantity for this printing system. In fact, the direct use of this untreated commercial solution was very difficult: the nozzle was often completely clogged by some thin filaments present in the PEDOT:PSS solution, that prevented the regular ink flow. This phenomenon implies repeated interruptions within the printing process and the necessity of starting a cleaning procedure, until the blockage is removed. These frequent stops cause an important decrease of the throughput in OECTs fabrication. The presence of a partial occlusion may also affect the control system of the jet flow. All the printing parameters obtained by an optimization process on the jetting (e.g. the pressure applied on the fluid, the voltage driving waveform and thus the optimization of the drop ejection and the relative dimensions) may be dependent on the reduced diameter of the nozzle, and so they might not be repeatable.

The different solutions were both pre-treated, applying two consecutive steps: sonication and filtering.

Each solution was placed in the digital sonifier Branson SFX 250 (Fig. 2.8). The PEDOT:PSS solutions used in this work underwent a sonication treatment, through a pulse wave with an ON-time of 5 s and an OFF-time of 10 s, for a total ON-time of 20 min. The power was set at 50% of the maximum.

The second step in the ink preparation consisted in the filtering. The sonicated solution was collected by a syringe and then a disposable filter with a pore size of 0.45 μm was applied at the end of the syringe to remove the residual particulate. This step ensures that the residual particulate in the solutions is smaller than 1% of the diameter of the nozzle, which in this case is 50 μm .

These solutions, in closed bottles, must be stored in fridge between 5 and 10 °C. If the solutions freeze, they may become unusable [53].



Fig. 2.8– The dark blue polymeric solution (Clevios) inside the sonifier. The beaker contains water and ice (the blue element behind the solution), to refrigerate the system, due to the high temperature caused by cavitation.

2.2.2.2 Spin coating

The sample is placed on a small platform inside the spin-coater and fixed on it with vacuum. The solution is dropped onto the centre of the sample and the lid of the spin-coater is closed. When the plate starts rotating, the liquid material is distributed on the entire surface through the centrifugal force, covering uniformly the sample and removing the excess (Fig. 2.9). The final thickness of the spin-coated layer depends on the fluid viscosity and on the speed and the time of rotation.

In this specific case a top-down approach has been exploited: the PEDOT:PSS solution is deposited on the samples and then patterned, removing the material where unnecessary [9]. The principal steps of this deposition process are reported in Fig. 2.10.

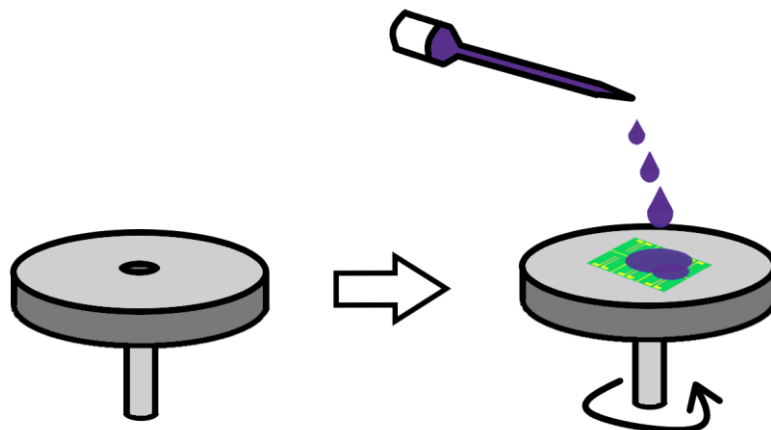


Fig. 2.9 – Schematic representation of spin coating. On the left the plate with the small hole connected to a vacuum pump for the fixing of the sample. On the right: the solution is dripped by a pipette on the device surface.

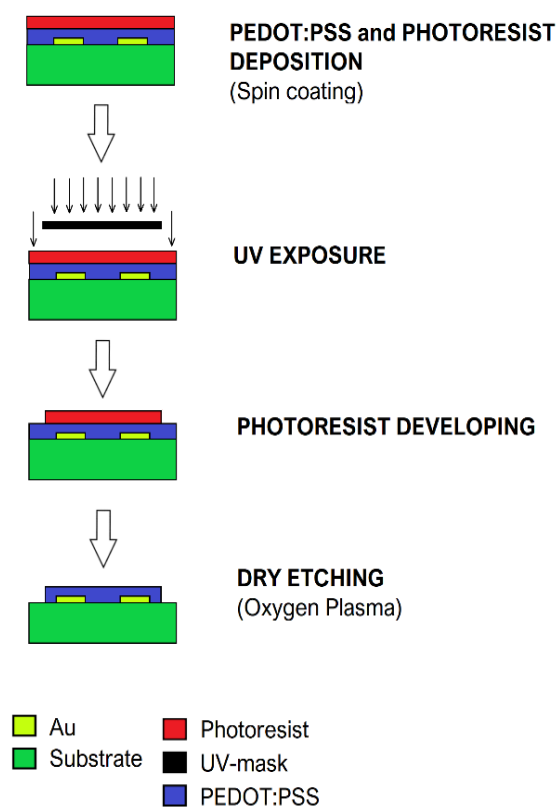


Fig. 2.10 – Principal steps for PEDOT:PSS deposition, involving spin coating technique.

After the preparation of the polymeric solutions, some devices were selected from the whole group for the deposition of an adhesion layer of GOPS². These samples were placed in the spin coater and the liquid solution of GOPS was dropped onto the centre of each sample by a pipette, then a rotation of 4000 rpm was applied for 30 s. Some of these samples were covered in the following steps only with the *Clevios*+*GOPS* solution and the residual ones were then used also for the ink-jet printing technique.

At this point of the process, the samples without the adhesion layer were covered with the *Clevios* solution, while the others with *Clevios*+*GOPS*. Each solution was spin-coated at 2000 rpm for 30s. The samples were then dehydrated on a hot plate at 120°C for 15 minutes, in order to evaporate the solvent.

Some samples among the devices with the spin-coated *Clevios* were selected for the H₂SO₄ post-treatment and thus were bathed in a 100% H₂SO₄ concentrated solution for 10 min, rinsed in deionized (DI) water and then placed on a hot plate at 120°C for 3 min. These devices will be called *Clevios*+H₂SO₄.

From here, the described processes were applied to all devices (*Clevios*, *Clevios*+H₂SO₄, *Clevios*+*GOPS*). A positive photoresist (AZ 9260 from Microchemicals) was spin-coated at 500 rpm for 5 s, and subsequently at 2400 rpm for 60 s. The samples were placed on the hot plate at 100°C for 10 minutes for soft-baking, then they were maintained at room-temperature for an hour, to perform hydration.

With the UV-mask reported in Fig. 2.11, all devices were exposed at 11 mW/cm² for 80 s in the NXQ-4006 Mask Aligner.

The samples were immersed in the AZ 400K developer solution for 8 min and rinsed with DI water. After that, they were dried on a hot plate at 100 °C for 3 min.

² This solution also includes toluene : acetic acid (200:1)

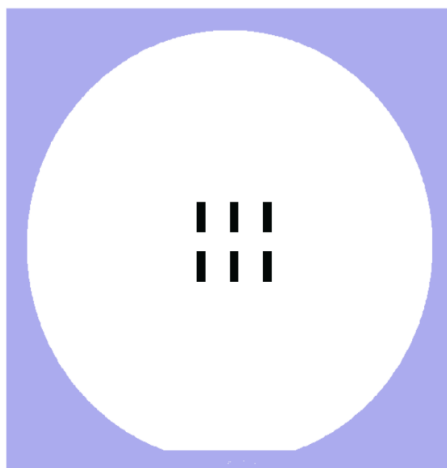


Fig. 2.11 – The UV-mask with the pattern of PEDOT:PSS channels.

Then they were treated with oxygen plasma etching (Plasmafab 508, reported in Fig. 2.12a), proceeding with consecutive steps of 5 min and checking the cleanliness of the surface of the samples in those zones where the polymeric film was not requested. After 5 cycles of 5 min of oxygen plasma the samples were rinsed in acetone in order to remove the residual resist on the surface. Then, they were dried with nitrogen and the thickness of the PEDOT:PSS film was finally measured with a profiler (Tencor P-10 Surface Profiler, Fig. 2.12b).



Fig. 2.12 – Tencor P-10 Surface Profiler (a) and Plasmafab 508 for oxygen plasma etching (b).

The developed devices were placed in oven at 150°C for 2 hours to perform annealing; after that they were ready for the installation of the PDMS chamber.

The times for each step and the total duration of this process are summarized in Table 2.2.

	<i>Clevios</i>	<i>Clevios+GOPS</i>
Spin coating (GOPS+toluene)	-	30 s
Spin coating (polymeric solution)	30 s	30 s
Dehydration	15 min	15 min
H ₂ SO ₄ treatment	13 min	-
Spin coating (photoresist)	65 s	65 s
Soft baking	10 min	10 min
Hydration	1 h	1 h
UV exposure	80 s	80 s
Developing	11 min	11 min
Dry etching	25 min	25 min
TOTAL	~ 2 h 30 min	~ 2 h 15 min

Tab. 2.4 – The total time estimation for the spin coating deposition technique for both involved solutions.

In the following sections, these two different samples will be called, for simplicity, *H₂SO₄_spin* and *GOPS_spin*.

2.2.2.3 Ink-jet printing

The two main ink-jet printing methods are drop-on-demand (DOD) and continuous ink-jet printing (CIJ). In this work a piezoelectric drop-on-demand (DOD) ink-jet mode was used, whereby the deformation of some piezoelectric material causes the change of the ink volume inside a pressure chamber to generate a pressure wave that propagates toward a nozzle. The term DOD refers to the release method: the voltage pulse to the piezoelectric element is applied only when a drop is desired. The piezoelectric DOD mode is very suitable for different inks and for the application of different materials on different kinds of substrates, due to the fact that ink degradation is no longer a concern since the pressure wave is generating strictly through mechanical deformation [31].

In this type of system, the droplets are produced by electromechanically-induced pressure waves [56]: a volumetric change in the fluid is induced by the application of a voltage pulse to the piezoelectric material that is coupled to the fluid. This volumetric change causes pressure/velocity transient to occur in the fluid, producing a drop that is released by the nozzle [55].

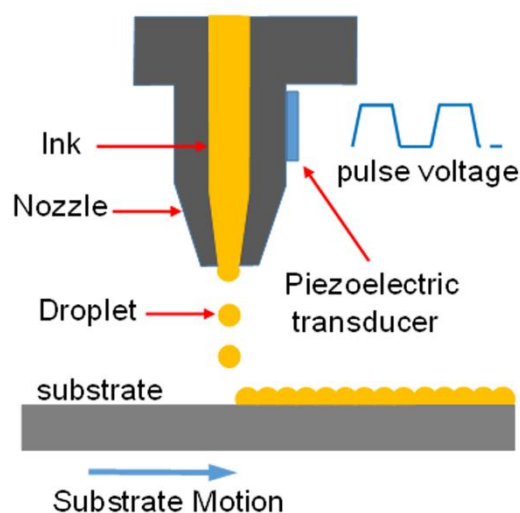


Fig. 2.13 – Scheme of the working principle of ink-jet printing in piezoelectric DOD mode [56].

The ink-jet printer used for this work is Microfab Jetlab 4 (Fig. 2.14), that allows the printing of simple elements (such as dots, lines of arrays of drops) and also patterns from a digital model. The optimization of the printing parameters and the final printing settings were reported in details in the following chapter. The printer equipment system, the conversion process from the digital model to the printing script and the alignment process between the model and the device on the printing area are reported in the Appendix.

The samples without the GOPS adhesion layer were placed in an ultrasonic bath in isopropyl alcohol (IPA) for 15 min, then were exposed to an oxygen plasma for 2 min, for a better cleaning of the surface. Then they were placed, one by one, on the printing platform. The *Clevios* solution was loaded, the jetting was regulated and observed by the lateral camera, then the printing was started. After the printing, the sample was placed on a hot plate at 120 °C for 10 min, in order to evaporate the solvent, completely. Then, all printed samples were bathed in pure



Fig. 2.14 – Microfab Jetlab 4 DOD ink-jet printer

H₂SO₄ solution for 10 min, rinsed in DI water and dried on the hot plate for 3 min at 120 °C.

The *Clevios+GOPS* devices realized with ink-jet printing do not need an initial oxygen plasma treatment, due to the presence of the GOPS adhesion layer. The *Clevios+GOPS* solution was loaded in the reservoir, and the corresponding jetting parameters were set.

All printed samples underwent an annealing process at 150°C for 2 hours in oven, making them ready for the installation of the PDMS chamber.

Table 2.3 summarizes the steps involved in the ink-jet printing process.

It must be remembered that the ink-jet process requires the preparation of the solutions, but also specific commercial inks are available on the market, so this initial step might be avoided. The choice of the same solutions used for the spin-coating technique and adapted for this printing systems was only due to a better comparison between the deposition techniques, as explained previously.

	<i>Clevios</i>	<i>Clevios+GOPS</i>
Spin coating (GOPS adhesion layer)	-	30 s
Oxygen plasma	2 min	-
Printing	10 min	5 min
Solvent evaporation	10 min	-
H ₂ SO ₄ treatment	13 min	-
TOTAL	~ 35 min	~ 5 min

Tab. 2.3 – Estimation of the printing process duration for the two inks.

The two samples fabricated by ink-jet printing will be named from this point *H₂SO₄_ink* and *GOPS_ink*.

2.2.3 PDMS chambers

The PDMS parts of the devices were realized using PMMA moulds, as seen in Fig. 2.15.

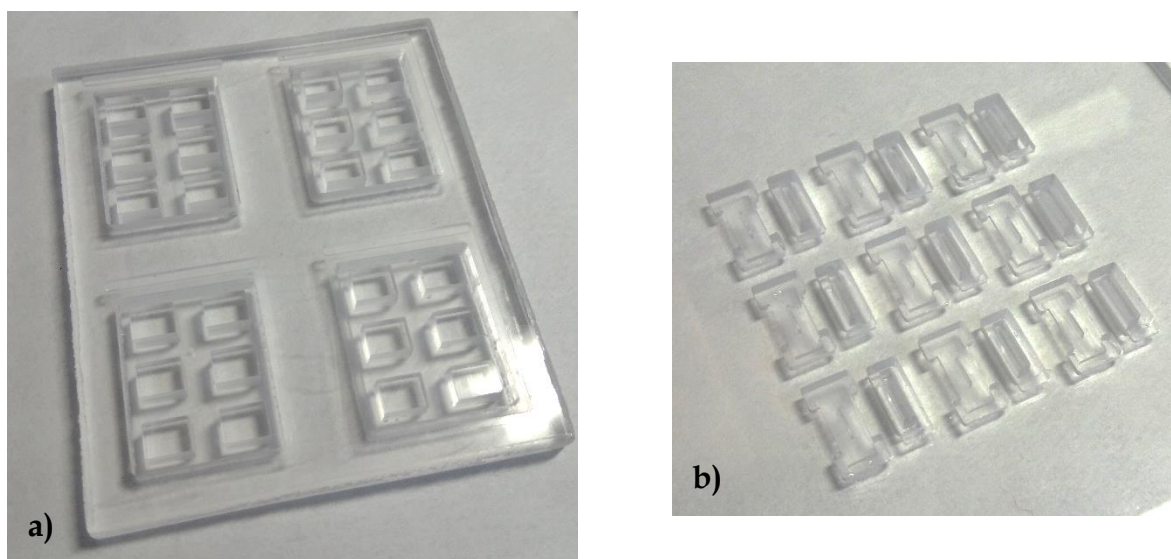


Fig. 2.15 – The moulds for the different PDMS chambers: the one for the SP chambers (a) and the other for the RTP (b).

A solution of Sylgard 184 Silicone Elastomer Base and Curing Agent (10:1) was mixed in a beaker for a few minutes. In order to remove the air bubbles trapped during the stirring, the beaker was placed in a desiccator for about 10 minutes under vacuum. After checking the removal of the bubbles, the PDMS solution

was dropped in the stamps, put on a hot plate at 65°C for about 2 h and then extracted from the moulds.

For the SP it was fabricated a structure made of six PDMS chambers, where each one can collect 120 μL of electrolytic solution and it makes possible the analysis of six different solutions. The structure is bonded to the electronic substrate, depositing a thin layer of PDMS solution with a small spatula under the solid chambers, placing then the whole system on a hot plate (80°C, 15 min). A single 60 μL chamber was produced for RTP, in order to meet the dimensional requirements of the other biosensors (EGOFET and GFET) and to allow a faster filling. In RTP the PDMS chamber was not bonded, due to the sufficient tightness of the external case.

With the same process, also the lids for each kind of chamber have been fabricated, obtaining the holder for the gold squared gate electrode.

2.2.4 Gate electrode

Two different gate electrodes were realized for the different measurements: an Ag/AgCl wire for the characterisation and a gold squared electrode for the measurements after functionalization.

The first one is realized by electrolysis of a KCl solution, in which an Ag/AgCl reference electrode, an auxiliary electrode and an Ag wire, as working electrode, are immersed. This three-electrode configuration of an electrochemical cell is used to deposit ions on the working electrode from the solution. By imposing a voltage of 0.8 V between the working electrode and the auxiliary for about 500 s, Cl^- ions covered the Ag wire surface immersed in the solution, producing the Ag/AgCl gate electrode, through this equation:



Concerning the other type of electrode, the fabrication started from a silicon oxide wafer. This substrate was covered by 10 nm of Ti and 100 nm of Au with the e-beam evaporator. The wafer was then cut in 5 mm x 5 mm squared pieces. This shape allows an easier handling of the equipment for the functionalization

process and leads to a wider area for immobilization (0.25 cm^2) with respect to a wire electrode.

2.2.5 The real-time platform

The RTP is obtained from an entire wafer, patterned with gold electrodes, as shown below. This wafer underwent a passivation of certain gold parts of it, in order to avoid their direct electric contact with the polymer. The zones preserved by the passivation were the source and drain electrodes and the central area, where are located the channels. Each platform was cut and was treated singularly. The adhesion layer of GOPS and then the solution of *Clevios+GOPS* were spin-coated on the entire surface of the sample. Before the soft bake, the polymeric solution was removed with acetone from above the source and drain contacts. Then the sample was placed on a hot plate for 15 min at $120 \text{ }^\circ\text{C}$. The annealing was completed in oven at 150°C for 2 h. At this point the platform was loaded in the basement of the case. Over the platform, the $60 \text{ }\mu\text{L}$ PDMS chamber and then the cover with the gold squared gate electrode were placed and finally the case was closed.

2.3 Device functionalization

For the detection of proteins, such as biomarkers, the immunosensors represent high-selectivity platforms, in which specific antibodies are immobilized on the sensing surface for the detection of the corresponding antigen. As explained in Section 1.5.2.2, the most advantageous method for the OECT functionalization is the immobilization of antibodies on the gate electrode surface, in order to change the capacitance at the gate-electrolyte interface.

In this work, preliminary measurements were conducted, involving simple immobilized molecules: streptavidin-peroxidase protein and vascular endothelial growth factor (VEGF).

2.3.1 Streptavidin-peroxidase (Stp-HRP)

The streptavidin-peroxidase protein is the streptavidin protein coupled with horseradish peroxidase (HRP). Streptavidin is composed of four essentially identical polypeptide chains and presents a molecular weight over 100 kDa, if coupled with HRP [57]. A dedicated functionalization process for the immobilization of Streptavidin-HRP (Stp-HRP) on gold substrate was followed (see Fig. 2.16).

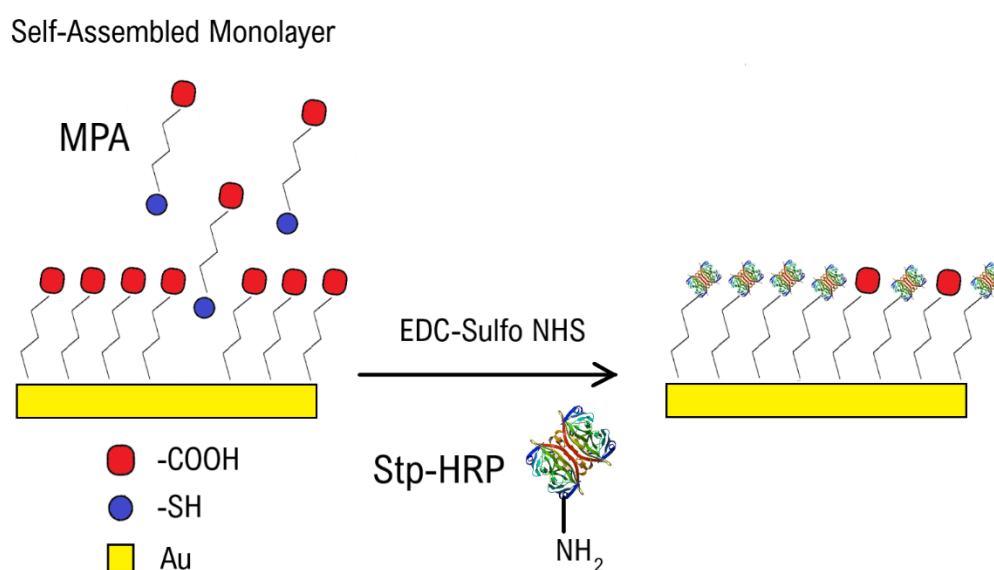
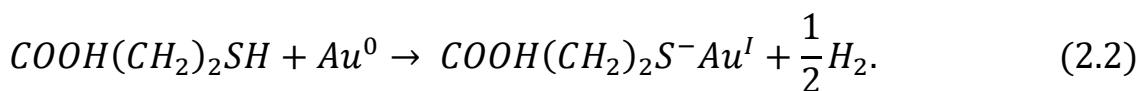


Fig. 2.16 – Schematic picture of Stp-HRP functionalization. (Notice that the real dimensions of the elements are not maintained due to the easier comprehension of the process).

The gold squared gate electrodes were washed in acetone and dried with nitrogen. A Self-Assembled Monolayer (SAM) of thiols was built incubating each gate electrode in a solution of 10 mM 3-mercaptopropionic acid (MPA) in ethanol for an hour at room temperature. Thiols are organic compounds, constituted by a head functional group, a carbon chain and a tail group, and used in this kind of processes as linkers. -SH (thiols), -COOH (carboxylic acids) or silane are examples of head groups, which allow the bonding with specific substrates, such as Au, SiO₂ or Al₂O₃. Once the thiols started the assembly, the carbon chains make the structure more compact and stable, thanks to Van der Waals interactions, whose maximization leads to a bending (about 30°) of the thiols with respect to the substrate. The thickness of the assembled layer depends on the number of

methylene groups within the carbon chain of the involved thiols. The ending functional group, like -COOH, -CHO, -OH, CF₃, can bind other molecules, through subsequent steps. In this case, MPA shows a -SH head and a carboxyl group -COOH at the other extremity, and presents a propyl chain with three carbon atoms. The reaction between thiol and substrate is:



After the incubation, the electrodes were placed in ethanol in order to remove the unbounded thiols and then dried with a nitrogen stream.

At this point, the surface was covered by a thin monolayer of thiols, which exhibit carboxylic groups. Since proteins show an amino group (-NH₂) at one terminal of their amino acid chain, they can theoretically form a chemical bound with a carboxylic group through a condensation. Nevertheless, an activation of -COOH groups is strictly necessary in order to increase the reactivity of these groups to primary amines, like proteins. The mechanism of 1-Ethyl-3-(3-dimethylaminopropyl)-carbodiimide hydrochloride (EDC) and N-hydroxy-sulfo succinimide sodium salt (Sulfo-NHS) is frequently adopted for the activation of carboxylic groups, during bio-functionalizations [58]. The EDC and Sulfo-NHS chemistry generates two consequent reactive esters, starting from the molecule with the -COOH group, facilitating the formation of a stable amide bond with an amine [59]. In this specific case, the thiol and the Stp-HRP respectively correspond to the carboxylate molecule and to the amine, shown in Fig. 2.17.

After the SAM step, the electrodes were placed in a solution of EDC and Sulfo-NHS for 15 min. They were immersed in a solution of phosphate-buffered saline (PBS) for 5 min on a rocking platform shaker, then the PBS solution was replaced. This step was repeated three times, in order to remove possible residues.

The samples were thus incubated with Stp-HRP and placed in fridge at +4°C, overnight.

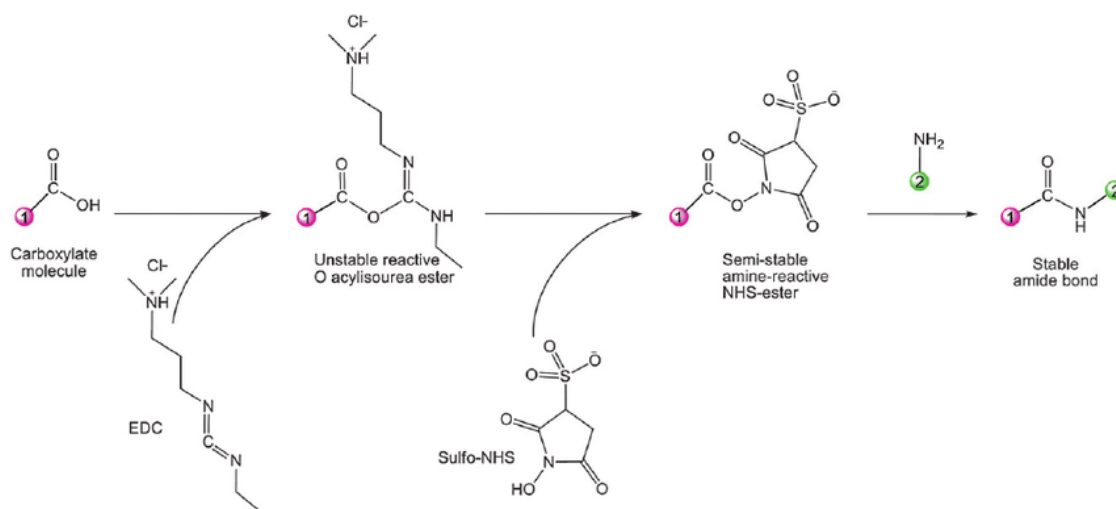


Fig. 2.17 – The mechanism of EDC and Sulfo-NHS for the activation of $-COOH$ groups [59].

At the end of every single step, a sample was collected and then used for the measurements. Therefore, after the functionalization, the following gate electrodes were produced:

- Au with SAM of thiols (SAM);
- Au with activated thiols through EDC and Sulfo-NHS mechanism (*activated SAM*);
- Au with StpHRP after 1 hour of incubation (*StpHRP 1 hour*);
- Au with StpHRP after an overnight incubation (*StpHRP overnight*).

2.3.2 Vascular endothelial growth factor (VEGF)

In this second detection measurements both antibodies and antigens were involved (see Fig. 2.18). As for StpHRP, the SAM step with thiols were repeated. After the activation through EDC and Sulfo-NHS, the samples were incubated with 50 $\mu\text{g}/\text{mL}$ of Protein G, overnight. Protein G is expressed in Group G Streptococcal bacteria and is commonly used also to immobilize antibodies, due to its specific portions, which express a high binding strength to different immunoglobulins. In this case, Protein G allows the formation of the bond between the $-COOH$ extremity of the thiols and the fragment Fc of anti-VEGF, orienting the fragments Fab, which detect the antigen, towards the electrolytic solution. The samples were washed in PBS three times, then they were incubated

with different concentrations of VEGF antibodies for 1 h: 0.5 $\mu\text{g}/\text{mL}$, 1 $\mu\text{g}/\text{mL}$ and 5 $\mu\text{g}/\text{mL}$. After another washing in PBS, all samples were incubated with the same concentration of antigen (100 ng/mL) and then washed.

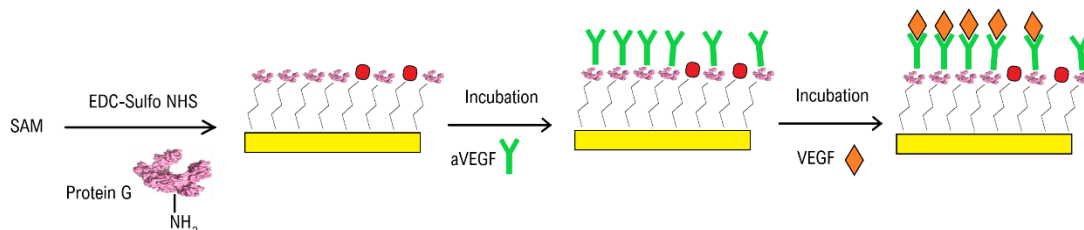


Fig. 2.18 – Functionalization with VEGF antibodies and immobilization of VEGF.

Summarizing, the following gate electrode were produced:

- Au with SAM, Protein G and 0.5 $\mu\text{g}/\text{mL}$ of aVEGF (*aVEGF 0.5 $\mu\text{g}/\text{mL}$*);
- Au with SAM, Protein G and 1 $\mu\text{g}/\text{mL}$ of aVEGF (*aVEGF 1 $\mu\text{g}/\text{mL}$*);
- Au with SAM, Protein G and 5 $\mu\text{g}/\text{mL}$ of aVEGF (*aVEGF 5 $\mu\text{g}/\text{mL}$*);
- *aVEGF 0.5 $\mu\text{g}/\text{mL}$* with 100 ng/mL of VEGF;
- *aVEGF 1 $\mu\text{g}/\text{mL}$* with 100 ng/mL of VEGF;
- *aVEGF 5 $\mu\text{g}/\text{mL}$* with 100 ng/mL of VEGF.

The measurements were conducted involving two different concentrations of PBS, as electrolyte: PBS 0.1x and PBS 1x.

2.4 Device measurement set-up

All measurements were realized with the Source Measure Unit (SMU) Keysight B2912A, driven by the software Keysight Benchvue for the characterization curves and by Quick IV Measurement Software for chronoamperometry. The SMU allows both the generation and the measurement of the electrical variables, using the same connections. The set-up is constituted by two channels, because the source is grounded, and thus the drain and the gate voltage are referred to the source. Channel 1 supplies the voltage between drain and source and can measure the drain-source voltage and the drain-source current. At the same time, channel 2 can apply a gate voltage and it can measure the gate-source voltage

and the gate-source current. A simple representation of the measurement circuit is shown in Fig. 2.19.

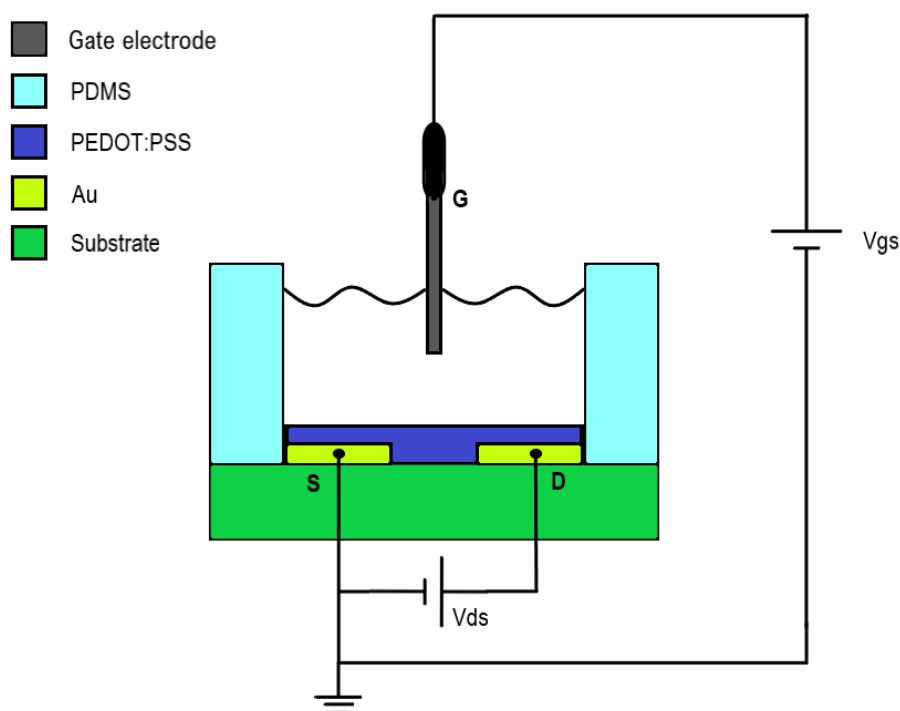


Fig. 2.19 – All measurements were conducted through this configuration: the source was grounded and only two channels are needed for the connection of drain and gate terminals.

2.4.1 Set-up for characterization

In this phase the 120 μL PDMS chamber was used, the Ag/AgCl wire was immersed in a solution of 100 mM NaCl and connected to channel 2. The source and drain terminals were contacted to the measurement system by micro-manipulators (Fig. 2.20).

In order to evaluate the response of the device and then the best working ranges, the different devices were characterised by the transfer and the output curves.

For the first one, a constant negative voltage of -500 mV was applied to channel 1 (so between drain and source), while a voltage sweep from -750 mV to 1 V with a scan rate of 20 mV/s was applied to the other channel (between the gate electrode and the source). Consecutively, a voltage sweep from 1 V to -750 mV was applied in order to observe the hysteresis. During each voltage sweep the two corresponding currents were measured: the drain-source electrode current

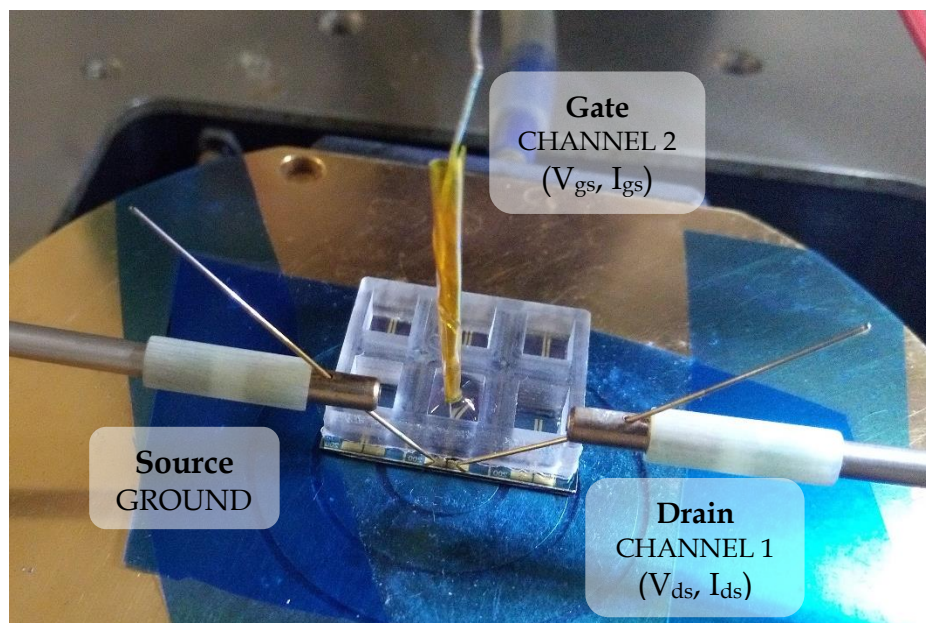


Fig. 2.20 – A real picture of the characterization set-up.

measured by channel 1 and the current between gate and source, measured by channel 2. For each device this curve was repeated three times, allowing a better stabilization of the measurement.

For the output characteristic, a list of different gate voltages (-200 mV, 0 V, 200 mV, 400 mV, 600 mV, 800 mV and 1 V) was used in sequence to obtain several output curves. Every curve was measured applying a voltage sweep from 0 V to -1 V on the drain electrode, with a scan rate of 20 mV/s. The same currents were measured (the drain-source and the gate-source ones).

The application of a negative drain-source voltages is due to the property of the conductive polymer of transporting holes: the negative drain pole attracts the positive charges from the source (ground), generating a current flow. The measured drain-source current, as reported in the next chapter, will be thus negative, because the direction of the current goes from the source to the drain terminal.

The scan rate depends on the time between two consecutive measurements and on the step between two consecutive voltages. OECTs show a response time from almost 100 μ s up to 1 s, therefore a delay between consecutive measurements of

1 s was chosen. Selecting a voltage step of 20 mV, a reasonable trade-off between the voltage resolution and the measurement duration was obtained.

With these settings, the fabricated devices (*H₂SO₄_spin*, *GOPS_spin*, *H₂SO₄_ink* and *GOPS_ink*) were characterised one by one before the functionalization step. Only the two samples without improvements were not characterized, due to their degradation, as it will be shown at the beginning of Chapter 3.

2.4.2 Set-up for the detection

For the first measurements (with Stp-HRP), the functionalized gate electrode was inserted in its slot in the PDMS lid, from below upwards, in order to ensure that the functionalized surface is preserved where the gate electrode will be immersed in the electrolyte. The platform without the cover was filled with the solution, then the chambers were closed by the lid, containing the gate electrode. All electrodes were then contacted by micro-manipulators (Fig. 2.21).

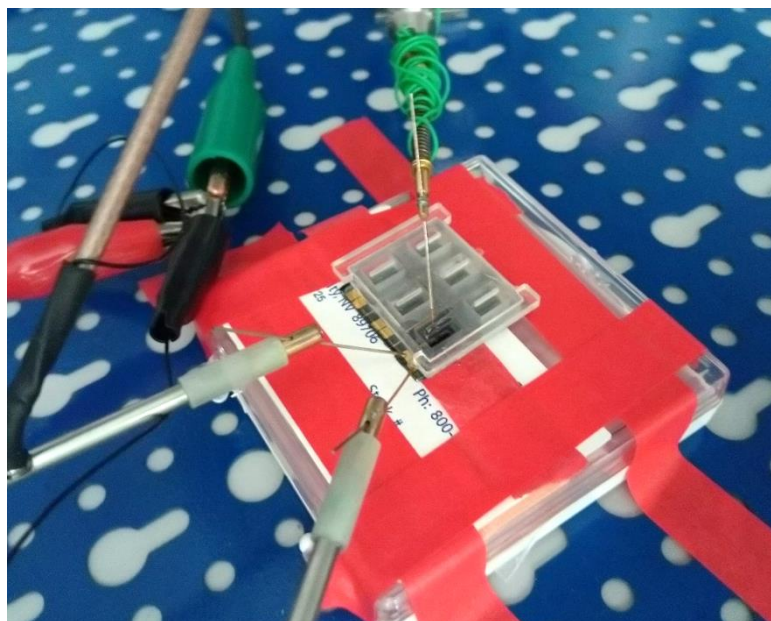


Fig. 2.21 – The SP during the first measurements (the chambers do not allow the change of the solution without the removing of the lid).

For the real-time measurements, the functionalized gate electrode was inserted with the same method in the PDMS lid, the device and the PDMS chamber were placed on the basement of the case, then the rigid cover of the case, supporting the lid with the gate electrode, was firmly sealed with screws. The connections were obtained through the micromanipulators, in the same way as seen in Fig. 2.18: the external case allows the connection of the drain electrode, on one side, and of the source, on the other side (Fig. 2.22), while the electrolytic chamber was filled by an automatic pump system (Fig. 2.23).

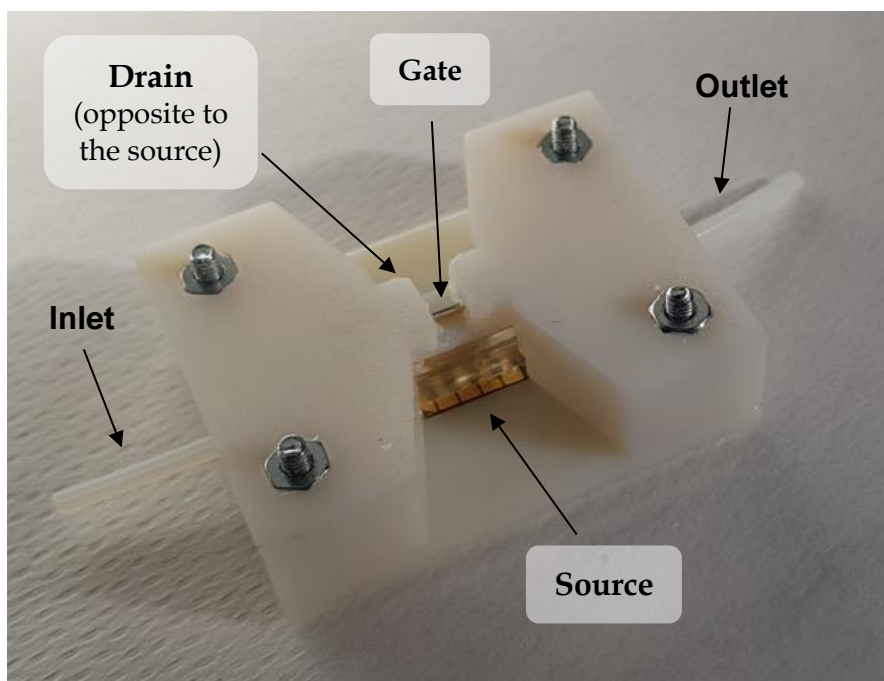


Fig. 2.22 - The connections of the RTP to the electronic set-up and to the microfluidic system.

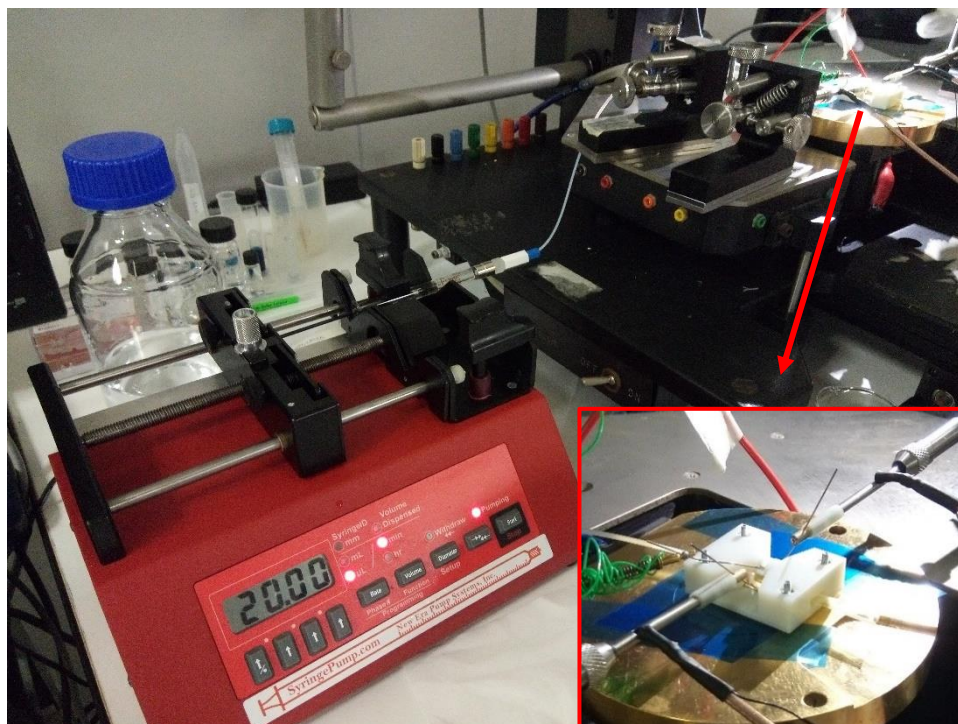


Fig. 2.23 – The whole real-time set-up: the pump system is seen on the left of the main picture, while on the right it is reported a zoom of the connected RTP.

3.

Ink-jet printing optimization

In the following sections the whole process of ink-jet printing optimization is reported, from a brief description of the ink-jet system to the last settings for the print of the digital pattern. The description is correlated to the experimental pictures, collected during the testing. More details regarding the ink-jet printer used in this work are included in the Appendix.

Regarding the environment of Chilab, the following work represented the first successful attempt to develop an ink-jet printing optimization process. Furthermore, the deposition of PEDOT:PSS on silicon oxide by ink-jet printing represented a novel process, since other research projects focused on the deposition on other materials (like glass or flexible substrates) or through different techniques. In order to compare this deposition technique with the more common spin-coating one, the polymeric solutions (Clevios and Clevios+GOPs), the same pattern and the same geometric characteristics of the final pattern have been used as reference and goal also in the printing technique.

3.1 Jetlab 4 ink-jet system

The Jetlab 4 DOD ink-jet system is equipped with a single-nozzle print-head, moving above a horizontal platform, for a 30 cm x 30 cm printing area (the grey square plate in Fig. 3.1). The diameter of the nozzle orifice is 50 μm and is provided with the electrical connections for the application of the voltage pulses to the tube-type piezoelectric material [60] (Fig. 3.2).

The printer is driven by a specific software (*jetlab4.exe*), provided by the manufacturer. Inside the main window of this driving software, the main settings can be set and the script, containing the additional instructions to print the pattern, can be loaded (for details about the script, see the Appendix).

In this chapter the optimization process, that led to the individuation of all the parameters needed to print homogeneous and water-stable films of PEDOT:PSS on a substrate of silicon oxide, is described. This process started from the regulation and stabilization of the drop jetting through the optimization of the main settings, and continued with the research of optimal additional settings, regarding specific options for the print.

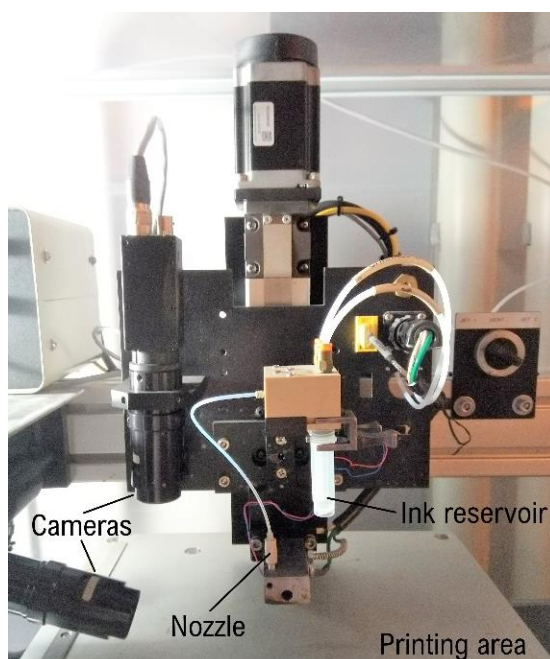


Fig. 3.1 –The main components of the Jetlab printing block.

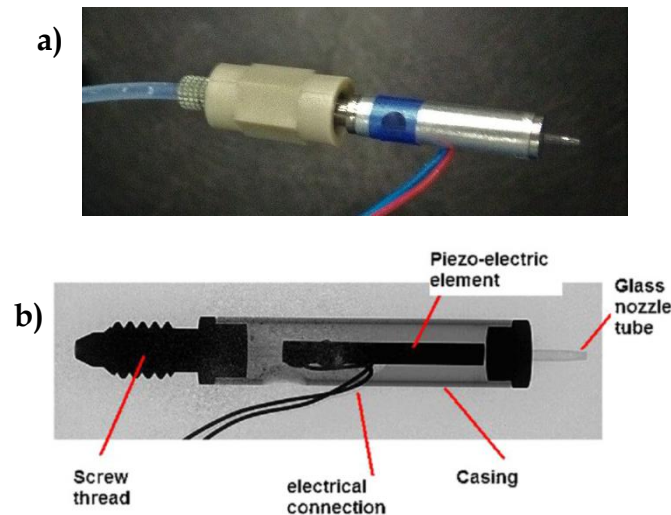


Fig. 3.2 – The 50- μm -diameter glass nozzle with the connection to the fluidic system (a) and its internal structure (b), shown through X-rays [60].

3.2 The problem of clogging

The first problem, observed during the drop jetting, was the clogging or the deposition of filaments at the end of the nozzle.

With the first tests using un-treated *Clevios* solution, this phenomenon often occurred and the regulation process of the jetting was suspended every time. A cleaning procedure of the nozzle and of the fluidic system was necessary, in order to continue the droplet ejection. The cleaning operations are conducted manually, removing the nozzle from the printing system and using a syringe, an adaptor to connect the syringe to the nozzle and some beakers (for the water and for the waste). They consist in flushing and subsequently back-flushing DI water through the nozzle, until the water flows out easily upon the application of a low pressure on the fluid. The successful cleaning of the glass orifice is visible at an optic microscope.

It was observed that *Clevios* shows thin filaments, which stop at the end of the nozzle, blocking the regular flux of ink, in most of the cases. For this reason, the solution was firstly treated, testing different techniques:

- filtering the solution with a pore size of 0.45 μm twice;

- immersing a small falcon, containing the ink, in ultrasonic bath for 15 min, then filtering;
- sonicating the solution for a total on-time of 20 min, then filtering.

The last procedure allowed the complete removing of the filaments and was applied to both *Clevios* and *Clevios+GOPS* solutions. In fact, the sonication allows a better dispersion of the polymeric molecules within their aqueous solution, through the phenomenon of cavitation, which consists in the generation of microbubbles, due to the application of ultrasounds. The sonifier has a probe, which must be immersed in the solution and which propagates the ultrasonic mechanical vibrations to the solution. When the wave meets the liquid, high and low pressure zones are formed and, if the ultrasound is intense enough, bubble-shaped cavities are generated between those regions. The volume of these bubbles increases, until their explosion. This causes a local increase of both temperature and pressure and may generate jets with a high speed (up to about 280 m/s), in fact the sonifier is often used also for homogenization and emulsion. With polymers, the ultrasonic waves may enhance the dispersion of the polymeric particles in the liquid medium, reducing the viscosity. For the high intensities and the direct diffusion of the vibrations thanks to the immersed probe, this system is more efficient for this purpose than the ultrasonic bath.

3.3 The main settings

The printing optimization firstly focused on the fundamental parameters, that control the formation, the dimension and the stability of the ejected drops: the back-pressure and the driving waveform (and the corresponding voltage, time values and frequency). The jetting is observed by a lateral camera, as in Fig. 3.3.

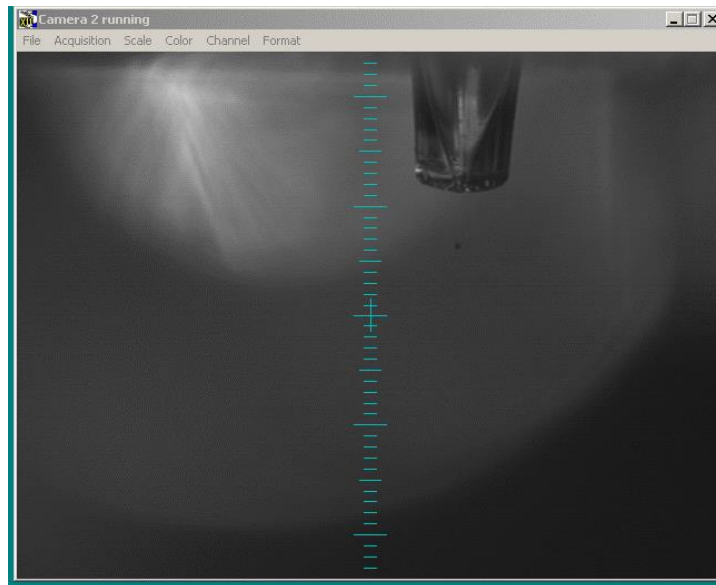


Fig. 3.3 – A stable drop jetting, without satellites and with a good direction of ejection (perpendicular to the printing area). The picture is obtained by the stroboscopic lateral camera of the printer.

3.3.1 The back-pressure

The printing system is provided with a pressure pump, that holds the ink reservoir under pressure (in the manual provided by Microfab it is called back-pressure). The set value of this back-pressure is displayed in psi (pound per square inch³) in the front panel and manually adjustable. A positive back-

³ 1 psi = 6.805×10^{-2} atm = 6.895 kPa

pressure is related to a force that pushes the surface of the ink, leading it to the nozzle through a fluidic channel. In this condition, after the air removal, huge

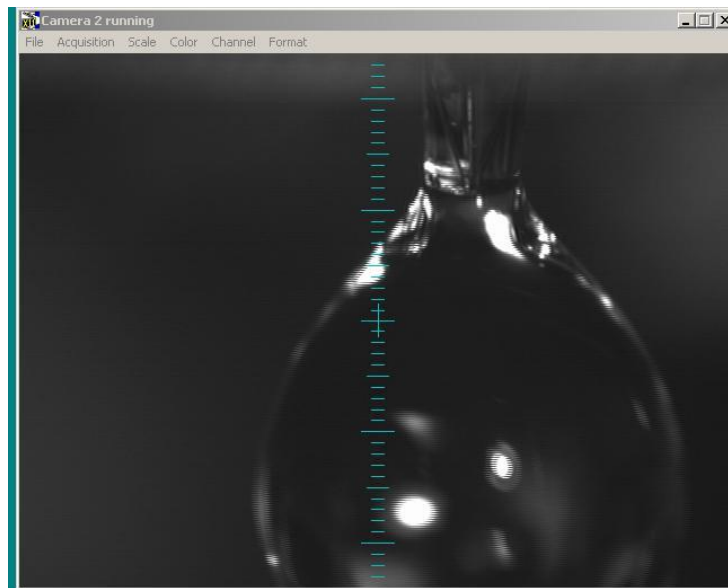


Fig. 3.4 – The big drops flow from the nozzle under a positive back-pressure (observed through the lateral camera).

drops (as in Fig. 3.4) flow from the nozzle, indicating that the fluidic channel is completely full of ink.

In order to avoid a spontaneous dropping out of the orifice during the jetting and then during the printing process, the ink reservoir must be held under a negative back-pressure (toward the pressure pump, see Fig. 3.5). Keeping the ink solution inside the reservoir, the application of a negative back-pressure is also more effective in order to avoid the dropping of a too high volume of ink, generating several drops without a controlled direction. Furthermore, the negative back-pressure allows a better definition of the optimal pulse width, and therefore leads to a better definition of the time ranges for the generation of the smallest drops [61]. Inks with higher viscosities require higher back-pressures, in order to avoid leakages of the ink from the orifice due to their higher weight.

The optimal range for the back-pressure includes the pressure values at which the ink forms a meniscus at the extremity of the nozzle.

For *Clevios* and *Clevios+GOPS* the optimal back-pressure is between -6 psi and -8 psi, depending on room conditions, and the specific value can be manually

selected and also adjusted during the jetting optimization. At higher values of pressure (up to -2 psi), the ink flows from the nozzle under the effect of its own weight, slowly generating huge drops. Instead, more negative values (such as

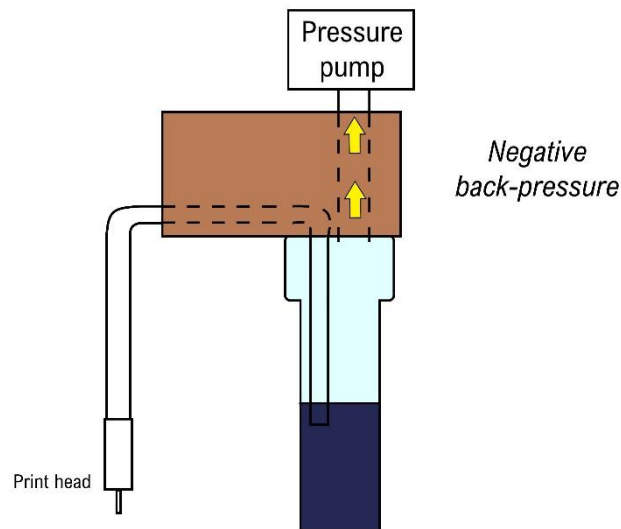


Fig. 3.5 – Schematic representation of the application of a negative back-pressure on the ink reservoir.

lower than -12 psi) of this parameter completely hold the ink in the reservoir, preventing any drop jetting.

3.3.2 The driving waveforms

Among all parameters that can be set within the printing driver, the voltage waveform for the piezoelectric element is fundamental for the regulation and the stability of the jetting and, thus, for the quality and the dimension of the ejected droplets.

The simplest voltage waveform which can generate droplets is the unipolar waveform, an on-off pulse (Fig. 3.6). This latter moves the piezoelectric transducer and then returns it to the rest state. All parameters of the drive waveform can be manually set, from the values of voltage to all the corresponding times (rise time, dwell time and fall time) of the waveform. An increase of the voltage results in an expansion of the fluid, on the contrary a voltage drop causes a fluid compression. While the voltage remains constant, the pressure wave can propagate within the fluid.

The pulse width (mainly referred to the dwell time) and the pulse amplitude can be regulated, optimizing the jetting effectiveness. Firstly, the dwell time range, where the nozzle can eject single and stable droplets of the selected ink, is identified. Due to the acoustic oscillations that are generated by compressions, it was proved the existence of an optimal value within the pulse width range, which is defined as the highest drop volume at a given pulse amplitude [62] (Fig. 3.7a). Regarding the pulse amplitude, it is verified that the increase of the drop volume is proportional to the increment of the voltage amplitude [60] (Fig. 3.7b).

In order to print microelectronic devices, the parameters of pulse width and amplitude must be the ones that allow the lowest volume of the droplets, due to the improvement of the printing resolution. For example, the best values to obtain the smallest PEDOT drops for the unipolar wave are 30 V and 25 μs [60]. But this waveform shows considerable drawbacks: the volume of the drops is still too big for this application and some satellites can be found next to the printed pattern. The satellites are undesired droplets caused by different

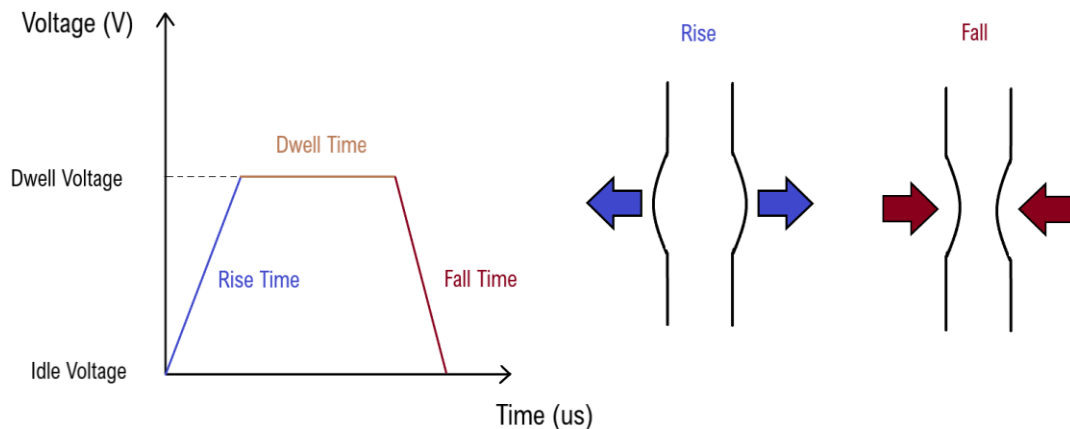


Fig. 3.6 - The unipolar waveform with the description of the effects on the piezoelectric material. During rise time the fluid is expanding, while in fall time there is the fluid compression. The dwell time represents the delay for pressure wave propagation.

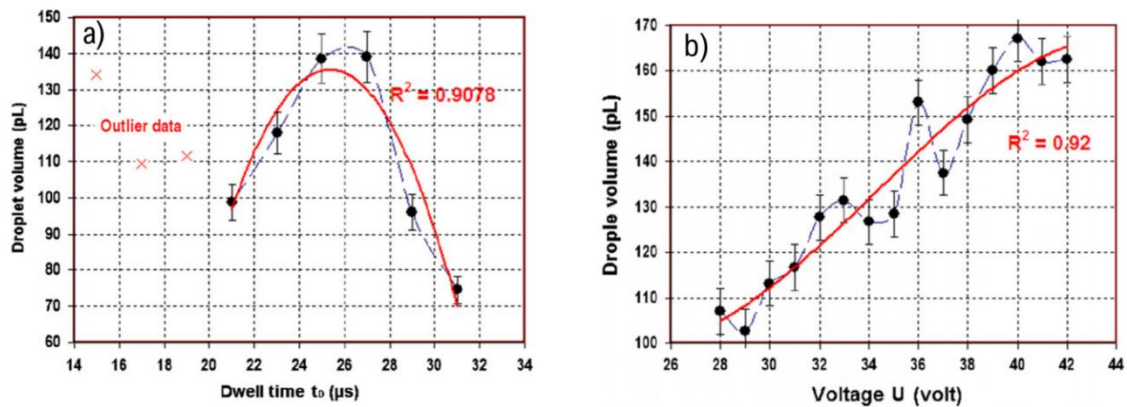


Fig. 3.7 – Effects of the dwell time (a) and of the voltage amplitudes (b) on the droplet volume in a piezoelectric DOD printing system. The curves refers to a unipolar wave, applied to PEDOT (from Sigma Aldrich) [60].

phenomena, occurring during the printing process, due to a combination of the dispensed solution and the driving waveform. A typical phenomenon, which may occur during the waveform application in low viscosity fluids, is that the pressure waves still travel in the nozzle after the ejection of the main drop. If those waves have enough residual energy, they may form satellites. For these reasons, a bipolar waveform is used to produce the main drop and to eliminate the residual acoustic waves propagating in the tube. It is composed by an initial trapezoidal curve, like the unipolar, and by a second negative part, called echo pulse. The function of the initial portion remains the same. The echo pulse can be used to eliminate some of the residual acoustic oscillations that remain in the device after drop ejection. In order to find the best waveform, the research of the best amplitude and dwell time is necessary. Typically, the optimum bipolar waveform has the same positive and negative voltage and the second dwell time is twice the initial one [61], but this proportion may slightly change during the optimization process.

Another fundamental parameter related to the waveform is the frequency, which can also overcome thousands of Hertz and cause an increase of drop-ejecting velocity. The choice of the frequency is likewise dependent on the ink.

It is important to consider that the waveform (the pulse width, the amplitude and the frequency) and the setting of the back-pressure are strictly ink-dependent,

due to the different characteristics of the employed solutions. The bipolar wave, shown in Fig. 3.8, was used for DI water and may generate drops of 88 μm up to 97 μm on a water-sensitive paper (Fig. 3.9).

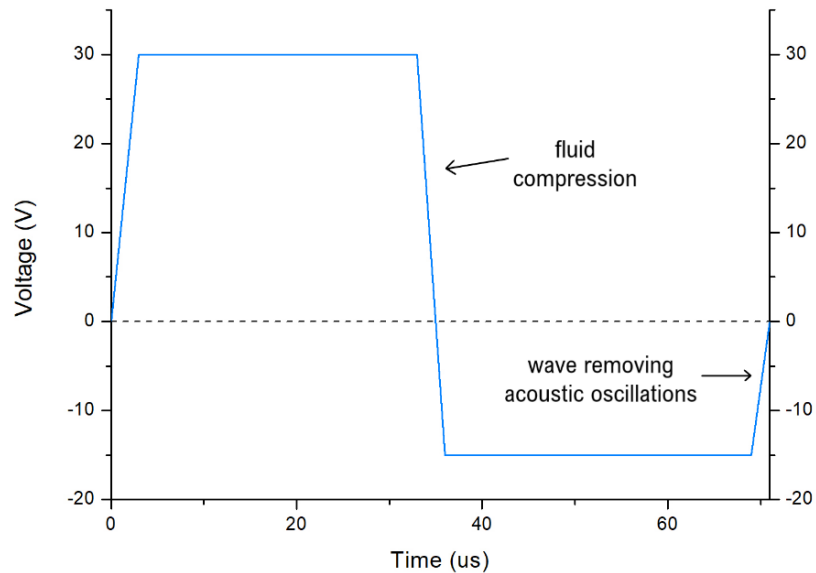


Fig. 3.8 – Bipolar wave used for DI water at 380 Hz with back-pressure of -6 psi.

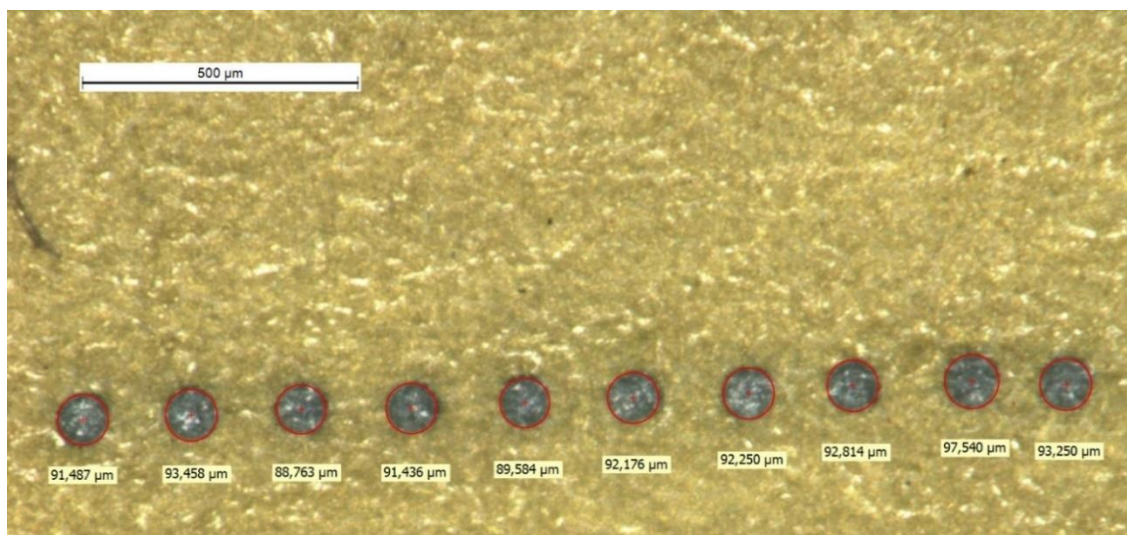


Fig. 3.9 – Droplets obtained with DI water upon the application of the bipolar wave, reported in the previous figure.

The dwell time, which allow the production of stable and single drops, may vary between 30 and 55 μs , depending on room conditions. Filtered DI water (with a 0.45 μm -pore-size filter) was used for preliminary tests and cleaning cycles.

Since a specific ink-jet printing protocol for *Clevios* and *Clevios+GOPS* has not been developed yet, a dedicated optimization of the driving waveforms was strictly necessary.

Both *Clevios* and *Clevios+GOPS* are more viscous than DI water, so they need a higher driving voltage [54], and a different waveform.

Different kinds of waveform were tested, in order to obtain the smallest drop diameter on a silicon oxide substrate.

Firstly, the bipolar wave used for DI water was employed with the solutions containing *Clevios*: droplets, with an average diameter around 207 μm , were produced, as reported in Fig 3.10, but in most of the cases satellites and unstable droplets were also generated.



Fig. 3.10 – Droplets of *Clevios* on a silicon oxide substrate, generated by the same bipolar wave used for DI water.

Secondly, a more complex waveform was tested: the W-wave [60], so called for its shape (or negative Purdue waveform [63]). It is constituted by a bipolar wave, preceded by a negative unipolar wave. Both negative parts of the W-wave need to remove any residual acoustic waves: the first negative part removes the oscillations from the last cycle of ejection and the second negative one from the current drop generation. This waveform was applied for a PEDOT ink (from Sigma Aldrich) by Gan et al. [60], and allowed the production of the smallest ejected droplets. They reported the parameters of the best W-wave (see Tab. 3.1

and Fig. 3.11), guaranteeing the reduction of the drop dimensions to 60 μm on a silicon substrate.

	V_1	V_2	V_3	t_{fall_1}	t_{dwell_1}	t_{rise_1}	t_{dwell_2}	t_{fall_2}	t_{dwell_3}
PEDOT	-20 V	65 V	-50 V	1.0 μs	2.0 μs	0.2 μs	3.0 μs	0.5 μs	1.0 μs

Tab. 3.1 – The W-waveform parameters for PEDOT ink [60]

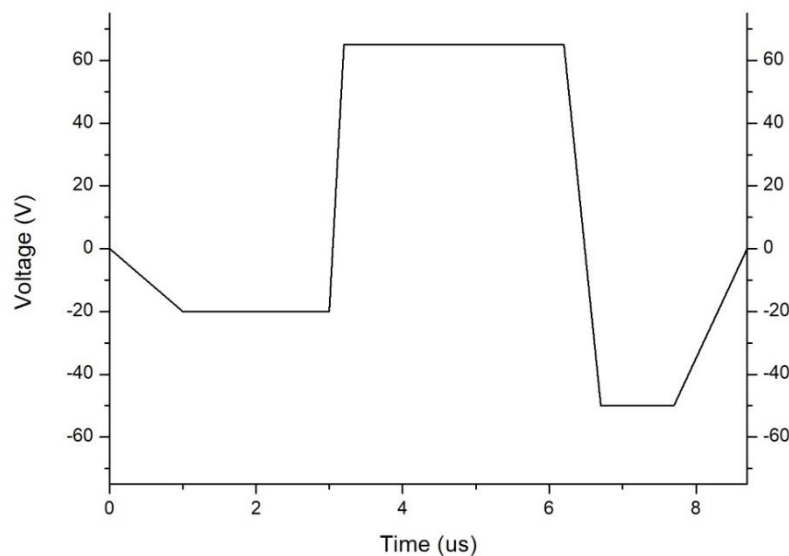


Fig. 3.11 – The graphical representation of the W-waveform for PEDOT.

Due to the different ink solution (PEDOT instead of *Clevios*) and to a slightly different printing system (Microfab Jetlab II), that W-wave has been changed as follow:

- **Printer limitation:** Each fall and rise time had to be increased, due to the limitation of this printer (fall and rise time must be bigger than 2 μs for a voltage difference that is bigger than 30 V, in absolute value, and this minimum time must be increased of 1 μs for every increment of 30 V in voltage. For example, for a difference of 60 V, the fall and rise time must be almost 3 μs . Further, decimal values, smaller than 0.5, are not permitted). The values reported by Gan et al. were thus necessarily increased.
- **Frequency:** The frequency of 550 Hz, used by Gan et al., still allowed the drop formation with *Clevios* and *Clevios+GOPS*. At a lower frequency, as the one

used for DI water, and with this kind of wave, the drops were not produced. The W-wave at 550 Hz had to be further adapted in order to solve other problems, such as instability of the drops and frequent jetting interruptions.

- **Removing satellites:** It was observed that the difficulty in the drop formation was due to the third part of this waveform, which caused even interruptions in drop jetting. In fact, the drops could still be formed without that wave part, but creating satellites, at the same time, and reducing slightly the final droplet diameter (see Fig. 3.12), respect to the bipolar wave. The satellites can

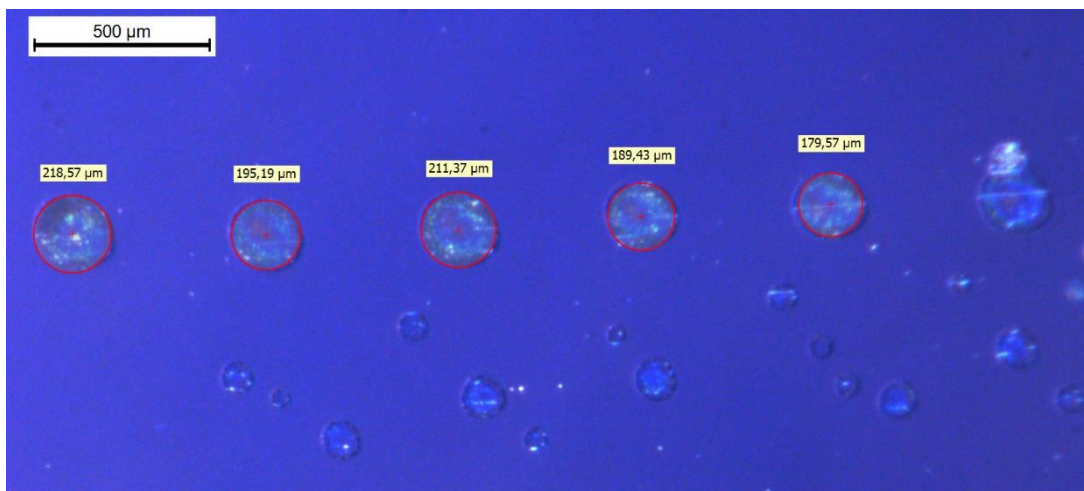


Fig. 3.12 – The Clevios droplets, produced by a reduced W-wave, achieved an average diameter of ca. 155 μm, showing the phenomenon of the satellites.

represent a great problem, during the printing, because they can modify the final print, as seen in Fig. 3.13. For this reason, the third negative part was necessary, but some values had to be modified.

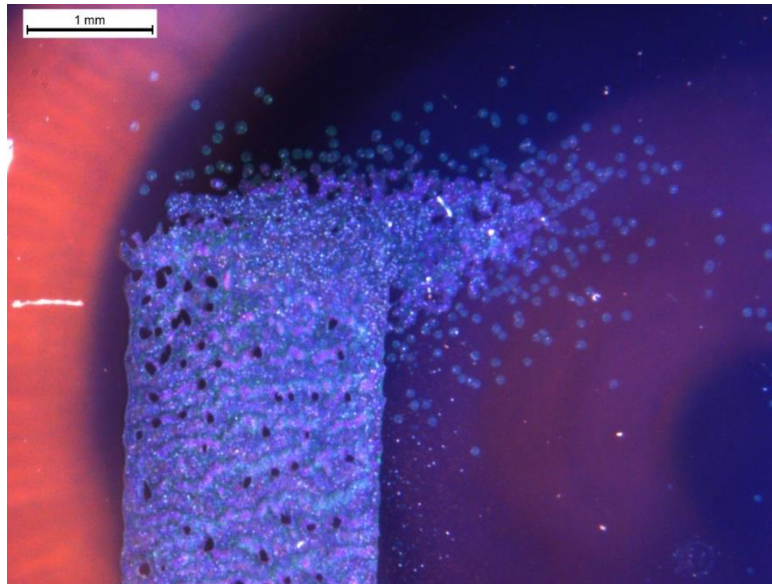


Fig. 3.13 – The effect of the satellites in a printed pattern.

- **Final modification:** The dwell time was increased, in order to obtain again the drop formation. For a better stability of the drops, the potential difference of this part of the wave (from 65 V to -50 V, in the original W-wave) was reduced, obtaining a voltage drop from 65 V to -40 V and the drops, shown in Fig. 3.14⁴.

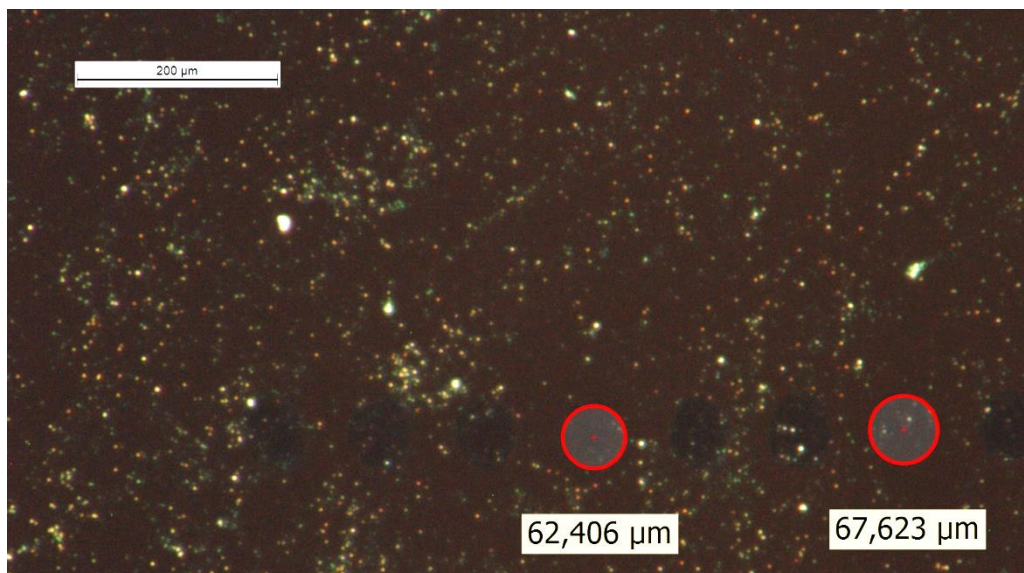


Fig. 3.14 – The drops ejected through the optimized W-wave for Clevios.

⁴ The different colors of the substrate in the pictures do not indicate a different material, but it is only an artefact, due to the effect of the microscope's light on the silicon substrate, which is very reflective.

For the *Clevios+GOPS* solution, the same wave used for *Clevios* was not effective, so it has been tried to preserve the same shape of the driving wave. The time values were maintained, but the voltage values were changed. Initially, the voltage of the third part of the W-wave was reduced to -40 V, in order to remove satellites, but it was not successful. Using a more negative voltage (-50 V), the satellites were removed, but the drops were still too large (about 200 μm): the positive voltage of the wave (65 V) might eject a high volume of ink, destabilizing the jetting and sometimes creating satellites. It was proved that a smaller voltage value for the positive part of the wave was enough for the generation of a smaller drop. The third part of the W-wave originated again the same problems and the only way to eliminate satellites and guarantee a stable droplet formation was to apply a negative voltage of -50 V with an intermediate step of -25 V. The smallest drops with an average diameter of about 109 μm , obtained upon the application of the final wave, are reported in Fig. 3.15.

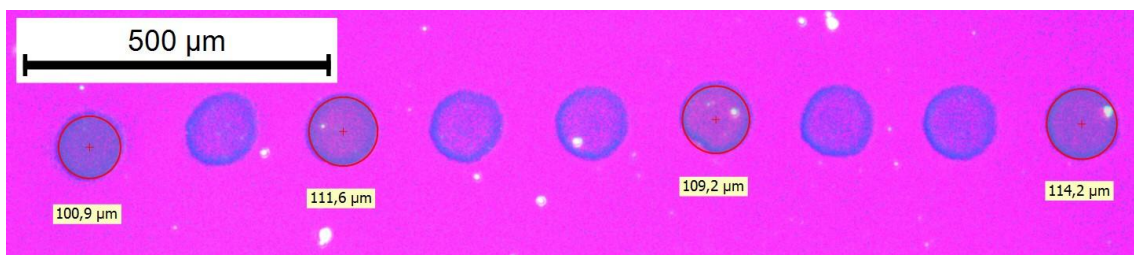


Fig. 3.15 - The *Clevios+GOPS* droplets generated by the corresponding optimized W-wave.

Summarizing, this optimization has led to the determination of two slightly different W-waves for *Clevios* and *Clevios+GOPS*, that ensure a good stability of the drops, the absence of satellites and a good continuity of the jetting (up to about 20 minutes of continuous jetting). The voltage and time values are summarized below in Tab. 3.2 and the corresponding waveforms are shown in Fig. 3.16.

Both the polymeric solution required a higher frequency of the driving waveform and smaller dwell time than DI water, but *Clevios* needed the highest voltage and back-pressure, due to its highest viscosity among the other solutions. Since *Clevios+GOPS* has an intermediate viscosity between water and *Clevios* ones, its

corresponding settings resulted in a lower maximum voltage and pressure than *Clevios*, but a higher voltage and frequency than DI water (all these considerations are resumed in Table 3.3). The back-pressure values were manually adjusted during the testing of the W-waves.

	V ₁	V ₂	V ₃	t _{fall_1}	t _{dwell_1}	t _{rise_1}	t _{dwell_2}	t _{fall_2}	t _{dwell_3}
<i>Clevios</i>	-20	65	-40 V	2.0	2.0	3.0	3.0	4.0	2.0 μ s
<i>Clevios</i> + <i>GOPS</i>	-20	45	-50 V	2.0	2.0	3.0	3.0	4.0	2.0 μ s

Tab. 3.2 – W-wave parameters for *Clevios* and *Clevios+GOPS*.

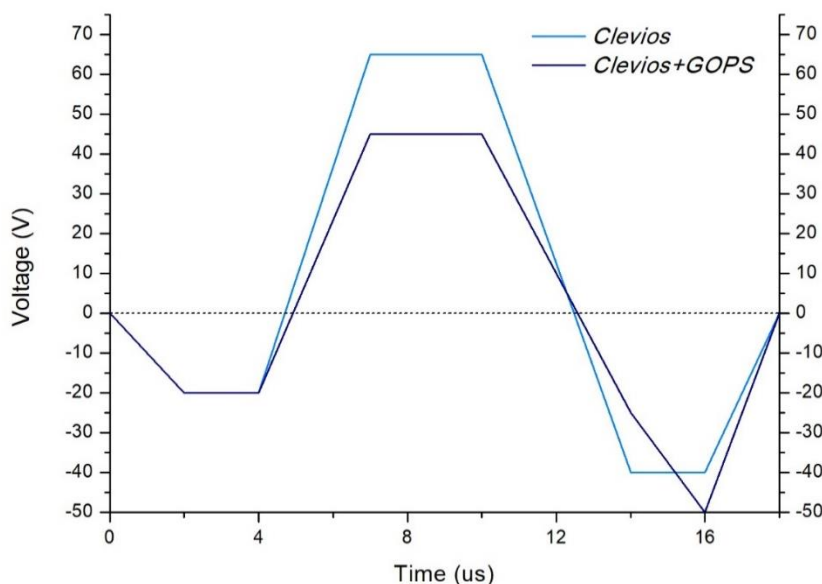


Fig. 3.16 – Optimized W-waves for *Clevios* and *Clevios-GOPS*.

	DI Water	<i>Clevios+GOPS</i>	<i>Clevios</i>
Waveform	Bipolar	W-wave	W-wave
Maximum positive voltage	30 V	45 V	65 V
Dwell time	30 ÷ 55 μ s	3 μ s	3 μ s
Frequency	380 Hz	550 Hz	550 Hz
Back Pressure	-6 psi	-6 psi	-8 psi

Tab. 3.3 – Summary of the settings for the different ink solutions.

3.4 The additional settings

Once the jetting parameters were found, the printing software (*jetlab4.exe*) needs additional parameters, regarding specific printing settings. This fact is due to the ability of this printer system to allow the direct uploading of the digital model of the required pattern. The model is converted into a text file, containing the instructions for the printing process, thanks to the software *GDS2Jetlab.exe*. As reported in the Appendix, the spacing between each drop, the distance from the margins and the moving speed of the print-head must be set within the text file, before launching the printing.

Since the diameter of the ejected drops is around 65 μm , an initial spot spacing of 50 μm was chosen and the default value of 25 mm/s was set for the flow velocity. These parameters were reduced gradually and changed until a uniform layer of *Clevios* was obtained. Table 3.4 shows the first tests, in which the same pattern was printed and was observed at the optical microscope, reporting the printing time and a qualitative feedback.

Test	Spot spacing (μm)	Flow velocity (mm/s)	Time (s)	Feedback
#1	50	25	103	Completely separated drops
#2	25	25	207	Non-uniform
#3	15	25	321	Non-uniform
#4	10	25	-	ERROR
#5	15	15	366	Non-uniform
#6	25	10	280	Non-uniform
#7	20	5	597	Separated drops
#8	15	5	796	Non-uniform
#9	10	5	1187	Uniform

Tab. 3.4 – The tests for the choice of the additional parameters for *Clevios* ink.

The film, obtained in this last way, was analysed with the profiler. The thickness was between 1.2 μm and 1.4 μm , thus was not suitable for OECT devices and not comparable with spin-coated films. In Fig. 3.17 this printed film is shown and the excessive polymeric material is clearly visible on the gold electrodes. After the

H₂SO₄ treatment and after the annealing process (involving different time of baking, from 15 min to about 2 hours), these thick films did not resist, if covered by water: the polymeric printing peeled away from the substrate completely, after only 5 min.

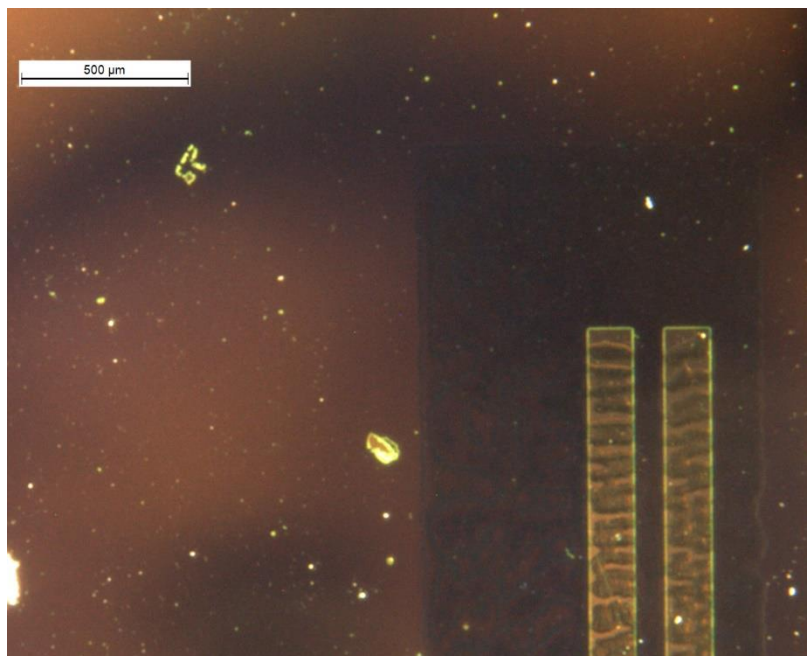


Fig. 3.17 – The Clevios film printed on a sample with the gold electrodes, using the additional settings of test #9.

For in-liquid sensing application, this phenomenon is unacceptable, thus a better adhesion of the film was studied, attempting a better surface preparation (see the next section).

Regarding the *Clevios*+*GOPS* solution, after the deposition of the *GOPS* adhesion layer, the last three tests (#7-9) were firstly investigated. They generated only thick films, therefore the spot spacing was gradually increased and the flow velocity was slightly reduced, allowing a better spreading of the droplets on the substrate, without increasing significantly the printing time (see Tab. 3.5).

With these additional settings, a film thickness between 75 μm and 95 μm can be obtained (see Fig. 3.18). This result shows that the *GOPS* adhesion layer is satisfactory and no additional surface preparation is needed, before the printing.

Test	Spot spacing (μm)	Flow velocity (mm/s)	Time (s)	Feedback
#10	25	4	585	Uniform, thick film
#11	30	4	402	Uniform, thick film
#12	40	4	362	Uniform, thick film
#13	50	4	299	Uniform, thin film

Tab. 3.5 – The optimization of the additional parameters for Clevios+GOPS.

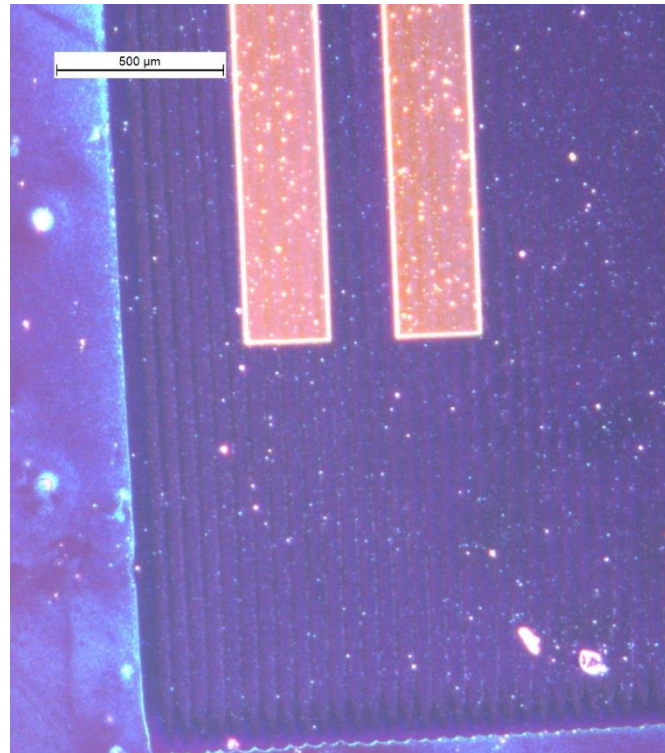


Fig. 3.18 – The Clevios+GOPS thin film, obtained with the settings of test #13.

3.5 Surface preparation

To improve the adhesion and the spreading of the printed drops, the substrate was subjected to a better cleaning. The surfaces of silicon oxide were subsequently cleaned with the following treatments:

- ultrasonic bath in IPA (15 min);
- oxygen plasma (2 min).

After the cleaning procedure, other tests were conducted, starting from the last setting (test #9). The flow velocity was reduced, as for *Clevios+GOPS*. The spot spacing was increased, obtaining a lower overlap and trying to reduce the final thickness of the film, without modifying the homogeneity. In fact, a uniform layer of *Clevios* was printed with a spot distance of 25 μm , instead of 10 μm .

Test	Spot spacing (μm)	Flow velocity (mm/s)	Time (s)	Feedback
#14	10	5	1187	Non-uniform
#15	20	5	597	Quite uniform
#16	25	4	585	Uniform
#17	30	4	402	Non-uniform
#18	40	4	362	Non-uniform
#19	45	4	328	Separated drops
#20	50	4	299	Separated drops

Tab. 3.6 – The test for the individuation of the optimal setting for *Clevios* solution, after the cleaning procedure of the substrate.

An example of the effect of the better cleaning of the substrate is clearly shown in Fig. 3.19, where the same settings were applied, printing on a pristine substrate and on a cleaner surface.

With the best settings (as in test #16), the printed layer achieved a thickness between 185 μm and 200 μm . After the sulfuric acid treatment, the polymer still adhered on the substrate (Fig. 3.20), even if covered and immersed in water, and it was damaged after longer water expositions (from 15 min onwards).

The additional settings used for the printing of the polymeric film are summarized in Tab. 3.7.

In conclusion, the spot spacing is strictly dependent on the diameter of the droplets. The printing process leads to the deposition of several separated droplets on the substrate, instead of the generation of a thin continuous film, for a too large spot spacing (Fig. 3.21a,b). On the other hand, a too small spacing causes the instantaneous merging of several consecutive drops and of adjacent drop lines, leading to the generation of an undesired excessively thick film, due to the failed drying of the solution during the printing process (Fig 3.21c).

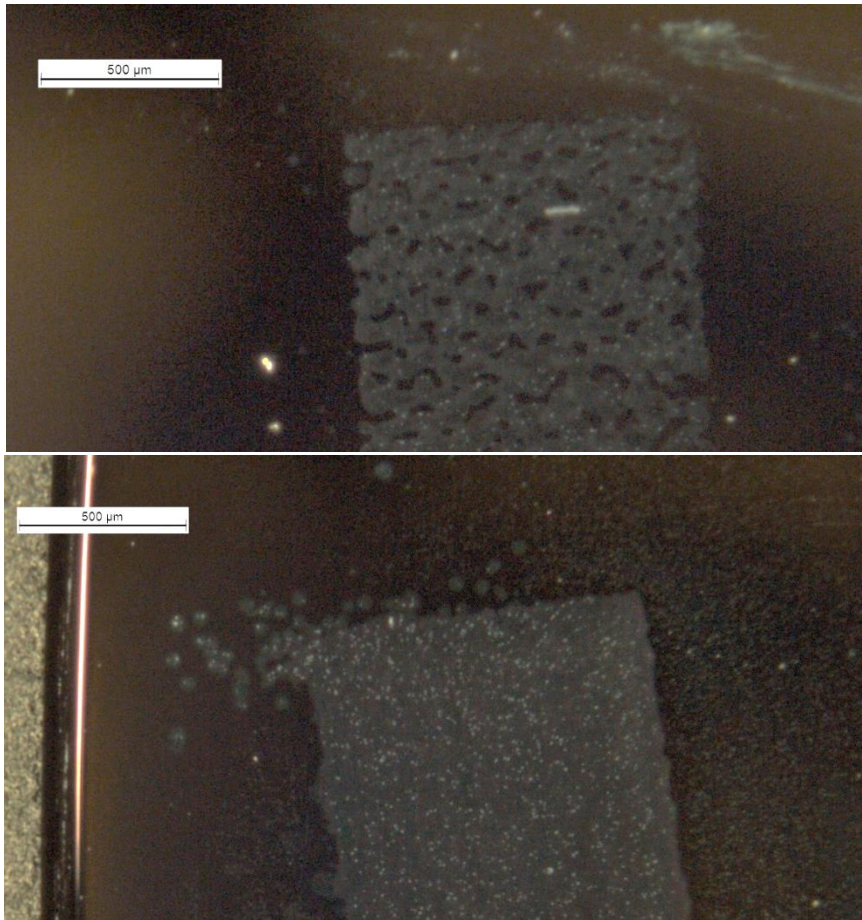


Fig. 3.19 – The same pattern printed with the same additional parameters on a silicon surface without any surface treatment (a) and with oxygen plasma treatment (b).

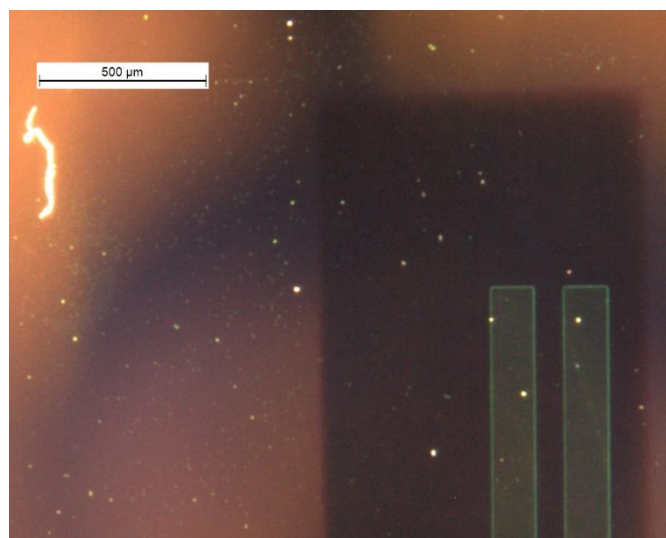


Fig. 3.20 – After the sulfuric acid bath, the printed film was immersed in water for 5 min. The edges slightly thinned.

Additional settings	<i>Clevios</i>	<i>Clevios+GOPS</i>
Spot margin (μm)	25	25
Spot spacing (μm)	25	50
Flow velocity (mm/s)	4	4
Mean diameter (μm)	65	109
Overlap (%)	38.46	45.87

Tab. 3.7 – Additional parameters required for the printing from the digital model.

Concerning the flow velocity, the range between 4 and 5 mm/s guarantees the printing of homogeneous pattern [64]. For both *Clevios* and *Clevios+GOPS* a flow velocity of 4 mm/s was selected. This allowed a good trade-off between pattern homogeneity and printing speed. In fact, too high flow speeds lead to the

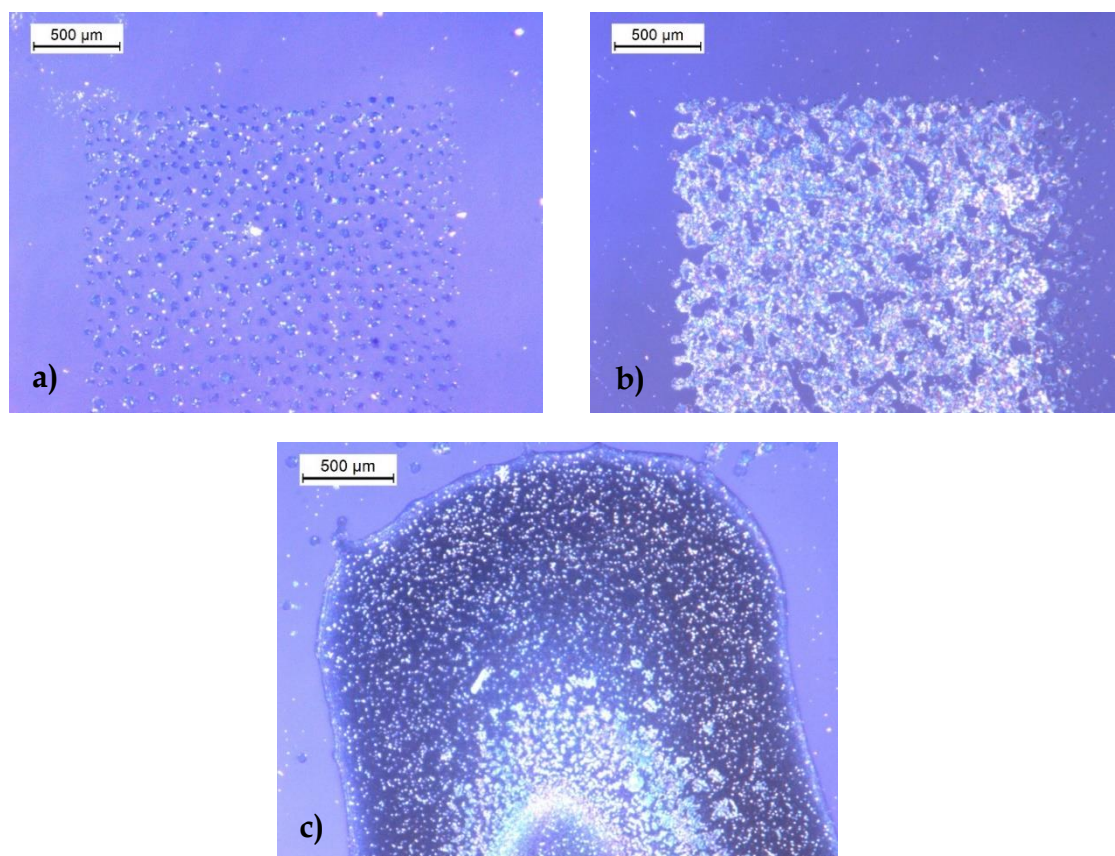


Fig. 3.21– Examples of wrong settings of the spot spacing during preliminary testing of *Clevios* on silicon oxide: (the two above) the use of too large spacing, so the formation of separated drops or holes and (the one below) too small spacing, causing a thick drop with curved boundaries. (Pictures obtained by optical microscope).

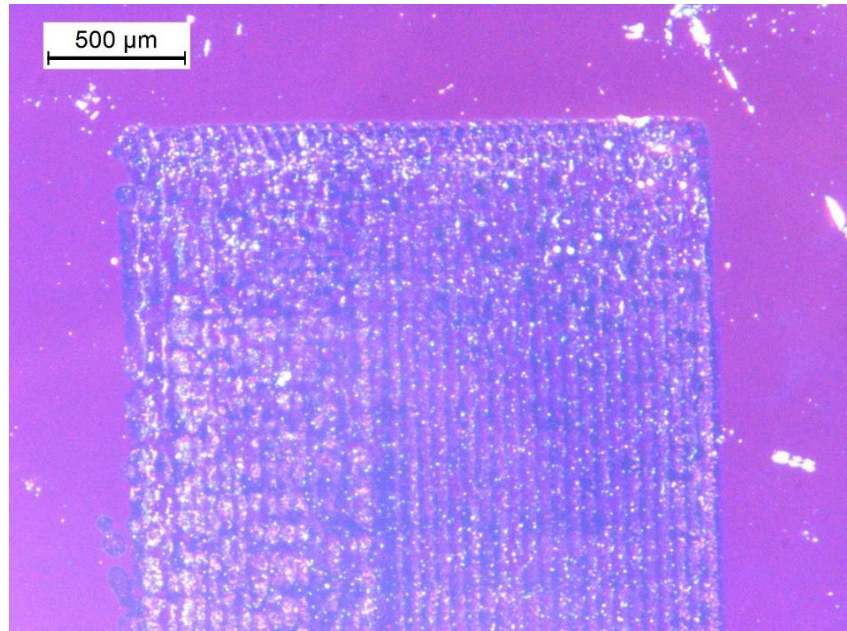


Fig. 3.22 – Good setting of spot spacing during tests of Clevios+GOPS on silicon oxide. (Picture obtained by optical microscope).

merging of consecutive lines of droplets, similarly to the choice of a small drop spacing. For a low flow velocity (significantly below 4 mm/s), the time for the printing increases, so the process might be too long, and the jetting might be no more stable.

4.

Results and discussion

In this chapter the results of the fabrication process are firstly shown, focusing the attention on the SP and on the prominent differences between the two deposition techniques. After that, the two improvements (the sulfuric acid post-treatment and the GOPS addition) were described and analysed. The same measurements conducted after the fabrication were repeated after 15 days, in order to check the stability of these devices during time. Then, the first detection measurements with StpHRP and VEGF are analysed and finally the first real-time characterizations are reported.

4.1 Fabrication process

After the fabrication of the electrodes, the wafer was cut and the samples were ready for the polymeric deposition (Fig. 4.1).

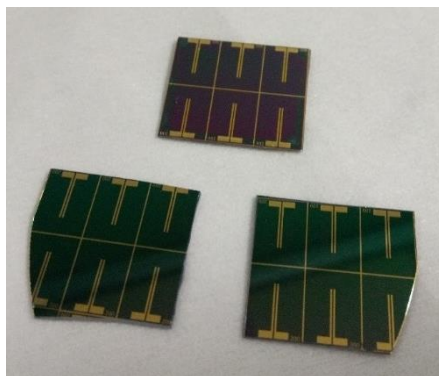


Fig. 4.1 – SPs with the gold pattern.

The two samples fabricated without treatments were covered by DI water for 5 minutes. Several cracks formed on the spin-coated film, while the ink-jet printed channel showed various folds. The corresponding images of the residual polymeric film obtained by optical microscope are shown in Fig. 4.2. For longer times (from 10 min upwards), the ink-jet printed channels completely detached from the substrate. It was verified that the employment of only *Clevios* led to form a polymeric channel with poor and inadequate adhesion for electrolytic measurements. For this reason, these samples were excluded to the measurements, including characterisation and functionalization, proving the necessity of some improvements.

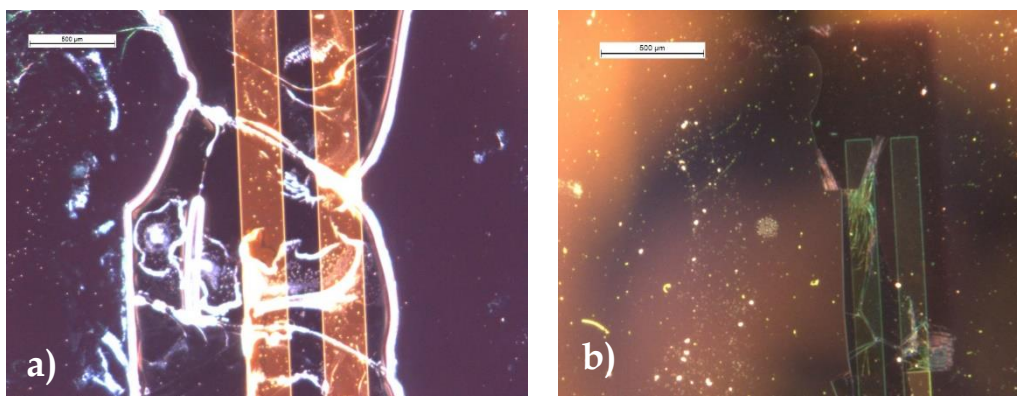


Fig. 4.2 – Device fabricated from *Clevios* solution without improvements. The pictures show the spin-coated channel (a) and the printed channel (b) after a short water covering. (The scale bar indicates 500 μm).

The enhancements reported in this work are useful also to avoid these undesired effects: the H_2SO_4 treatment modifies the polymeric structure creating a crystalline domain, instead the GOPS addition allows the formation of bounds

with the substrate and between the polymeric chains, so both improvements made possible the measurements with aqueous solutions.

All samples were completely immersed in DI water for 5 minutes and then observed under the optical microscope⁵ (Fig. 4.3). The spin-coated films presented more straight boundaries than the printed ones. Further, the film obtained by ink-jetting showed clearly a striped surface, that is due to the way by which the print-head deposits the droplets for the generation of the pattern.

Concerning the thickness of the channels, Table 4.1 summarises the minimal and maximal values (expressed in nanometers) for each type of device, measured by the profiler.

For *Clevios* solution, the printing settings used in this work led to the generation of a printed polymeric film twice as thick as the spin-coated one: the ink-jet printed channel showed a thickness of 100 nm more than the spin-coated channel. The conducting properties of these films might be different, due to the

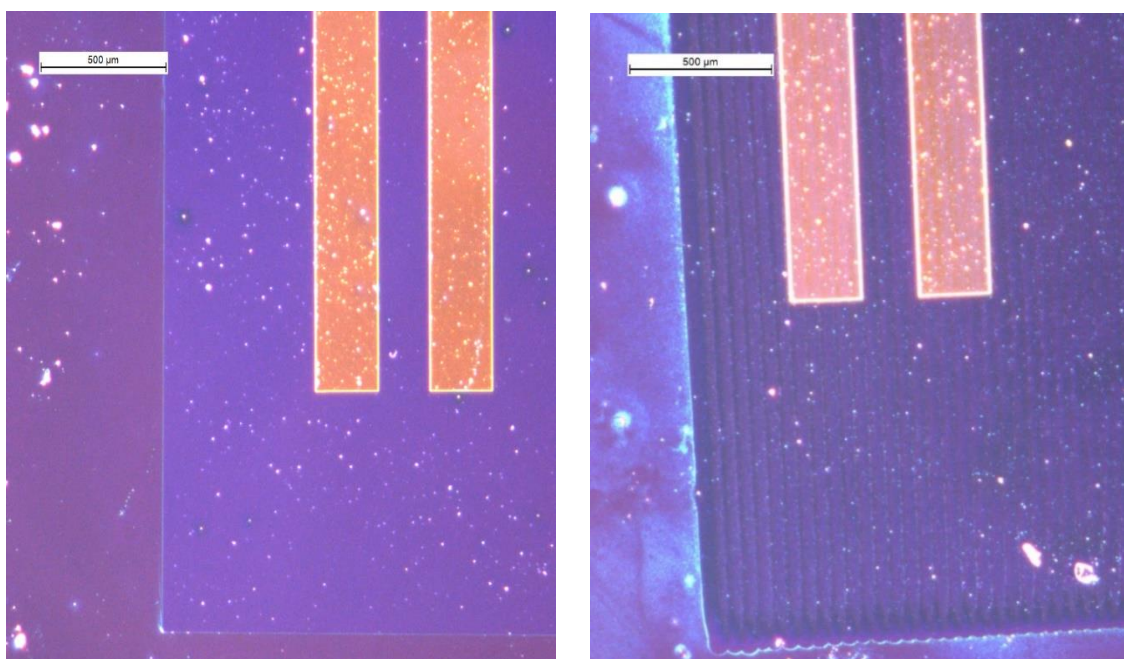


Fig. 4.3 – The difference in the surface morphology between the deposition techniques is clearly visible in GOPS devices: a spin-coated sample (a) and a printed one (b).

⁵ The little white spots in the pictures are only dust or residual water droplets, deposited on the device surface, because the observation was made outside the clean room, near the ink-jet printing apparatus.

	H₂SO₄		GOPS	
	min (nm)	max (nm)	min (nm)	max (nm)
Spin-coating	85	100	70	90
Ink-jet printing	185	200	75	95

Tab. 4.1 – The channel thicknesses, grouped by deposition techniques and improvements (all the samples were analysed with the profiler and the extreme values).

close relationship between the volumetric dimensions of the channel and the current flow.

Both kind of devices with GOPS addition presented the same thickness, thus they are perfectly comparable: the ink-jet printed channel (with the optimized printing setting reported in the previous chapter) achieved the same dimensional characteristic of the spin-coated one. The deposition, through ink-jetting, led to generate a film thickness between 75 nm and 95 nm, quite similar to the spin-coating technique (70 nm-90nm). The printing needed only 5 min to complete the deposition of the channel and further steps for the definition of the pattern (as for spin-coating) are no more necessary.

In general, the characteristics of the ink (the viscosity and the surface tension, as reported in Section 2.2.1), an inevitable optimization process for the printing setting and a difficult control in the film thickness represent the main limitations of ink-jet printing in this kind of application. However, after the definition of these initial steps (the eventual solution preparation, the individuation of the optimal settings and the characteristics of the printed film), only the final printing process must be repeated and the geometry of the pattern can be changed independently from all the preparatory processes.

After these considerations, the samples were completed, with the installation of the 120 μL chamber, as shown in Fig. 4.4.

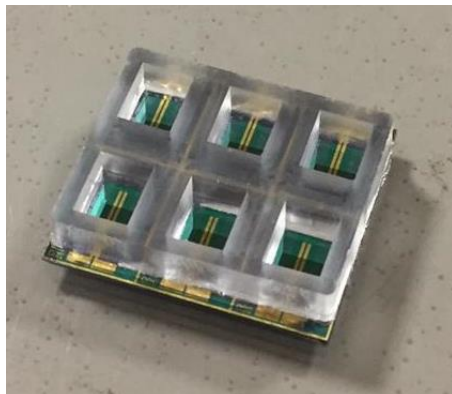


Fig. 4.4 – A completed SP, ready for the in-liquid measurements.

4.2 Electrical conductivity enhancement

The transconductance represents one of the most widely remarkable figures-of-merit for transistors, as explained in the beginning of Chapter 1. The most conductive devices, involving an untreated-PEDOT:PSS channel, exhibit a maximum transconductance of about 4 mS [16] (see Fig. 4.5).

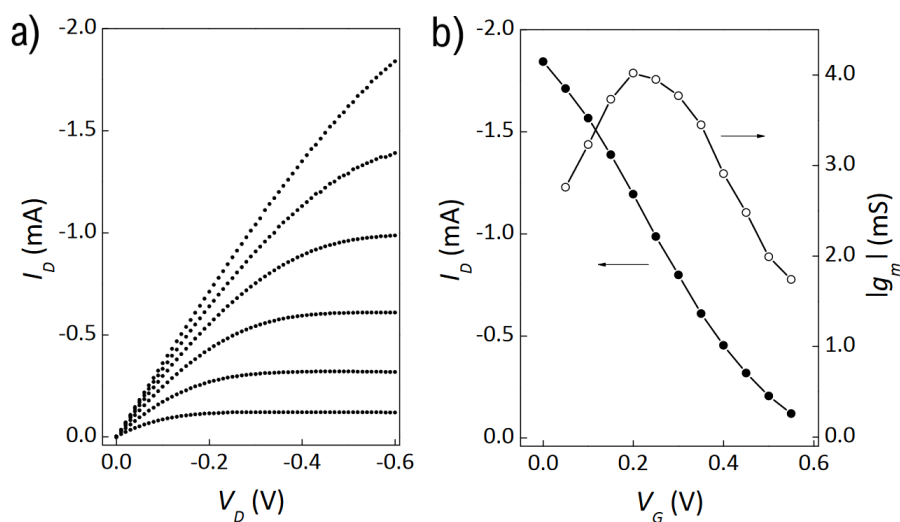


Fig. 4.5 – The output and transfer characteristics of a PEDOT:PSS OEET, fabricated with untreated Clevis PH1000 ($W=10\mu\text{m}$, $L=10\mu\text{m}$, $T=400\text{nm}$) by spin-coating on glass, after the deposition of an adhesion layer of parylene-C [16].

Many pre-deposition and post-deposition treatments for the conductivity improvement are reported in literature. The one which allows the largest increase in conductivity is the sulfuric acid treatment after the film deposition [9], in which the thin PEDOT:PSS structures are immersed in a solution of H_2SO_4 for 10 minutes at room temperature and then rinsed with deionized water. The maximum value of conductivity is obtained at 100% H_2SO_4 concentration. Two molecules of H_2SO_4 in concentrated H_2SO_4 solutions undergo autoprotolysis, generating two ions:



When these ions are in contact with PEDOT:PSS, they stabilize the segregated states of $PEDOT^+$ and PSS^- . The pristine PEDOT:PSS structure rearranges itself, forming superior PEDOT networks, due to the formation of crystallized nanofibrils [65] (Fig. 4.6).

A crystalline structure in conductive polymers facilitates the intra- and interchain charge transport, leading to a highly conducting state [65–67]: the holes can easier move through the vertical edge-on and horizontal π - π orderings, formed by the crystallization of PEDOT:PSS [67] (see Fig. 4.7).

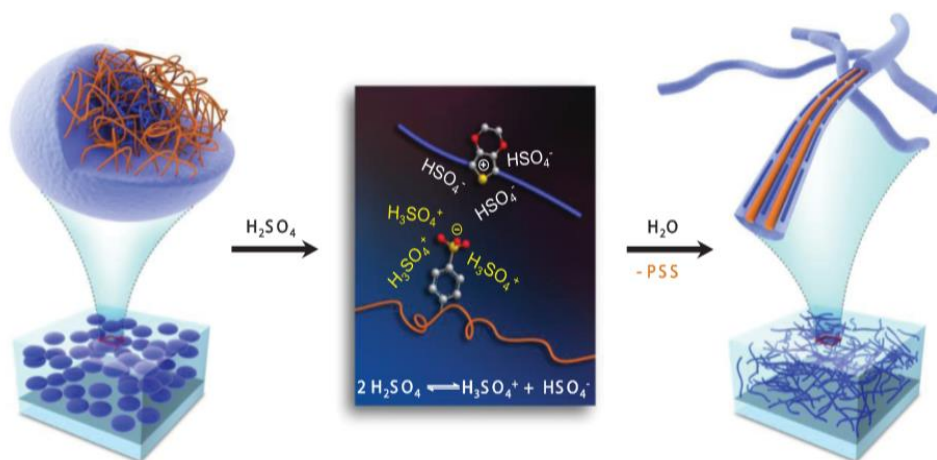


Fig. 4.6 – Scheme of H_2SO_4 treatment. The amorphous chains of PEDOT:PSS (on the left) are rearranged into crystalline nanofibrils (on the right) through a charge-separated transition mechanism, reported in the middle of the picture [65].

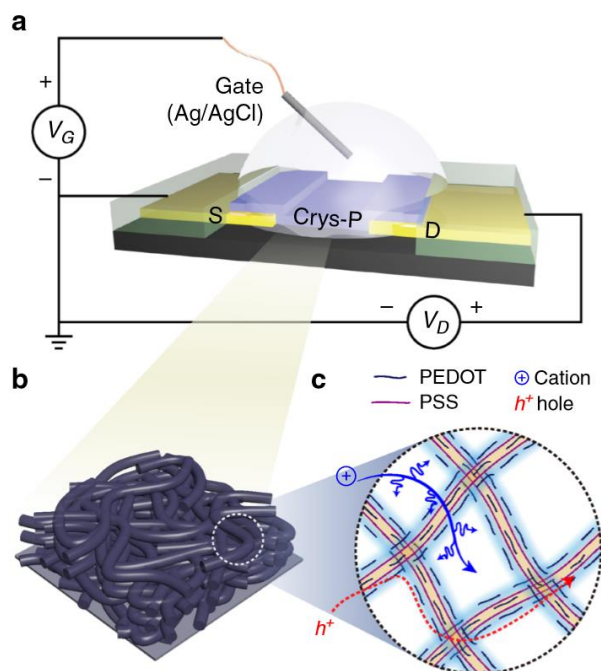


Fig. 4.7 – The crystallized polymeric film and its microstructure, which enhances the hole and ion transport [67].

This treatment causes another phenomenon inside the PEDOT:PSS complex: PSS is selectively removed by H_2SO_4 , without influencing the PEDOT regions. The H_2SO_4 and the uncoupled PSS are washed out by a sufficient amount of water, then the minimal quantity of PSS is reorganized with PEDOT and acts as counterion [65]. The 100% H_2SO_4 treatment can remove more than 70% of the PSS from the pristine PEDOT:PSS.

Even though the crystallized polymer exhibits a highly ordered film microstructure, cations can still access the PEDOT chains throughout the whole film for dedoping: the removal of excess PSS and thus a uniform PSS dispersion enhanced the nanoporosity of the film, permitting the enhanced ion transport into highly crystallized PEDOT:PSS domains for dedoping PEDOT chains [67].

In this treatment the H_2SO_4 acts as a solvent and the crystalline order is induced at low temperature and exhibits the highest conductivity (up to 4380 S/cm for 100% H_2SO_4 concentration) among solution treatments. In fact, a crystalline structure of PEDOT:PSS allows to obtain a five-times higher transconductance (up to about 19 mS [67]) than an amorphous one, as shown in Fig. 4.8.

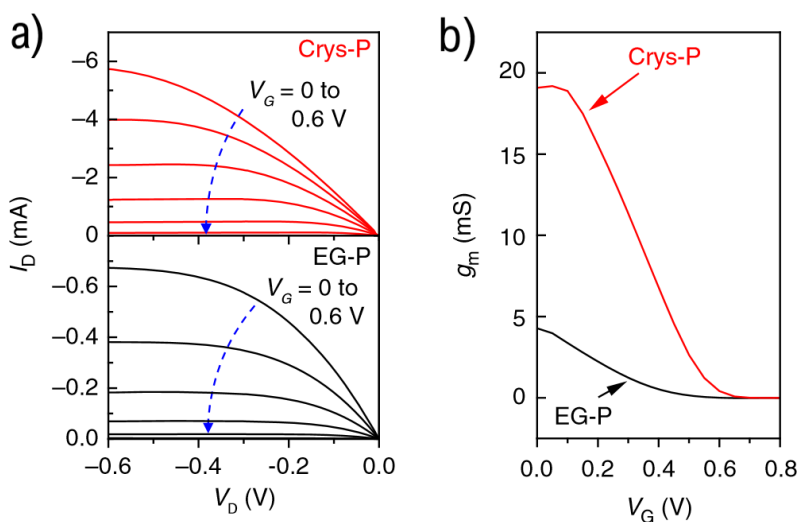


Fig. 4.8 - The output curves and the transconductances of a OEET, treated by sulfuric acid (>95% for 15 min), called Crys-P and of a untreated one, which contains only PEDOT:PSS and ethylene glycol, named EG-P. These channels have been designed with $W=80\mu m$, $L=20\mu m$ and $T=200nm$ [67].

In this work, the H_2SO_4 spin devices exhibited an average transconductance of 17.4 mS and a maximum value of 19.6 mS (in Fig. 4.9a, the experimental transfer curves and the computed g_m of three H_2SO_4 spin devices are reported). The peak transconductances were obtained at $V_{gs}=0$ V. The on-state currents achieved a value of -13 mA, in one case, and -9 mA in the other two devices. At $V_{gs}=1$ V, I_{ds} remains still between -2 mA and -1 mA, indicating a good de-doping of PEDOT, but an incomplete switching-off of the device.

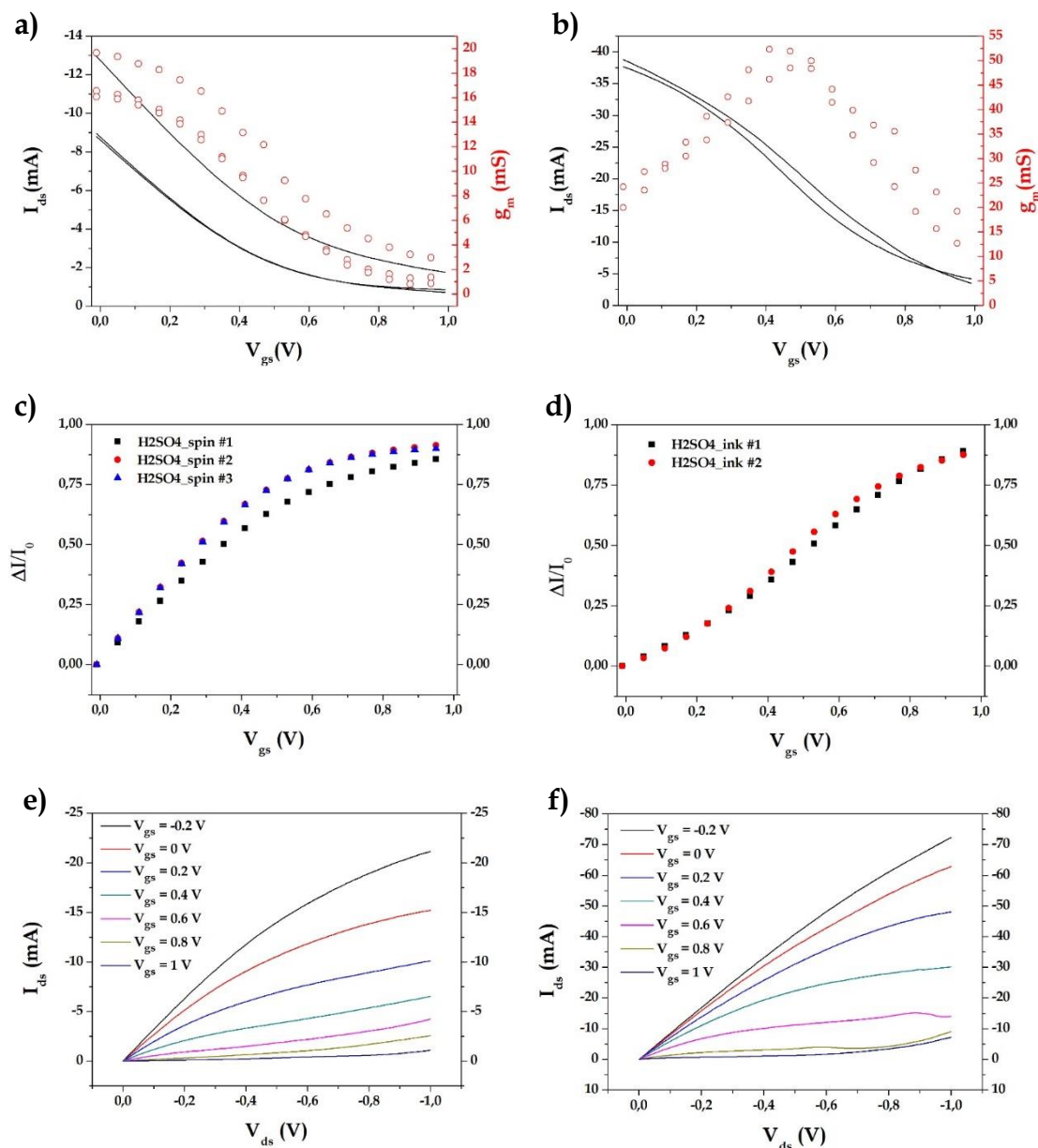


Fig. 4.9 –Comparison between H2SO4_spin (left column) and H2SO4_ink devices (right column): transfer curves and transconductances (a,b), normalized currents (c,d) and output curves (e,f).

Concerning the ink-jet printed OECTs (Fig. 4.9a), the transconductances achieved higher values than the spin-coated ones, likely due to the higher thickness of the printed channel. The average peak transconductance of 51.4 mS was obtained at higher gate-source voltages, between 0.4 V and 0.6 V. The maximum achieved value of g_m was 52.9 mS. The I_{ds} current showed a higher changing from about -37 mA to -5 mA, thus the devices did not switch-off completely for $V_{gs} < 1V$.

In order to evaluate the current modulation by the application of the gate-source voltage, the normalized current was calculated from the transfer curve, as:

$$\frac{\Delta I}{I_0} = \frac{I_{ds} - I_0}{I_0}; \quad \text{where } I_0 = I_{ds}(V_{gs} = 0 \text{ V}) \quad (4.3)$$

I_0 is the on-state current, that corresponds to the drain-source current upon no-bias application. This operation allows to observe better the changing of the drain-source current with respect to the initial current value, in particular for OECTs operating in sensing mode, as it provides information about the detection of analytes excluding secondary effects, such as instabilities, that could hinder the sensing response [24]. For $H_2SO_4_spin$ devices (Fig. 4.9c), the larger variation is shown at low gate voltages, indicating a better current modulation in the range between 0 V and 0.4 V. Despite of the high transconductance of $H_2SO_4_ink$ devices, the normalized current (Fig. 4.9d) shows that the modulation trend is less increasing compared to spin-coated devices. For example, a modulation of 0.5 is achieved at about 0.5 V in $H_2SO_4_ink$ devices, while in the $H_2SO_4_spin$ ones only 0.3 V were needed.

The output curve of $H_2SO_4_spin$ devices (Fig. 4.9e) shows an incomplete saturation inside this range of V_{gs} and reaffirms a scarce current variation for gate-voltages higher than 0.6 V. The device is more sensitive to the current modulation due to V_{gs} variation for more negative values than -0.4 V of drain-source voltage. On the other hand, $H_2SO_4_ink$ devices also did not achieve the saturation, as shown in their output characteristic curve (Fig. 4.9f), and a good current modulation is obtained only for a more restricted range of V_{ds} .

4.3 Adhesion enhancement

In order to prevent the delamination of the polymeric film on the substrate, Hakansson et al. [68] proved the efficiency of the addition of (3-glycidyloxypropyl)trimethoxysilane (GOPS) in the PEDOT:PSS solution. In fact, on one side, the introduction of PSS stabilizes the oxidation state of PEDOT, conferring also water solubility to the conjugated polymer, as pointed out previously. On the other hand, the deposition of PEDOT:PSS films for biosensors gives rise to problems in long-term applications, due to their low mechanical stability, especially in the case of immersion in aqueous media [9].

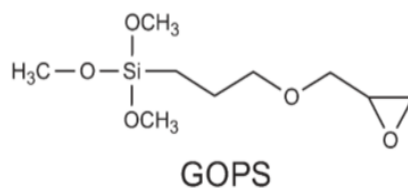


Fig. 4.10 – The chemical structure of GOPS with the methoxysilane group (on the left end) and the epoxy ring (on the right extremity).

The epoxy ring of GOPS binds to the SO_3H^- group of excess PSS, while its methoxysilane group binds to the hydroxyl group on the substrate or to other GOPS molecules. Thus, GOPS acts as a cross-linker, allowing a triple bonding: GOPS-GOPS, GOPS-PSS and GOPS-substrate (Fig. 4.11).

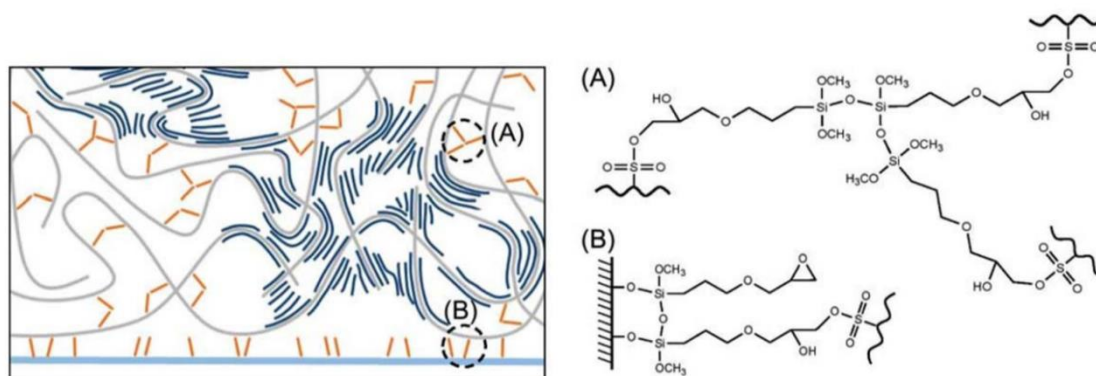


Fig. 4.11 – Schematic representation of the cross-linking due to the addition of GOPS in the polymeric solution. GOPS binds only to the PSS domains (grey chains), not to PEDOT chains (in dark blue). The three interactions of GOPS are indicated by the dashed circles and the relative chemical bounds are reported on the right. (A) shows both the cross-links between GOPS molecules and between GOPS and PSS. (B) indicates the bound GOPS-substrate (in this case the substrate is glass, exposing hydroxyl groups) [68].

GOPS does not interact with PEDOT, but forms a siloxane network, which reduces the charge carrier density and the charge carrier mobility [68]. These phenomena lead to a decrease in electrical conductivity of the polymeric films, as the GOPS content is increasing.

The conductivity of GOPS-treated PEDOT:PSS films is reduced by one order of magnitude, upon addition of only 0.1% *v/v* GOPS. For contents larger than 1% *v/v* GOPS the conductivity remains quite constant, saturating at values around 0.002 S/cm.

The reduction of ionic conductivity, which modulates OECT current in the channel, is larger than the drop in electrical conductivity, due to the reactions between GOPS and PSS in the PSS-rich regions, where ions move [68,69].

For all these reasons, the addition of GOPS prevents both dissolution of the PEDOT:PSS film and delamination from the substrate, but worsens the electrical performances of the film (Fig. 4.12).

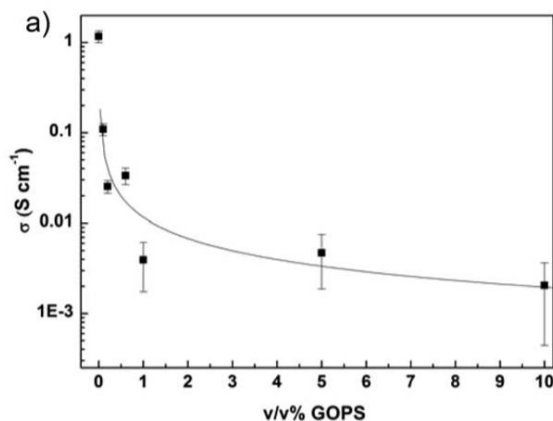


Fig. 4.12 – Variations in conductivity at increasing GOPS addition volumes [68].

In fact, the transfer and output characteristics of the devices fabricated from *Clevios+GOPS* solution showed lower current flows and lower transconductances than the acid-treated ones. Fig. 4.13 summarizes the characteristic curves of two significant examples of each type of device: on the top, an example of a *GOPS_spin* sample and on the bottom a *GOPS_ink* one. The maximum on-state current of -3.7 mA was obtained from ink-jet printed devices, as the maximum transconductance (about 14 mS). With all devices the saturation was achieved also for drain-source voltages of -0.5 V at $V_{gs}=0$ V and $V_{gs}=0.2$ V.

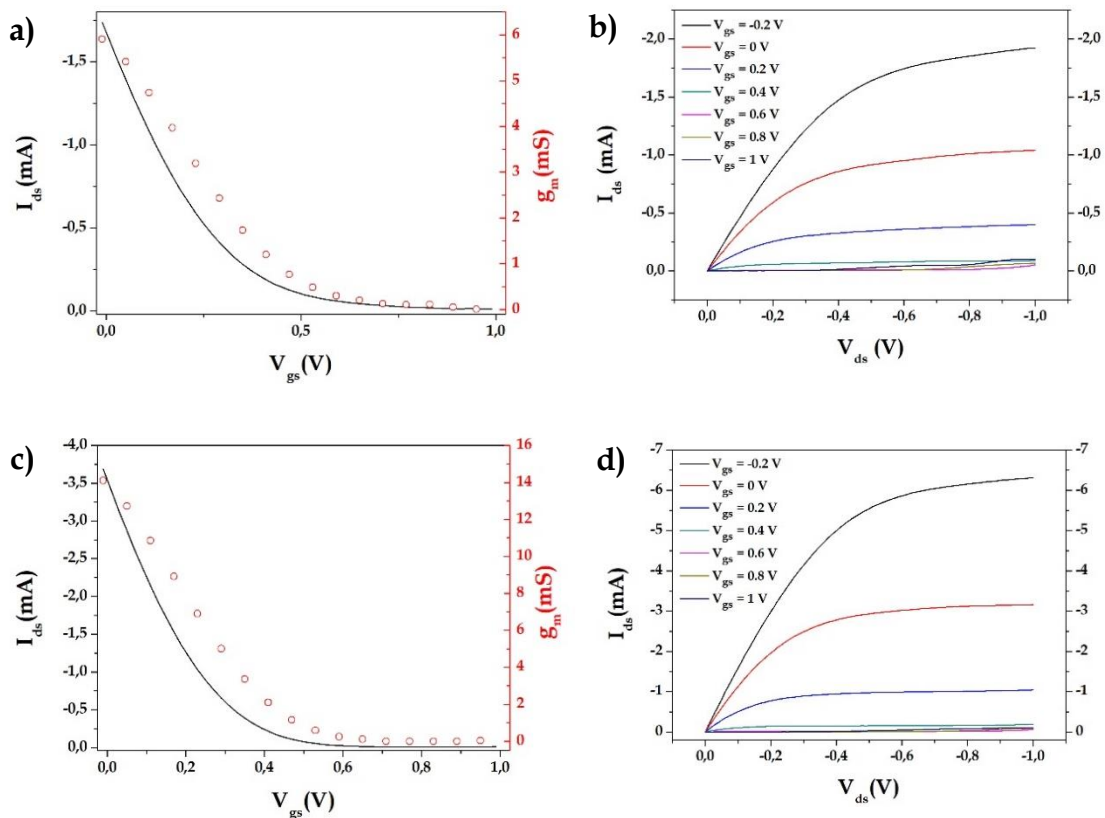


Fig. 4.13 – On the top: the transfer (a) and the output (b) curves of a GOPS_{spin} device. On the bottom: the corresponding curves of a GOPS_{ink} device (c,d).

After these characterisation measurements, the channels with GOPS addition showed a better stability than the others. In Fig. 4.14, the pictures of the different devices are reported. On the left, the channels treated with sulfuric acid show small cracks and a more damaged surface, globally. The devices with GOPS addition, shown on the right, exhibit a preserved surface, even after the measurements.

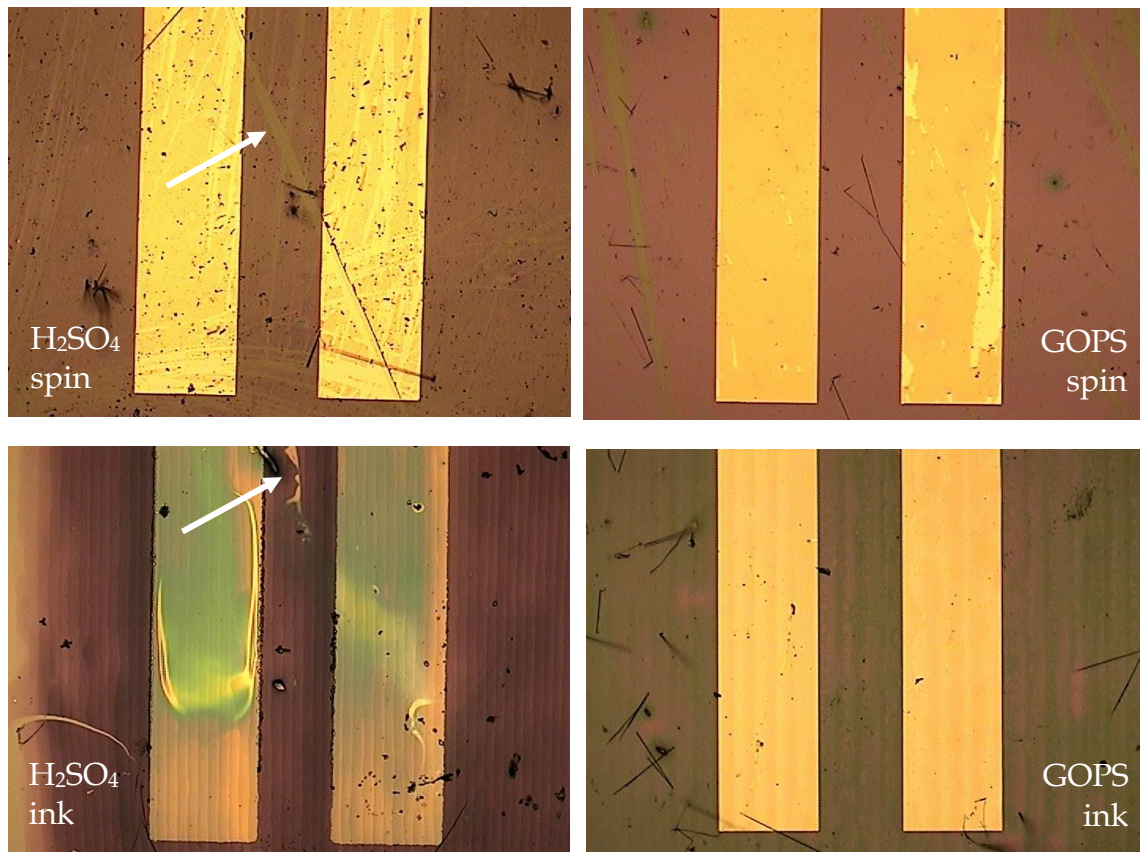


Fig. 4.14 – The surfaces of the different kinds of devices, obtained under optical microscope.

4.4 Stability after 15 days

The transfer characteristic curves were repeated after 15 days from the first characterization measurements, reported in Fig. 4.9.

The following picture (Fig. 4.15) shows the complete curves of the devices treated by sulfuric acid (sweep of V_{gs} from -0.75 V to 1 V): the first measurements are reported with dashed lines, instead the after-15-days curves are shown in solid lines. The red and the blue curves indicate the spin-coated and the ink-jet printed channels, respectively.

The spin-coated devices showed a considerable reduction in current flowing: the on-state values have been almost halved. In this condition, they can achieve the completely off-state at about 0.5 V. The printed devices showed a lower decrease in the current flow, achieving however values of about -34 mA at $V_{gs}=0V$. Even

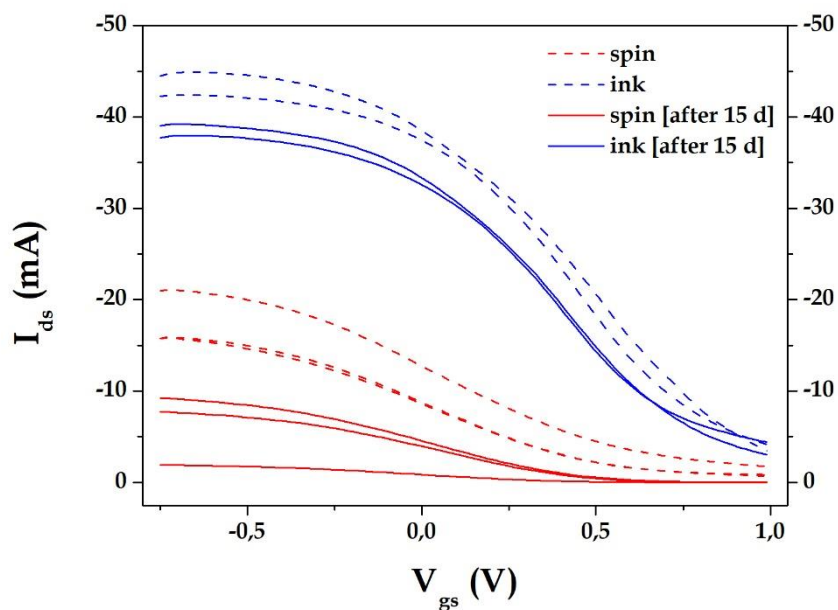


Fig. 4.15 – Comparison between the first measurements (after the fabrication), shown in dashed lines, and the curves after 15 days, reported in solid lines. The different colours indicate the different deposition techniques.

in this situation, the devices were not able to switch off, in fact I_{ds} remained still at -4 mA at $V_{gs}=1$ V.

In order to evaluate the transduction capability, the transconductances were computed and grouped by technique (see Fig. 4.16): the spin-coating is coloured in red, the ink-jet printing is indicated in blue. The first boxplot of each couple, with a low intensity of colour, refers to the first measurement, the others indicate the measurements after 15 days. The ink-jet printed channels maintained a good transconductance of about 47 mS, while the spin-coated ones achieved only a maximum transconductance of 10.7 mS.

Concerning the devices with GOPS addition (Fig. 4.17), all samples showed a great decrease in the current flow, which achieved only few milliamps (less than -2 mA) at $V_{gs}=0$ V. In these cases, all devices completely have been switched off at about 0.4 V.

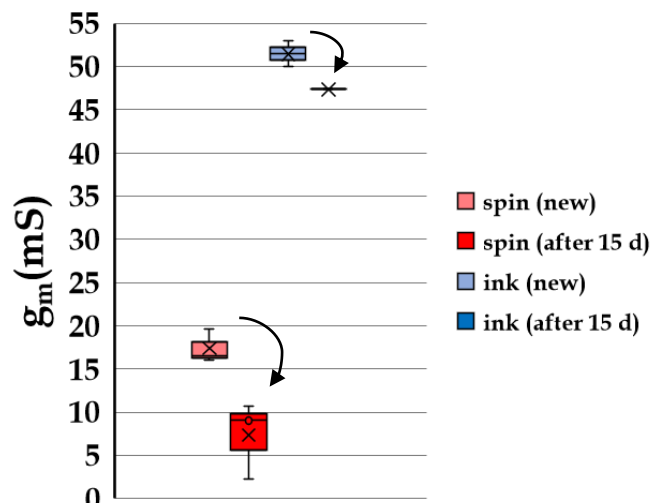


Fig. 4.16 – The maximum transconductances of the acid-treated devices. From the left: the first boxplot represents the g_m of H₂SO₄_spin devices, the second one shows the g_m of the same device after 15 days from the fabrication. The third boxplot refers to the H₂SO₄_ink devices (just fabricated), the last one corresponds to the after-15-days g_m of the same device.

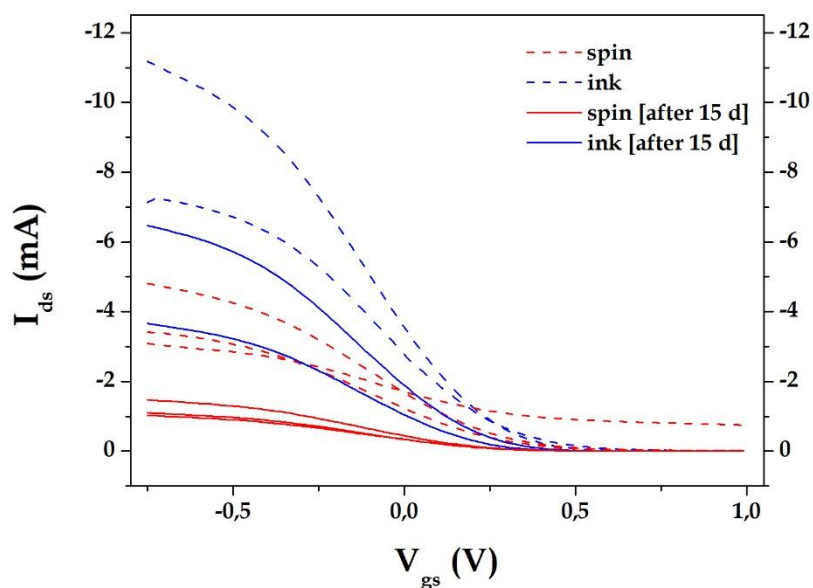


Fig. 4.17 – Comparison of the transfer curves of GOPS_spin (in red) and GOPS_ink devices (blue) just after the fabrication (dashed lines) and after 15 days (solid lines).

The maximum transconductances are reported in Fig. 4.18. Generally, the devices obtained from *Clevios*+GOPS solution exhibited low transconductances, if compared to the devices fabricated with the same deposition technique and with the acid post-treatment. For GOPS_spin devices, g_m decreased from a maximum value of 6.28 mS to a maximum of 2 mS after 15 days. The transconductance of

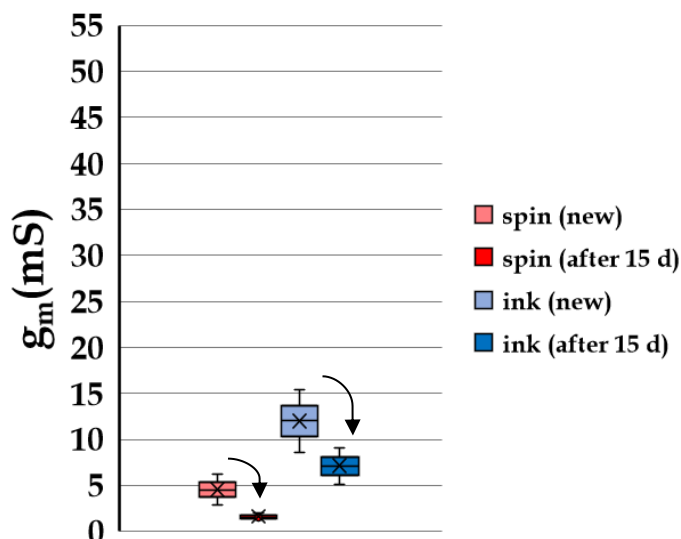


Fig. 4.18 – The variation in the maximum transconductances between the first measurements (first and third boxplot from the left) and the values after 15 days (second and last boxplot). The red couple indicates the same devices (GOPS_spin), while the blue one refers to GOPS_ink devices.

the ink-jet printed devices still showed a maximum of 9.1 mS with respect to the starting maximum value of 15.4 mS.

4.5 First detection measurements

For the first detection measurements, involving the gate functionalization, the devices with the higher I_{ds} variation as a function of V_{gs} were chosen: the $H_2SO_4_spin$ and the $H_2SO_4_ink$ ones (a single device of each type was sufficient to cover this whole cycle of measurements).

All measurements have been performed using different electrolyte solutions: PBS 0.1x and PBS 1x.

Fig. 4.19 shows the normalized current, obtained from the transfer characteristics of the $H_2SO_4_spin$ devices at the different steps of the gate functionalization: the pristine Au square electrode (bare), the electrode after the SAM process (SAM), the activation of the thiols (active. SAM), the incubation with StpHRP for 1 h (StpHRP 1h) and after an overnight incubation (StpHRP).

The functionalization of the gate electrode with the StpHRP molecules led to a higher variation in the current reduction. This phenomenon is more significant in PBS 1x solution, where the modulation of the current achieved a value of 0.50, after the overnight incubation.

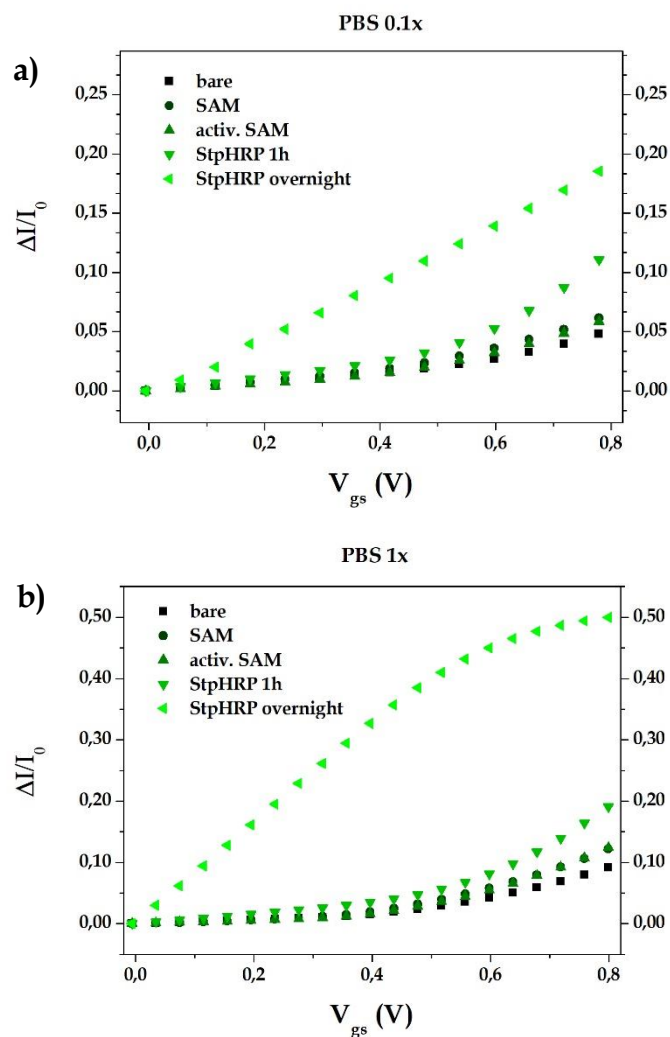


Fig. 4.19 – The normalized current at every step of functionalization in PBS 0.1x (a) and PBS 1x (b) in a H_2SO_4 _spin device ($V_{ds} = -0.5V$).

In the ink-jet printed devices, the current modulation through the effect of the functionalized gate electrode (Fig. 4.20) was less consistent: lower changes in current occurred and only at higher voltages (over 0.7 V in PBS 0.1x and over 0.8 V for PBS 1x).

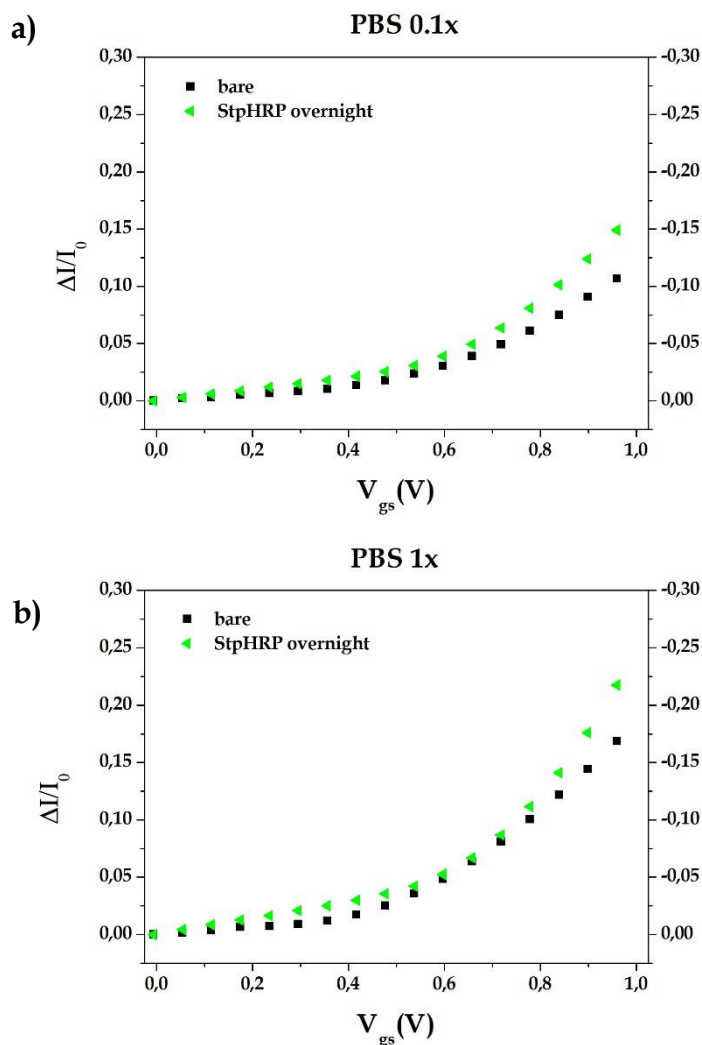


Fig. 4.20 – The current modulation through the functionalization with StpHRP in a $H_2SO_4_ink$ device ($V_{ds} = -0.5$ V).

The measurements involving aVEGF and VEGF were conducted with a single $H_2SO_4_spin$ device and using the same two electrolyte solution: PBS 0.1x and PBS 1x (see Fig. 4.21). The gate modification through the bonds with the antibodies resulted in a higher current reduction, due to the increased thickness of the double-layer and consequently a variation in the gate voltage. The bond between antibodies and antigens led to different behaviours in the current modulation: in the most of cases the curves of the antigens followed the same trend of the corresponding antibodies (Fig. 4.21a, c, d, f). In the other cases (Fig. 4.21 b and e) the VEGF curve showed a lower modulation than the one of the antibodies.

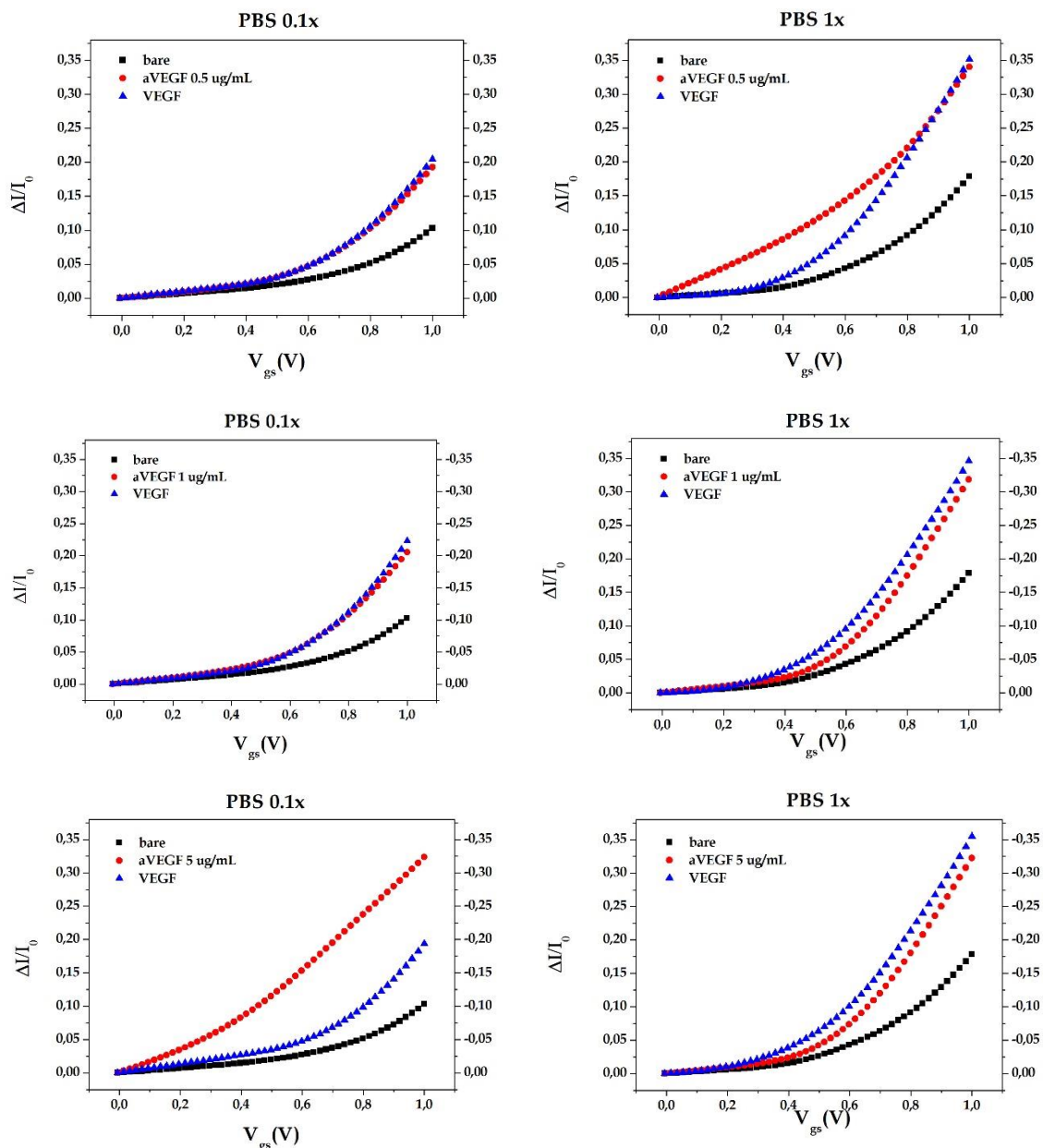


Fig. 4.21 – The normalized current in PBS 0.1 (on the left) and in PBS 1x (on the right). Different concentration of anti-VEGF (0.5 $\mu\text{g/mL}$, 1 $\mu\text{g/mL}$ and 5 $\mu\text{g/mL}$) were bounded on the gate electrode surface, instead the same VEGF concentration of 100 ng/mL was used for every sample.

It should be noted that these measurements were conducted in a static mode. The gate electrode and the solution were manually changed every time a new curve had to be obtained. Different factors could modify the conditions of these measurements, such as:

- a different gate surface exposed to the solution, thus a different quantity of exhibited biomolecules;
- a slightly different volume of solution;

- the presence of small air bubbles (due to the manually insertion of the solution by a micropipette, which could contain air bubbles, or due to the insertion of some air between the solution and the top covering of the electrolytic chamber).

Furthermore, the static measurements involve an already-assembled gate electrode: the direct effect of the bond between antibodies and antigens is not visible, because it occurs before the measurement step. Even increasing concentrations of antigen cannot be measured in sequence through this system.

For all these reasons, real-time measurements were promoted, allowing the analysis in a hermetic structure, with an automatic pumping of the solutions and a non-stop monitoring of the current over time.

4.6 Real-time measurements

The devices fabricated for the RTP were firstly characterised to check their proper functioning. The Ag/AgCl gate electrode and the solution of NaCl (see. Fig. 4.22) were used. Through the interdigitated electrodes, the channel exhibited a very high conductivity, achieving high values of current and the complete switching-off of the device at 1 V of V_{gs} . The saturation was achieved over -0.7 V at $V_{gs}=0$ V and at about -0.5 V between 0.2 V and 0.6 V of V_{gs} .

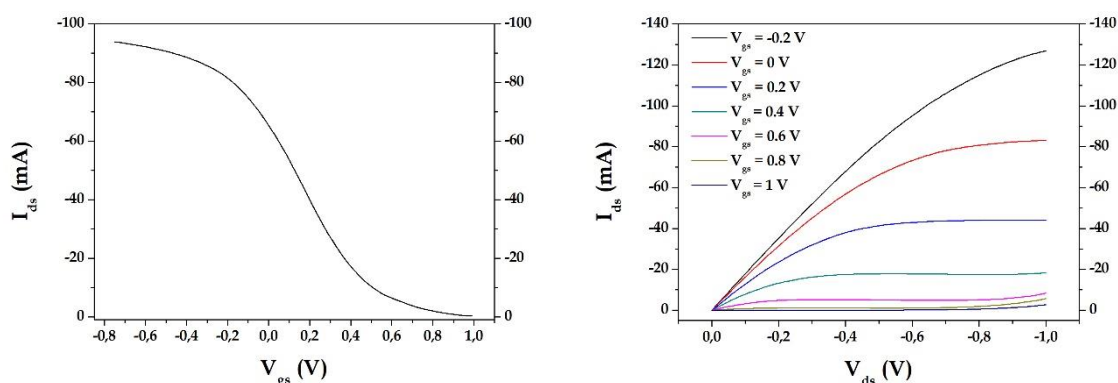


Fig. 4.22 – The transfer and output curves of the device used in RTP.

The complete RTP (Fig. 4.23) was assembled and filled by the automatic pump. Before the starting of the RTP characterization, the current must achieve the stabilization (an example is reported in Fig. 4.24).

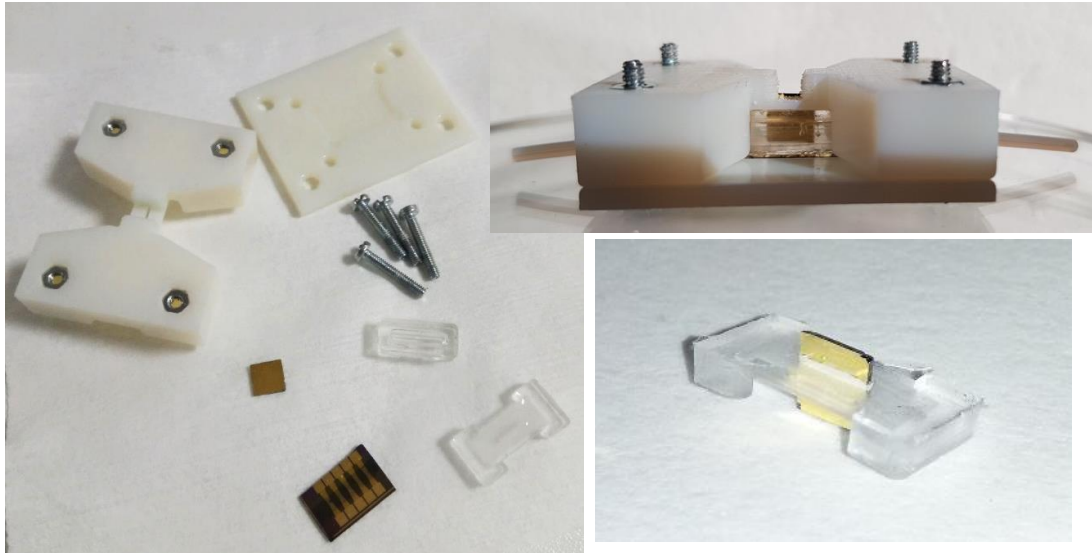


Fig. 4.23 – The RTP before and after its complete installation and a zoom on the positioning of the gate electrode in the chamber covering.

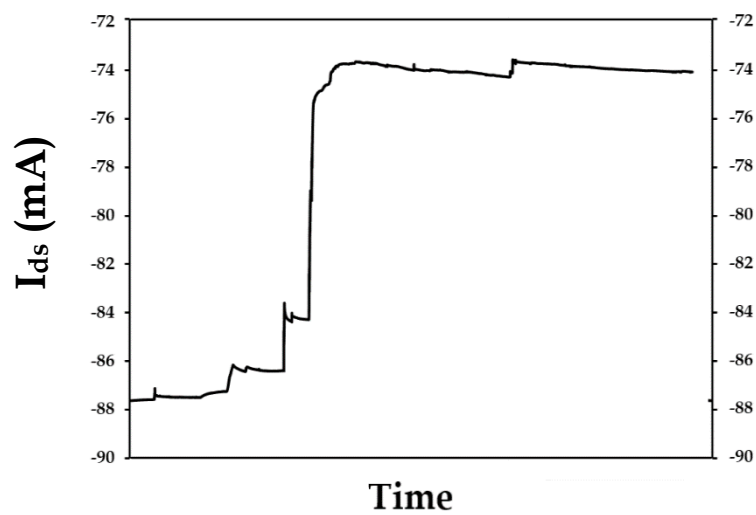


Fig. 4.24 – An example of current stabilization just after the solution pumping (before the beginning of this measurement the gate electrode was not completely covered by the electrolyte solution). $V_{ds}=-0.5$ V, $V_{gs}=0$ V.

The characterisation is useful for the individuation of the best values of V_{gs} and V_{ds} , that will be applied during the current measurements over time.

An exemplar output curve is reported in Fig. 4.26. It presents a very different shape, thus a totally different characteristic curve, than the one shown in Fig. 4.22. In this situation the current decreased only of about 30 mA. The gold gate electrode modified the transfer curve of the device, not allowing a proper working of the device and thus an easy choice of the best V_{gs} value for following measurements. Possible liquid leakages are the most probable reason of these difficulties during the measurements. Further study towards the resolution of this problem are still in process.

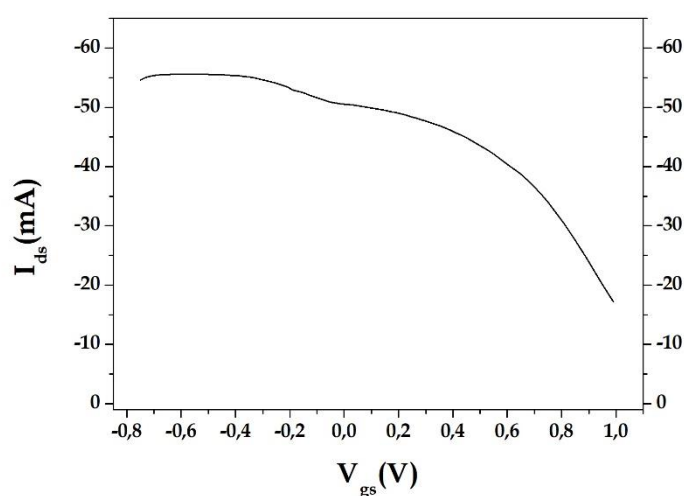


Fig. 4.26 – The transfer characteristic curve of the RTP at $V_d = -0.5$ V in PBS.

5. Conclusions and future works

The two improvements were successful, since the sulfuric acid post-treatment achieved higher values of current and transconductance and the GOPS addition maintained a preserved surface of the polymeric channel, even after the characterisation measurements. The ink-jet printed and acid-treated samples exhibited the maximum values of transconductance (52.9 mS), while the spin-coated ones achieved 19.6 mS. In both cases, they exceeded the highest value of transconductance (ca. 4 mS) of untreated-Clevios devices. After 15 days from the fabrication, the same devices have still maintained a maximum transconductance of 47 mS and 10.7 mS, for the ink-jet printing and the spin-coating, respectively. The GOPS devices showed under the optical microscope a preserved surface, without cracks or damages, which appeared on the acid-treated device instead. Concerning the geometries, the ink-jet printed channels reported a comparable thickness with respect to the spin-coated ones, but only in the samples with GOPS addition. Since the volumetric dimension of the channel is directly connected to the current flow through the channel, the acid-treated devices resulted not really comparable in their electrical performances.

For all these reasons, a deeper investigation of the morphology of the surfaces and a further optimization of the printing process for *Clevios* are clearly needed. Furthermore, a greater number of devices might be fabricated for a more solid statistical analysis. After these first necessary steps, different thicknesses of both spin-coated and ink-jet printed channels might be investigated and compared with respect of their electrical behaviour and also during real-time biosensing. A deeper study of the ink-jet printing technique can be conducted, testing different and/or more complex geometries for the pattern and different bio-applications, for example the employment of bio-inks for cell cultures or the nanoparticles deposition for flexible electronics.

Concerning the first detection measurements, the devices showed an evident reduction in the channel current with the StpHRP-functionalized gate electrode in acid-treated devices, fabricated by spin-coating. In the ink-jet printed ones, the variation was less consistent. The antiVEGF-functionalization and the subsequent bond with the VEGF led to a difficult interpretation of the current variation, mainly due to the static nature of these first measurements.

In conclusion, a better comprehension of the effects connected to the changing of the gate voltage after the surface modification and the solution of the problems related to the real-time platform are strictly necessary to continue and evaluate the measurement operations. After this, the functionalization with other more specific antibodies and antigens (for example biomarkers) can be explored. The analysis of more complex samples, such as saliva or serum, might be the last step of the whole design process of this kind of biosensors.

Appendix

Easy guide to Jetlab 4 ink-jet printer

During the thesis work an easy guide to the Microfab Jetlab 4 printing system was written. Here the most relevant issues are reported.

General description

For the usage of Jetlab, the following equipment is necessary:

- a white-light lamp, in order to obtain the right illumination for the cameras;
- a pressure pump, to flux the fluid toward the nozzle or to hold it;
- a filter with pore size of 0.45 μm , to remove particulates, also from DI water, which is used for testing and cleaning;
- water sensitive paper, if preliminary tests with water are necessary.

The printer is mainly constituted by the printer block and the front panel.

The main elements of the printer block (Fig. A1) are briefly described:

- 1- **Metallic holder:** it provides the cylindric slots for the piezoelectric nozzles, which are hold by small screws, present on the left side of this holder.

- 2- **Piezoelectric nozzle:** it consists in the more fragile element of the printer, due to its glass tip, which must not be damaged, because it constitutes the print-head of the system.
- 3- **Adaptor:** it represents the central block for all the connections. On the top the tubes from the pressure pump are visible, on the bottom the reservoirs can be fastened, and on the left the connector to the nozzle is fixed.
- 4- **Reservoirs:** they are small storage units, which contain the ink solution.
- 5- **Channel selection:** it manages the channelling of the pressure, coming from the pump system, and presents a manual valve for the selection of the channel (JET1 or JET2) or for the vent (VENT).
- 6- **Printing area:** metallic plate, on which the nozzle moves to complete the printing. It is provided by a specific Cartesian reference system (explained in the following paragraph).
- 7- **Lateral camera:** it allows the observation of the nozzle (if located in the *Maintenance Position* with the lowered head) and of the ink drop (ejected through the set values, after pressing the button: *Start Jet Continuous*).
- 8- **Superior camera:** it allows the view of the surface/substrate, on which the printing is required, and the obtainment of the accurate coordinates of the observed point.

The front panel (Fig. A2) shows some of the fundamental elements to control the printing system:

- **Emergency stop:** a manual emergency button, for the immediate stop of the ongoing printing process;
- **Purge pressure:** it is like an “instantaneous pushing pressure”. With the small black regulator, under the indicator, the pointer can be set at the desired value of this pressure. The *Positive* button must be pushed in order to apply this pushing pressure on the ink solution.
- **Back pressure:** this display shows the applied pressure to the ink inside the reservoir. It is displayed in psi.
- **Purge control:** it is the manual regulator of the back-pressure.

- **Positive/Vacuum:** pushing on *Positive* button, the *Purge Pressure* is supplied to the solution in the reservoir (it can be also a high instantaneous pressure, up to about 200 psi). This button is used to verify the verticality of the jetting and sometimes it allows the removing of particulates or impurities, still in the glass tip ending. Instead, pushing *Vacuum*, the ink is lead in the reservoir again, due to the vacuum effect on the connector to the nozzle.
- **Camera light:** this manual regulator can switch on and change the intensity of a red light, that is used to see gold elements on electronic devices placed on the printing area, though the superior camera.
- **Strobe delay:** the regulator can manually control the strobe delay, useful in the visualization of the drops, through the stroboscopic lateral camera.
- **Power:** an orange LED indicates that the printer is switched on.
- **USB:** the printer is provided with a USB port, connected to the internal computer.

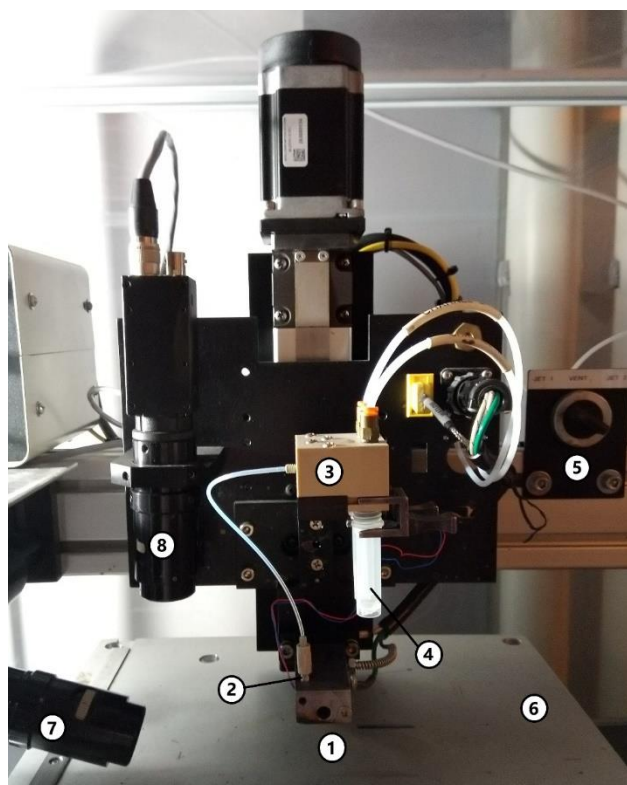


Fig. A1 – The printing block of Jetlab 4

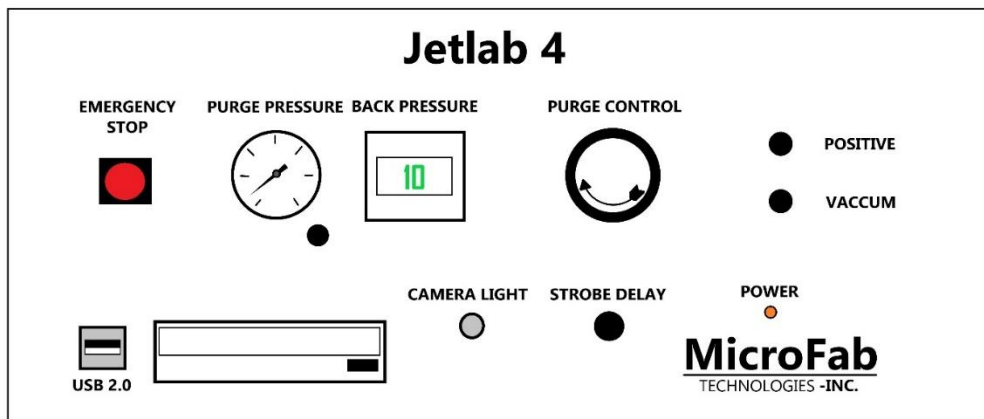


Fig. A2 – Scheme of the front panel.

Reference system

From a frontal view of the printer, the x - y Cartesian plane is placed as in Fig. A3a. The z -axis is direct upwards (see Fig. A3b) and its origin is located about 10 cm above the printing area. The coordinates of the *Maintenance Position* are: $(-128.496; -76.631; -93.202)$.

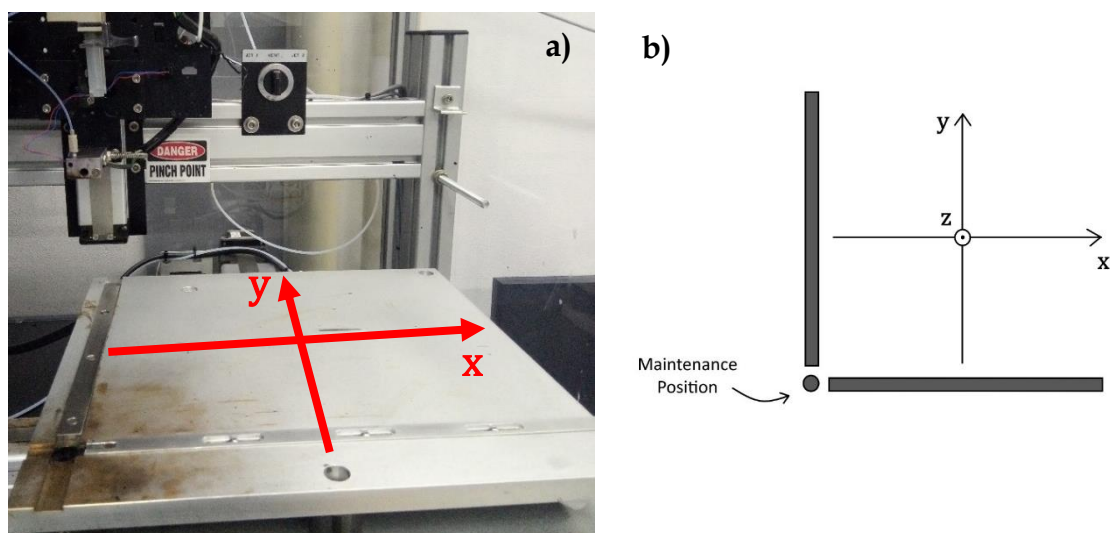


Fig. A3 – The reference system: the position of the x - y axes respect to the printing area (a) and a scheme of the x - y - z reference system (b)

Initialization and simple prints

To start, the printer must be switched on, and the internal PC will switch on directly. After opening the software *jetlab4.exe*, the pressure pump must be switched on, setting the back-pressure at 0 psi with the purge control.

In the main page of the software, the button *Go to Maintenance Position* is used to lead the nozzle in the position, where the drop jetting can be regulated and checked.

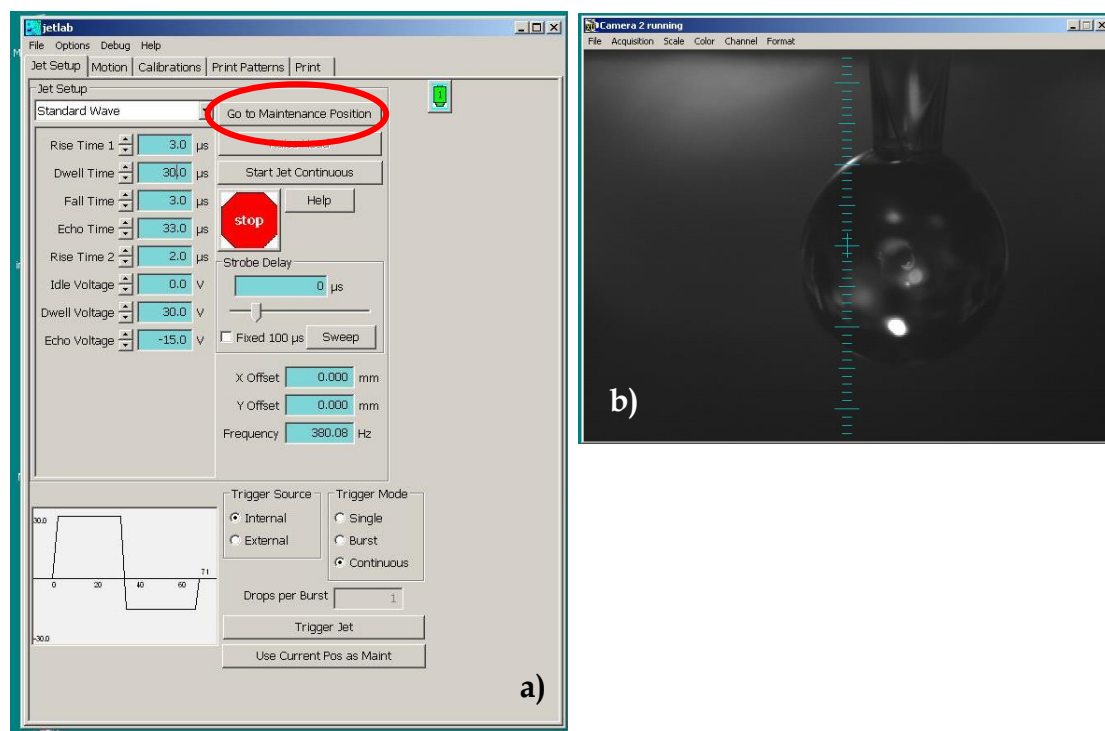


Fig. A4 – The section *Jet Setup* in which the nozzle can be moved to the *Maintenance Position*. In this section the waveform parameters can be set (a) and the drop jetting can be observed by the lateral camera. Picture b) represents the initial step of the back-pressure regulation, when the value is still set at 0 psi and the ink flows down only by the gravity.

At this condition, the drops can be observed by the lateral camera, and the back-pressure must be reduced until the formation of a meniscus.

After the setting of the driving waveform and the other parameters, this camera can show the ejected drops and eventual problems, related to the drop formation. The *Strobe delay* must be changed, until the jetting becomes visible to the camera.

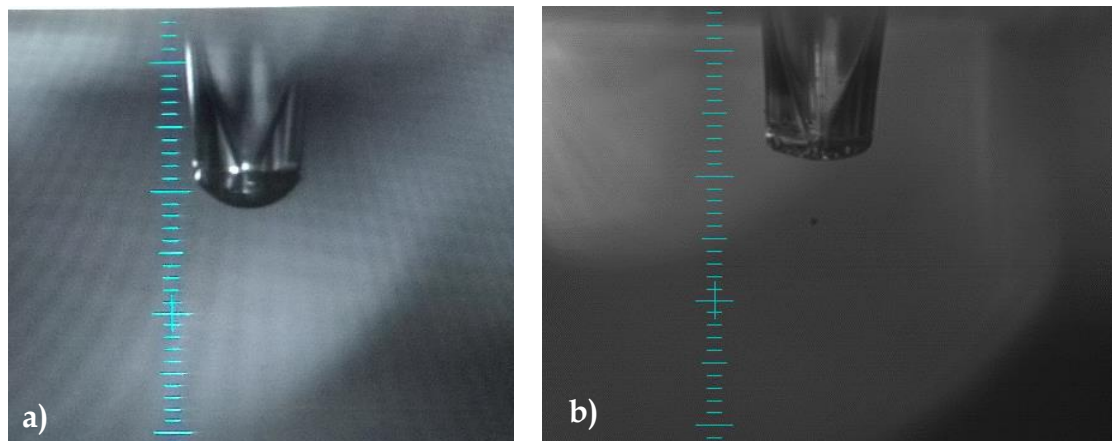


Fig. A5 – The formation of the meniscus upon the application of a negative back-pressure (a) and the visualization of the drop jetting during the checking of the driving parameters (b).

Start Jet Continuous enables the application, on the ink solution, of all the driving settings, allowing the modification of all parameters until the desired effect is obtained.

When the jetting is satisfactory, the button *Stop Jetting* ends the application of the voltage pulse.

To print simple elements, the section *Print* must be opened and some simple patterns can be chosen. For example, selecting *Straight line*, a line of drops can easily be printed, setting the starting coordinates, the drop distance, the number of drops (or the line length) and the angle.

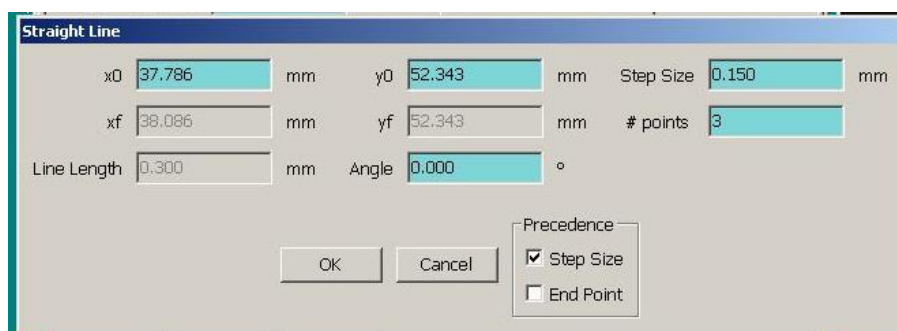


Fig. A6 – The settings for the generation of a simple line of drops.

Printing from digital models

The following programs allow the conversion of the digital model to a script, which can directly print the desired pattern. The model used in the thesis work is employed as example in the describing images.

- 1- **CleWin:** the desired pattern is built through the software *CleWin*. Specific markers, such as a cross or four squared elements, are inserted in the model and will be useful in the alignment process. The pattern is placed in a different layer with respect to the markers' one, in order to avoid the printing of both the elements. The file is saved in *GDS-II* format.
- 2- **GDS2Jetlab.exe:** after the opening of the software, the *.gds* file is selected and opened. The button *Set origin* is now activated, allowing the selection of the origin of the pattern model (Fig. A7).

A region, containing necessarily elements (the selection of an empty area is not permitted), must be selected. The origin will correspond to the center of mass of the selected area (Fig. A8a).

Then, pushing *Ok*, the *Set x direction* button is active and other elements (not empty zones) must be selected: their center of mass will define the x-axis in combination with the previous origin (Fig. A8b). In this way, the model is likewise oriented as the x-axis of the printing area and both origins are coincident.

The layer, which must be printed, is selected from the *Select layer* list: the elements, that will be printed, become red. The additional settings are adjustable through the window *Options>Spot Geometry* (Fig. A9), where:

- **Spot margin** represents the minimum distance between the center of the drop and the edges of the shapes in the pattern model.
- **Spot spacing** indicates the distance from the center of a drop and the centre of the adjacent one, inside the shapes.
- **Unit per meter** is the measurement unit of the previous parameters (Spot margin and spot spacing). The unit usually corresponds to micrometer, thus the value is set at 0.000001.

- *Fly velocity* represents the moving velocity of the nozzle during the printing. Jetlab 4 supports a maximum velocity of 50 mm/s. The Fly velocity/Spot margin ratio might be less or equal than 1000 Hz.

After all the parameters and settings have been set up, clicking on the button *Create script* a script (.txt extension) is generated, which converts all the chosen parameters and automatically adds functions, in order to adapt the digital model to the printer operating system.

- 1- **jetlab4.exe**: in the driver software, the .txt script is selected in the section *Print Patterns*, clicking on *Add Scripts* (Fig. A10a). The loaded script is now shown in the section *Print*, inside the drop-down menu (Fig. A10b). Before launching the printing, the *Offset* must be individuated through the alignment process, reported below.

A scheme of the whole conversion process is summarized in Fig. A11.

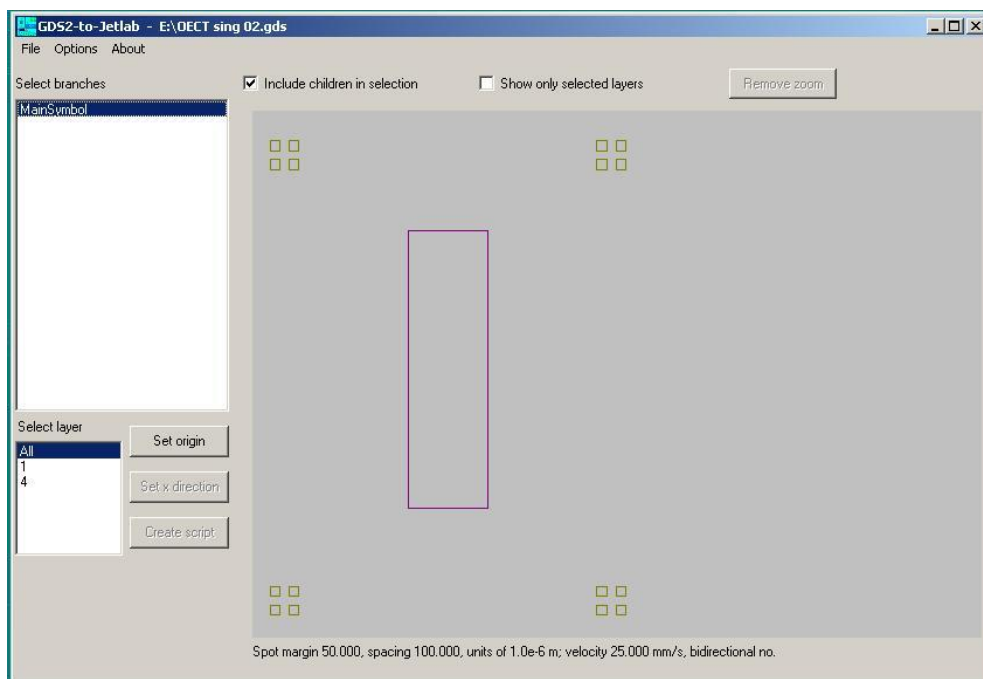


Fig. A7 – The .gds model was loaded inside GDS2Jetlab.exe and the button *Set origin* is active.

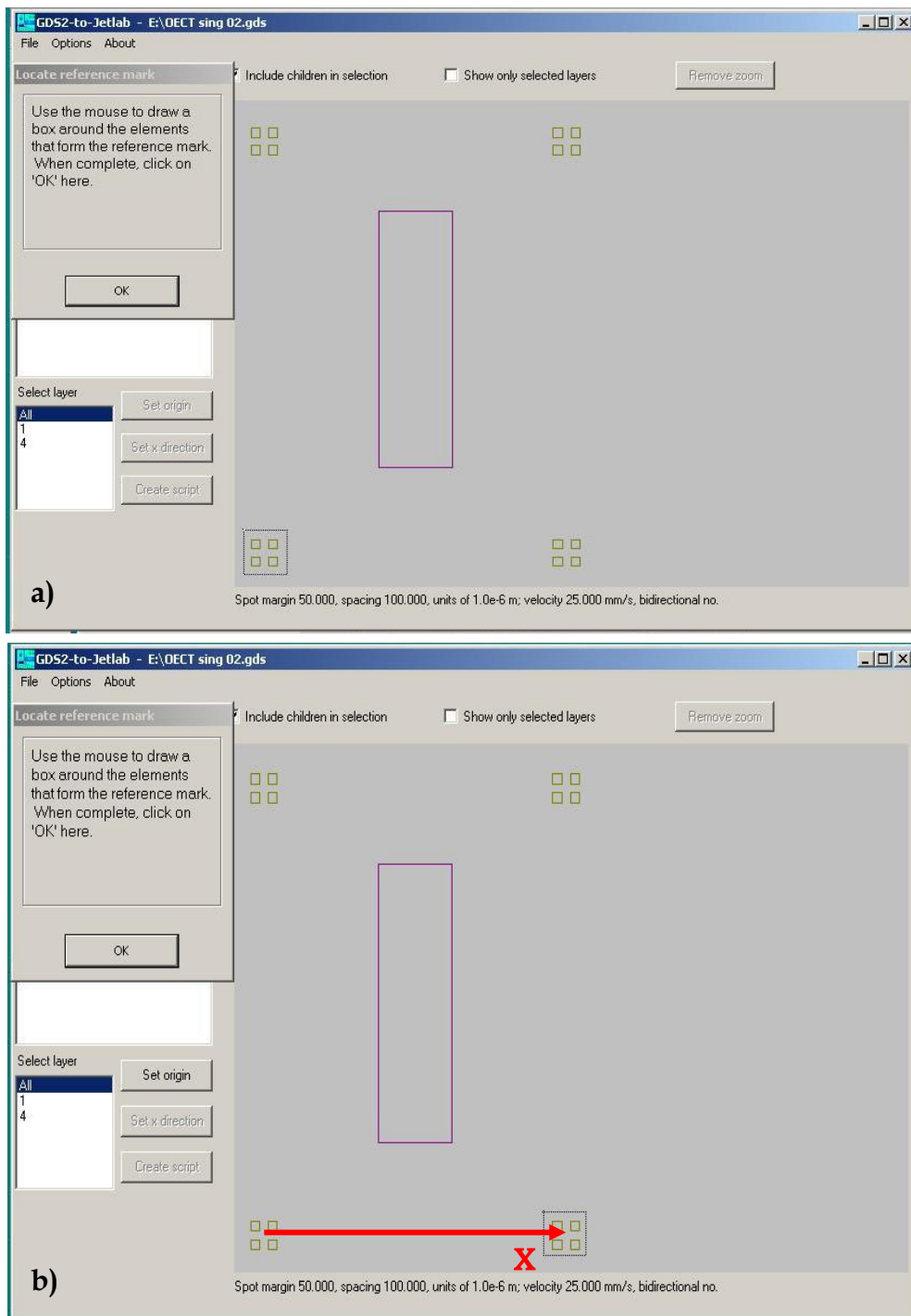


Fig. A8 – The selection of the elements which define the origin of the model (a) and then the x-axis orientation (b).

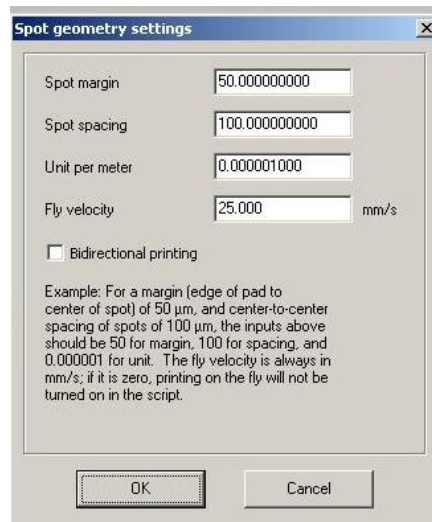
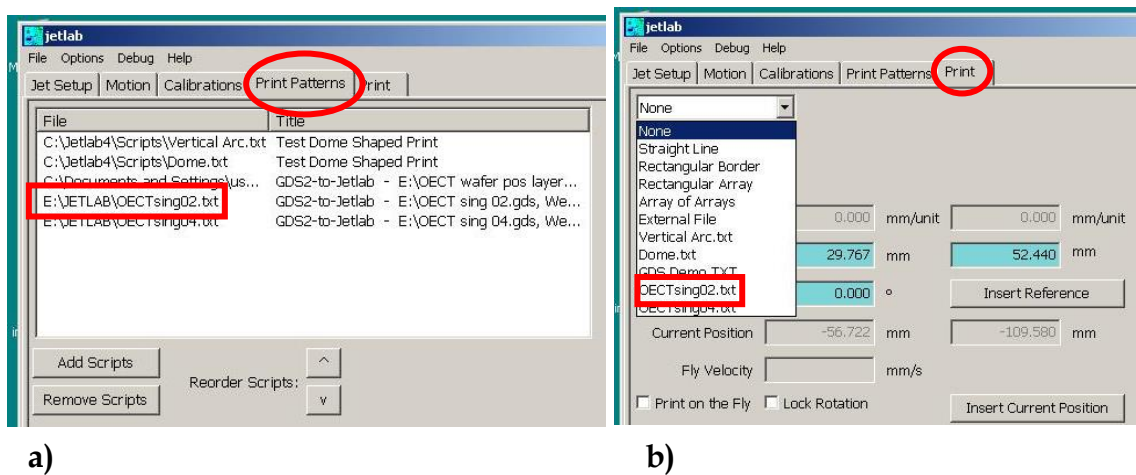


Fig. A9 – The additional setting which will be inserted in the script.



a)

b)

Fig. A10 – The loading of the script inside the section Print patterns (a) and the selection of the loaded script in the section print to proceed to the printing process (b).

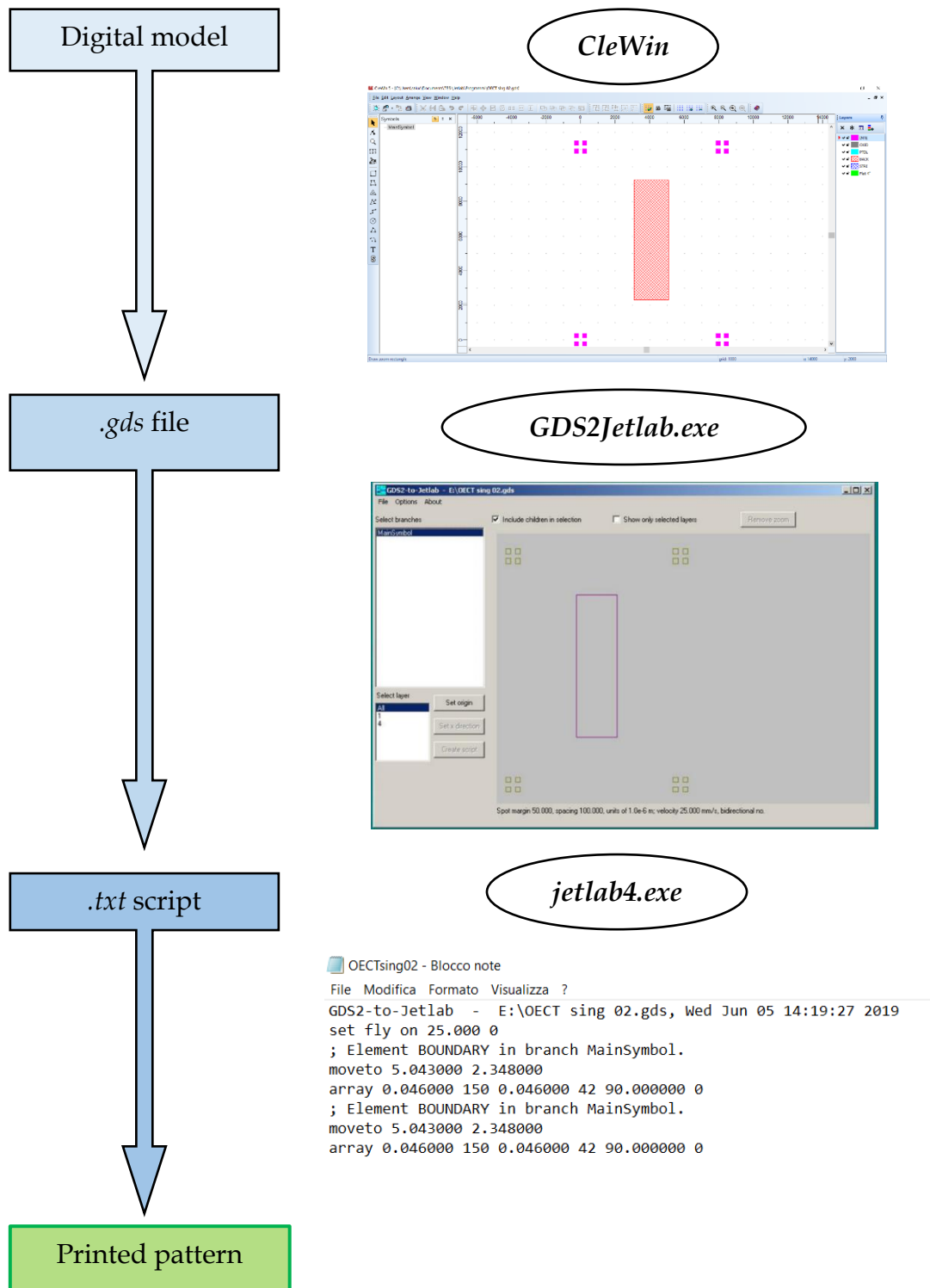


Fig. A11 – The summary of the whole conversion process.

Alignment process

The specific pattern involved in the thesis work is used again as practical example for the description of this process. Fig. A12 shows the whole model of the device:

the grey rectangle represents the pattern to be printed, while the violet objects are elements, which are still on the device and represents the substrate. On this latter, markers must be already reported (with previous fabrication steps) and they must correspond with both the origin and the x -axis, contained in the digital model, used to print the pattern.

The substrate is placed and fixed on the printing area. Through the superior camera, the origin marker on the substrate is individuated and their coordinates must be recorded, checking that the device is correctly oriented with respect to the x -axis (Fig. A13).

The recorded coordinates represent the current position of the nozzle, therefore the coordinates of the point, observed by the superior camera, must be determined through the following correspondence, as shown in Fig. A14:

$$\Delta x = 70.970$$

$$\Delta y = -32.949$$

For example, the *Current Position* of the nozzle is (73.861; -102.360), see Fig. A15. In order to obtain the real coordinates, observed by the camera, the following simple subtraction must be computed:

$$OFFSET_x = Current\ Position_x - \Delta x$$

$$OFFSET_y = Current\ Position_y - \Delta y$$

For this example:

$$OFFSET_x = 73.861 - 70.970 = 2.891$$

$$OFFSET_y = -102.360 + 32.949 = 52.440$$

This origin must be set as *Offset*, before launching the printing process. Now the pattern is ready to be printed, clicking on Start (Fig. A16).

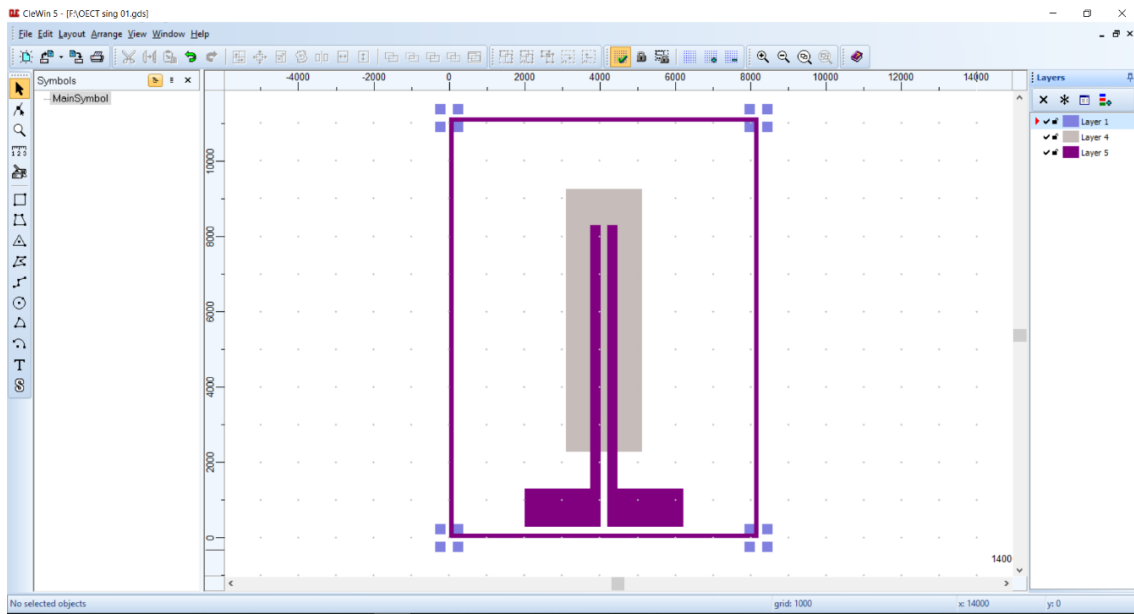


Fig. A12 – The model containing the whole layout of the device (the substrate and the pattern to be printed).

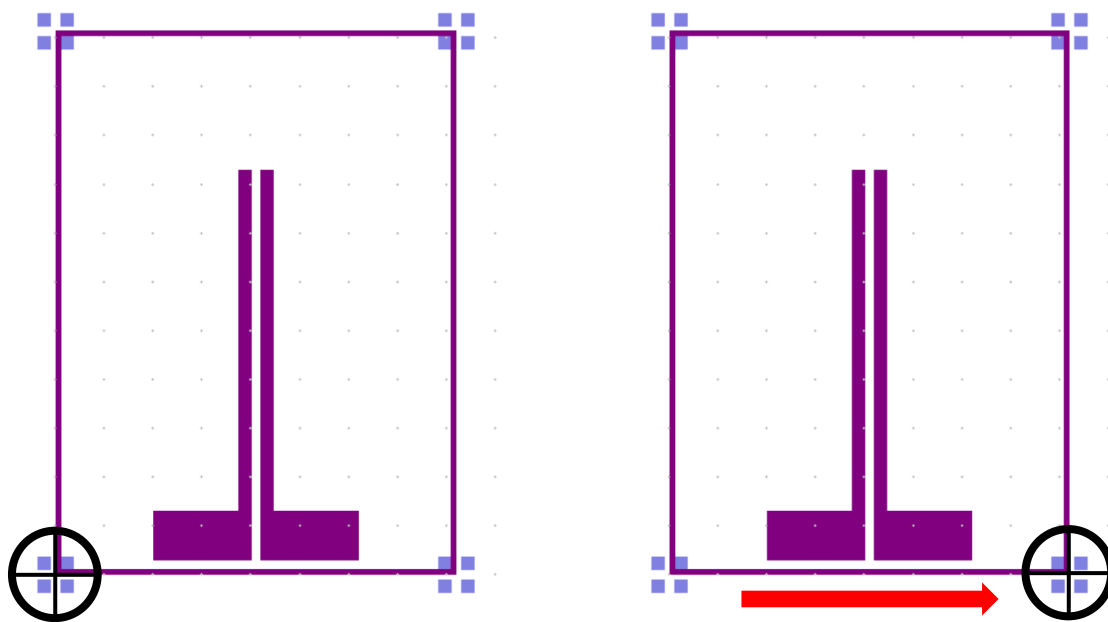


Fig. A13 – The checking of the horizontal orientation of the substrate. The black circle with the cross represents the point, observed by the superior camera.

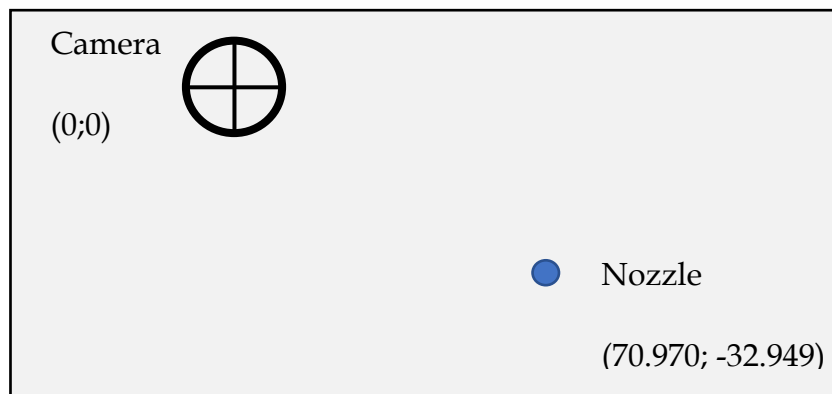


Fig. A14 – Scheme of the different positions of the camera view and the nozzle.

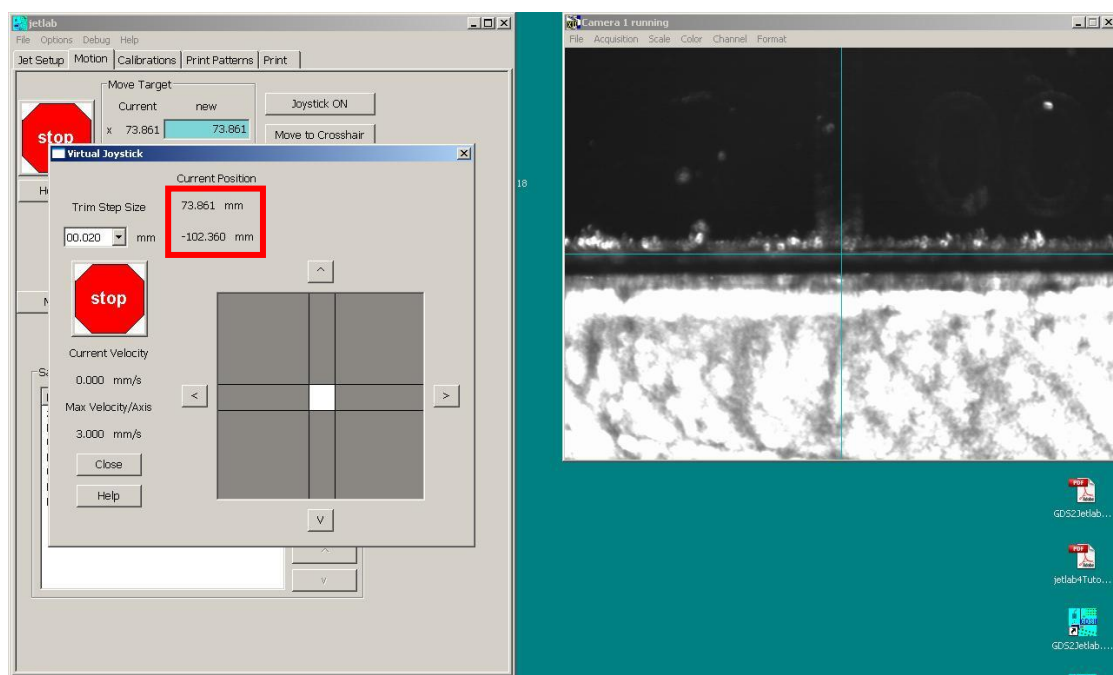


Fig. A15 – An example of the visualization of the origin point on the substrate through the superior camera and the corresponding of the Current Position of the nozzle.

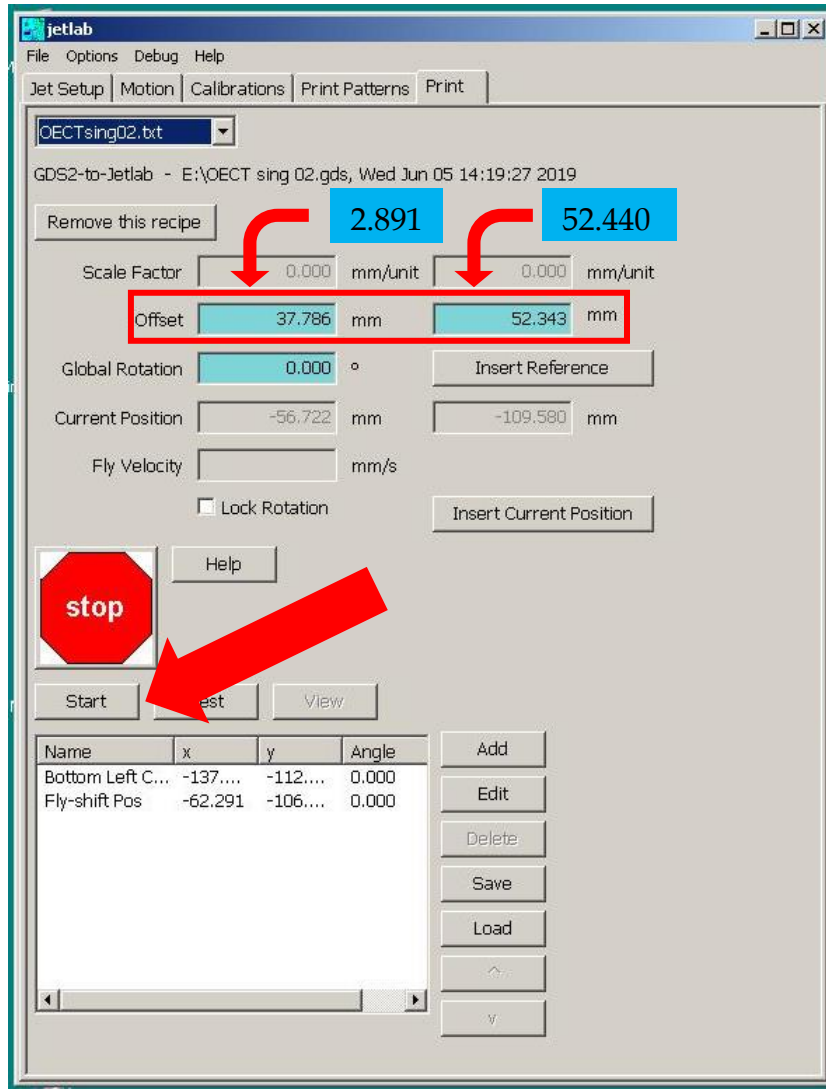


Fig. A16 – The new Offset must be set (in the example: 2.891 and 52.440), then the print is launching, clicking on Start.

References

1. Bai, L.; Elósegui, C.G.; Li, W.; Yu, P.; Fei, J.; Mao, L. Biological applications of organic electrochemical transistors: Electrochemical biosensors and electrophysiology recording. *Front. Chem.* **2019**, *7*, 1–16.
2. Strakosas, X.; Bongo, M.; Owens, R.M. The organic electrochemical transistor for biological applications. *J. Appl. Polym. Sci.* **2015**, *132*, 1–14.
3. Liao, J.; Si, H.; Zhang, X.; Lin, S. Functional sensing interfaces of PEDOT:PSS organic electrochemical transistors for chemical and biological sensors: A mini review. *Sensors (Switzerland)* **2019**, *19*.
4. Lu, B.; Yuk, H.; Lin, S.; Jian, N.; Qu, K.; Xu, J.; Zhao, X. Pure PEDOT:PSS hydrogels. *Nat. Commun.* **2019**, *10*.
5. Xu, Y.; Patsis, P.A.; Hauser, S.; Voigt, D.; Rothe, R.; Günther, M.; Cui, M.; Yang, X.; Wieduwild, R.; Eckert, K.; et al. Cytocompatible, Injectable, and Electroconductive Soft Adhesives with Hybrid Covalent/Noncovalent Dynamic Network. *Adv. Sci.* **2019**, *1802077*.
6. Guex, A.G.; Puetzer, J.L.; Armgarth, A.; Littmann, E.; Stavriniidou, E.; Giannelis, E.P.; Malliaras, G.G.; Stevens, M.M. Highly porous scaffolds of PEDOT:PSS for bone tissue engineering. *Acta Biomater.* **2017**, *62*, 91–101.

7. Del Agua, I.; Marina, S.; Pitsalidis, C.; Mantione, D.; Ferro, M.; Iandolo, D.; Sanchez-Sanchez, A.; Malliaras, G.G.; Owens, R.M.; Mecerreyes, D. Conducting Polymer Scaffolds Based on Poly(3,4-ethylenedioxythiophene) and Xanthan Gum for Live-Cell Monitoring. *ACS Omega* **2018**, *3*, 7424–7431.
8. Qureshi, A.; Gurbuz, Y.; Niazi, J.H. Biosensors for cardiac biomarkers detection: A review. *Sensors Actuators, B Chem.* **2012**, *171–172*, 62–76.
9. Piro, B.; Mattana, G.; Zrig, S.; Anquetin, G.; Battaglini, N.; Capitaio, D.; Maurin, A.; Reisberg, S. Fabrication and use of organic electrochemical transistors for sensing of metabolites in aqueous media. *Appl. Sci.* **2018**, *8*.
10. Tarabella, G.; Villani, M.; Calestani, D.; Mosca, R.; Iannotta, S.; Zappettini, A.; Coppedè, N. A single cotton fiber organic electrochemical transistor for liquid electrolyte saline sensing. *J. Mater. Chem.* **2012**, *22*, 23830–23834.
11. Coppedè, N.; Tarabella, G.; Villani, M. Human Stress Monitoring Through an Organic Cotton-Fiber Biosensor. *J. Mater. Chem. B* **2014**, *2*, 5620–5626.
12. Gualandi, I.; Marzocchi, M.; Achilli, A.; Cavedale, D.; Bonfiglio, A.; Fraboni, B. Textile Organic Electrochemical Transistors as a Platform for Wearable Biosensors. *Sci. Rep.* **2016**, *6*, 1–10.
13. Liao, C.; Mak, C.; Zhang, M.; Chan, H.L.W.; Yan, F. Flexible organic electrochemical transistors for highly selective enzyme biosensors and used for saliva testing. *Adv. Mater.* **2015**, *27*, 676–681.
14. Thackeray, J.W.; White, H.S.; Wrighton, M.S. Poly(3-methylthiophene)-coated electrodes: Optical and electrical properties as a function of redox potential and amplification of electrical and chemical signals using poly(3-methylthiophene)-based microelectrochemical transistors. *J. Phys. Chem.* **1985**, *89*, 5133–5140.
15. Nikolou, M.; Malliaras, G.G. Applications of poly (3,4-ethylenedioxythiophene) doped with poly(styrene sulfonic acid) transistors in chemical and biological sensors. *Chem. Rec.* **2008**, *8*, 13–22.
16. Khodagholy, D.; Rivnay, J.; Sessolo, M.; Gurfinkel, M.; Leleux, P.; Jimison, L.H.; Stavriniidou, E.; Herve, T.; Sanaur, S.; Owens, R.M.; et al. High transconductance organic electrochemical transistors. *Nat. Commun.* **2013**, *4*, 1–6.
17. Shi, H.; Liu, C.; Jiang, Q.; Xu, J. Effective Approaches to Improve the Electrical

- Conductivity of PEDOT:PSS: A Review. *Adv. Electron. Mater.* **2015**, *1*, 1–16.
18. Nilsson, D.; Chen, M.; Kugler, T.; Remonen, T.; Armgarth, M.; Berggren, M. Bi-stable and dynamic current modulation in electrochemical organic transistors. *Adv. Mater.* **2002**, *14*, 51–54.
 19. Bernardis, D.A.; Malliaras, G.G. Steady-state and transient behavior of organic electrochemical transistors. *Adv. Funct. Mater.* **2007**, *17*, 3538–3544.
 20. Bard, A.J.; Faulkner, L.R.; Bagotsky, V.S. *Electrochemical Methods Fundamentals of Electrochemistry*; 2001; ISBN 9780471700586.
 21. Bernardis, D.A.; MacAya, D.J.; Nikolou, M.; Defranco, J.A.; Takamatsu, S.; Malliaras, G.G. Enzymatic sensing with organic electrochemical transistors. *J. Mater. Chem.* **2008**, *18*, 116–120.
 22. Lin, P.; Yan, F.; Chan, H.L.W. Ion-sensitive properties of organic electrochemical transistors. *ACS Appl. Mater. Interfaces* **2010**, *2*, 1637–1641.
 23. He, R.X.; Zhang, M.; Tan, F.; Leung, P.H.M.; Zhao, X.Z.; Chan, H.L.W.; Yang, M.; Yan, F. Detection of bacteria with organic electrochemical transistors. *J. Mater. Chem.* **2012**, *22*, 22072–22076.
 24. Gentili, D.; D'Angelo, P.; Militano, F.; Mazzei, R.; Poerio, T.; Brucale, M.; Tarabella, G.; Bonetti, S.; Marasso, S.L.; Cocuzza, M.; et al. Integration of organic electrochemical transistors and immuno-affinity membranes for label-free detection of interleukin-6 in the physiological concentration range through antibody-antigen recognition. *J. Mater. Chem. B* **2018**, *6*, 5400–5406.
 25. Sessolo, M.; Rivnay, J.; Bandiello, E.; Malliaras, G.G.; Bolink, H.J. Ion-selective organic electrochemical transistors. *Adv. Mater.* **2014**, *26*, 4803–4807.
 26. Bernardis, D.A.; Malliaras, G.G.; Toombes, G.E.S.; Gruner, S.M. Gating of an organic transistor through a bilayer lipid membrane with ion channels. *Appl. Phys. Lett.* **2006**, *89*, 1–3.
 27. Xiong, C.; Wang, Y.; Qu, H.; Zhang, L.; Qiu, L.; Chen, W.; Yan, F.; Zheng, L. Highly sensitive detection of gallic acid based on organic electrochemical transistors with poly(diallyldimethylammonium chloride) and carbon nanomaterials nanocomposites functionalized gate electrodes. *Sensors Actuators, B Chem.* **2017**, *246*, 235–242.

28. Tang, H.; Yan, F.; Lin, P.; Xu, J.; Chan, H.L.W. Highly sensitive glucose biosensors based on organic electrochemical transistors using platinum gate electrodes modified with enzyme and nanomaterials. *Adv. Funct. Mater.* **2011**, *21*, 2264–2272.
29. Shim, N.Y.; Bernardis, D.A.; Macaya, D.J.; DeFranco, J.A.; Nikolou, M.; Owens, R.M.; Malliaras, G.G. All-plastic electrochemical transistor for glucose sensing using a ferrocene mediator. *Sensors* **2009**, *9*, 9896–9902.
30. Liu, J.; Agarwal, M.; Varahramyan, K. Glucose sensor based on organic thin film transistor using glucose oxidase and conducting polymer. *Sensors Actuators, B Chem.* **2008**, *135*, 195–199.
31. Wen, Y.; Xu, J. Scientific Importance of Water-Processable PEDOT-PSS and Preparation, Challenge and New Application in Sensors of Its Film Electrode: A Review. *J. Polym. Sci. Part A Polym. Chem.* **2017**, *55*, 1121–1150.
32. Khan, S.; Lorenzelli, L.; Dahiya, R.S. Technologies for printing sensors and electronics over large flexible substrates: A review. *IEEE Sens. J.* **2015**, *15*, 3164–3185.
33. Sigma Aldrich website <https://www.sigmaaldrich.com/technical-documents/articles/materials-science/organic-electronics/agfa-opv.html>.
34. Rivnay, J.; Leleux, P.; Ferro, M.; Sessolo, M.; Williamson, A.; Koutsouras, D.A.; Khodagholy, D.; Ramuz, M.; Strakosas, X.; Owens, R.M.; et al. High-performance transistors for bioelectronics through tuning of channel thickness. *Sci. Adv.* **2015**, *1*, 1–6.
35. Hai, W.; Goda, T.; Takeuchi, H.; Yamaoka, S.; Horiguchi, Y.; Matsumoto, A.; Miyahara, Y. Human influenza virus detection using sialyllactose-functionalized organic electrochemical transistors. *Sensors Actuators, B Chem.* **2018**, *260*, 635–641.
36. Kim, D.J.; Lee, N.E.; Park, J.S.; Park, I.J.; Kim, J.G.; Cho, H.J. Organic electrochemical transistor based immunosensor for prostate specific antigen (PSA) detection using gold nanoparticles for signal amplification. *Biosens. Bioelectron.* **2010**, *25*, 2477–2482.
37. Zhang, L.; Wang, G.; Xiong, C.; Zheng, L.; He, J.; Ding, Y.; Lu, H.; Zhang, G.; Cho, K.; Qiu, L. Chirality detection of amino acid enantiomers by organic electrochemical transistor. *Biosens. Bioelectron.* **2018**, *105*, 121–128.

38. Ji, X.; Lau, H.Y.; Ren, X.; Peng, B.; Zhai, P.; Feng, S.P.; Chan, P.K.L. Highly Sensitive Metabolite Biosensor Based on Organic Electrochemical Transistor Integrated with Microfluidic Channel and Poly(N-vinyl-2-pyrrolidone)-Capped Platinum Nanoparticles. *Adv. Mater. Technol.* **2016**, *1*, 1–8.
39. Mak, Chun; Liao, Caizhi; Fu, Ying; Zhang, M. Highly-sensitive epinephrine sensors based on organic electrochemical transistors with carbon nanomaterial modified gate electrodes. *J. Mater. Chem. C* **2015**, *3*, 6532–6538.
40. Liao, C.; Zhang, M.; Niu, L.; Zheng, Z.; Yan, F. Organic electrochemical transistors with graphene-modified gate electrodes for highly sensitive and selective dopamine sensors. *J. Mater. Chem. B* **2014**, *2*, 191–200.
41. Pappa, A.M.; Curto, V.F.; Braendlein, M.; Strakosas, X.; Donahue, M.J.; Fiocchi, M.; Malliaras, G.G.; Owens, R.M. Organic Transistor Arrays Integrated with Finger-Powered Microfluidics for Multianalyte Saliva Testing. *Adv. Healthc. Mater.* **2016**, *5*, 2295–2302.
42. Contat-Rodrigo, L.; Pérez-Fuster, C.; Lidón-Roger, J.V.; Bonfiglio, A.; García-Breijo, E. Screen-printed Organic Electrochemical Transistors for the detection of ascorbic acid in food. *Org. Electron. physics, Mater. Appl.* **2017**, *45*, 89–96.
43. Braendlein, M.; Pappa, A.M.; Ferro, M.; Lopresti, A.; Acquaviva, C.; Mamesier, E.; Malliaras, G.G.; Owens, R.M. Lactate Detection in Tumor Cell Cultures Using Organic Transistor Circuits. *Adv. Mater.* **2017**, *29*.
44. Yang, S.Y.; Cicoira, F.; Byrne, R.; Benito-Lopez, F.; Diamond, D.; Owens, R.M.; Malliaras, G.G. Electrochemical transistors with ionic liquids for enzymatic sensing. *Chem. Commun.* **2010**, *46*, 7972–7974.
45. Song, J.; Lin, P.; Ruan, Y.F.; Zhao, W.W.; Wei, W.; Hu, J.; Ke, S.; Zeng, X.; Xu, J.J.; Chen, H.Y.; et al. Organic Photo-Electrochemical Transistor-Based Biosensor: A Proof-of-Concept Study toward Highly Sensitive DNA Detection. *Adv. Healthc. Mater.* **2018**, *7*, 1–8.
46. Guo, X.; Liu, J.; Liu, F.; She, F.; Zheng, Q.; Tang, H.; Ma, M.; Yao, S. Label-free and sensitive sialic acid biosensor based on organic electrochemical transistors. *Sensors Actuators, B Chem.* **2017**, *240*, 1075–1082.
47. Liao, J.; Lin, S.; Yang, Y.; Liu, K.; Du, W. Highly selective and sensitive glucose

- sensors based on organic electrochemical transistors using TiO₂ nanotube arrays-based gate electrodes. *Sensors Actuators, B Chem.* **2015**, *208*, 457–463.
48. Liao, J.; Lin, S.; Zeng, M.; Yang, Y. A miniature photoelectrochemical sensor based on organic electrochemical transistor for sensitive determination of chemical oxygen demand in wastewaters. *Water Res.* **2016**, *94*, 296–304.
49. Gualandi, I.; Tonelli, D.; Mariani, F.; Scavetta, E.; Marzocchi, M.; Fraboni, B. Selective detection of dopamine with an all PEDOT:PSS Organic Electrochemical Transistor. *Sci. Rep.* **2016**, *6*, 1–10.
50. Ji, Xudong; Chan, P.K.L. Highly Sensitive Glucose Sensor Based on Organic Electrochemical Transistor with Modified Gate Electrode. *Methods Mol. Biol.* **2017**, *1572*, 205–216.
51. Pecqueur, S.; Lenfant, S.; Guérin, D.; Alibart, F.; Vuillaume, D. Concentric-electrode organic electrochemical transistors: Case study for selective hydrazine sensing. *J. Phys. Conf. Ser.* **2017**, *939*.
52. Wet-chemical etching for metals (from Microchemicals) www.microchemicals.com/downloads/application_notes.html.
53. Clevios PH1000 Datasheet from Heraeus https://www.heraeus.com/media/media/hec/documents_hec/data_sheets_hep/81076212_PD_Clevios_PH_1000.pdf.
54. Microfab Technotes, 99-02 <http://www.microfab.com/images/pdfs/technote99-02.pdf>.
55. Microfab Technotes, 99-01 <http://www.microfab.com/images/pdfs/technote99-01.pdf>.
56. Inkjet printing process for kesterite solar cells <https://phys.org/news/2015-05-inkjet-kesterite-solar-cells.html>.
57. Streptavidin-Peroxidase Datasheet from Sigma Aldrich https://www.sigmaaldrich.com/content/dam/sigmaaldrich/docs/Sigma/Product_Information_Sheet/1/s5512pis.pdf.
58. Chiadò, A.; Palmara, G.; Frascella, F. Optimization and characterization of a homogeneous carboxylic surface functionalization for silicon-based biosensing.

- Colloids Surf B Biointerfaces* **2016**, *143*, 252–259.
59. Bart, J.; Tiggelaar, R.; Yang, M.; Schlautmann, S.; Zuilhof, H.; Gardeniers, H. Room-temperature intermediate layer bonding for microfluidic devices. *Lab Chip* **2009**, *9*, 3481–3488.
60. Gan, H.Y.; Shan, X.; Eriksson, T.; Lok, B.K.; Lam, Y.C. Reduction of droplet volume by controlling actuating waveforms in inkjet printing for micro-pattern formation. *J. Micromechanics Microengineering* **2009**, *19*.
61. Microfab Technotes, 99-03
<http://www.microfab.com/images/pdfs/technote99-03.pdf>.
62. Bogy, D.B.; Talke, F.E. Experimental and Theoretical Study of Wave Propagation Phenomena in Drop-on-Demand Ink Jet Devices. *IBM J. Res. Dev.* **1984**, *28*, 314–321.
63. Microfab Technotes Creation of small microdrops
http://www.microfab.com/images/pdfs/smalldrops_Nov06_v3.pdf.
64. Dankoco, M.D.; Tesfay, G.Y.; Benevent, E.; Bendahan, M. Temperature sensor realized by inkjet printing process on flexible substrate. *Mater. Sci. Eng. B Solid-State Mater. Adv. Technol.* **2016**, *205*, 1–5.
65. Kim, N.; Kee, S.; Lee, S.H.; Lee, B.H.; Kahng, Y.H.; Jo, Y.R.; Kim, B.J.; Lee, K. Highly conductive PEDOT:PSS nanofibrils induced by solution-processed crystallization. *Adv. Mater.* **2014**, *26*, 2268–2272.
66. Heeger A. J. Semiconducting and Metallic Polymers : the Fourth Generation of Polymeric. *Synthetic Met.* **2001**, *125*, 23–42.
67. Kim, S.M.; Kim, C.H.; Kim, Y.; Kim, N.; Lee, W.J.; Lee, E.H.; Kim, D.; Park, S.; Lee, K.; Rivnay, J.; et al. Influence of PEDOT:PSS crystallinity and composition on electrochemical transistor performance and long-term stability. *Nat. Commun.* **2018**, *9*.
68. Håkansson, A.; Han, S.; Wang, S.; Lu, J.; Braun, S.; Fahlman, M.; Berggren, M.; Crispin, X.; Fabiano, S. Effect of (3-glycidyoxypropyl)trimethoxysilane (GOPS) on the electrical properties of PEDOT:PSS films. *J. Polym. Sci. Part B Polym. Phys.* **2017**, *55*, 814–820.

69. Stavriniidou, E.; Leleux, P.; Rajaona, H.; Khodagholy, D.; Rivnay, J.; Lindau, M.; Sanaur, S.; Malliaras, G.G. Direct measurement of ion mobility in a conducting polymer. *Adv. Mater.* **2013**, *25*, 4488–4493.